# CFD Simulation Analyses of the Blowdown Phase of a Depressurized Loss of Forced Cooling Accident in a HTGR

**Keenan Kresl-Hotz and Mohamed S. El-Genk**

Institute for Space and Nuclear Power Studies and Nuclear Engineering Department, The University of New Mexico, Albuquerque, NM, USA

**Report No. UNM-ISNPS-02-2026**
Institute for Space and Nuclear Power Studies, The University of New Mexico,
Albuquerque, NM, USA, http://isnps.unm.edu/reports/

**May 2026**

# Abstract

This research numerically investigates the helium-air mixing in HTGR containment cavities during the blowdown phase of a simulated DLOFC accident. The results of the performed CFD simulation analyses, using the commercial code STAR-CCM+, are compared with reported measurements from an experiment conducted at CCNY. The analyses investigate the effects of the RANS and LES turbulence models, numerical mesh refinement, time-step size, and flow rate and temperature of the injected hot helium into the scaled reactor cavity. Calculated parameters analyzed include the pressure and spatial distributions of temperature and oxygen concentration in the simulated reactor and steam generator cavities. CFD oxygen concentration predictions agree well with experimental measurements early in the transient but diverge later. Temperature comparisons show good agreement during the middle of the transient, with overprediction early and underprediction late. The LES model resolves significantly more small-scale eddies, producing more uniform helium-air mixing than the RANS model.

# Table of Contents


Abstract ........ iii

Table of Contents ........ iiv

List of Figures ........ vi

List of Tables ........ x

Nomenclature ........ xi

Chapter 1 – Background ........ 1

1.1 High Temperature Gas-cooled Reactors (HTGRs) ........ 1

1.1.1: Prismatic Core HTGR Layout and GA-MHTGR Design ........ 2

1.1.2: Reactor Cavity Cooling Systems (RCCSs) ........ 6

1.2 Depressurized Loss of Forced Cooling (DLOFC) Accident ........ 8

Chapter 2 – Introduction ........ 11

2.1 Literature Review ........ 11

2.2 Research Objectives ........ 21

Chapter 3 – Methodology and Approach: Cavity 1 ........ 23

3.1 Approach ........ 24

3.1.1 Assumptions and boundary conditions ........ 25

3.1.2 Numerical Mesh Grid and Turbulent Parameter Estimates ........ 25

3.2 Adaptive Time Step Scheme ........ 29

3.3 Numerical Grid Turbulence Resolution ........ 30

Chapter 4 – Results and Discussion: Cavity 1 ........ 32

4.1 Cavity 1 Pressure ........ 34

4.2 Flow Velocity and Mixing Eddies ........ 36

4.3 Oxygen Concentration ........ 39

4.4 Temperature ........ 47

4.5 Summary ........ 50

Chapter 5 – Analyses of Cavity 1 Connected to Cavity 2 ........ 52
5.1 Methodology and Approach ........ 53
5.1.1 Numerical Mesh Grid ........ 54
5.1.2 Isolation Valve ........ 55
5.1.3 Adaptive Time Step ........ 56
5.2. Results and Discussion ........ 57
5.2.1 Effect of the Valve Opening Time ........ 58
5.2.2 Time Step Sensitivity ........ 60
5.2.3 Pressure Calculations and Comparison ........ 60
5.2.4 Flow Field Images ........ 61
5.2.5 Cavity Species Composition and Flow Rates ........ 64
5.2.6 Spatial Distributions of Oxygen Concentration ........ 68
5.2.7 Temperature Calculations and Comparison ........ 72
5.3 Summary ........ 81
Chapter 6 – Summary and Conclusions ........ 82
Appendix A – Feed Tube CFD Simulation Analyses ........ 86
A1 Analysis Methodology ........ 88
A2 Results and Discussion ........ 92
Appendix B – Measurements Uncertainties of Oxygen Concentration in the Experiments ........ 96
References ........ 99

# List of Figures

**Fig. 1.1:** GA-MHTGR module and steam generator (modified from IAEA 2014). .......... 3

**Fig. 1.2:** Cross-sectional view of the GA-MHTGR prismatic core layout (modified from IAEA [2014]). ........................................................................................ 4

**Fig. 1.3:** Prismatic HTGR Fuel Assembly (modified from Reitsma [2019] and Harp et al. [2014])........................................................................................................ 5

**Fig. 1.4:** GA-MHTGR Reactor Cavity Cooling System (RCCS) (IAEA 2014). ............... 6

**Fig. 1.5:** Section view of GA-MHTGR containment structure showing reactor and steam generator cavities (IAEA 2014). ............................................................... 8

**Fig. 2.1:** Experimental 1/28-scale He-air mixing facility (modified from Yang et al. [2018])...................................................................................................... 14

**Fig. 2.2:** Scaled HTGR Experiment of Balderrama Prieto and Arcilesi [2025] based on the GT-MHR design (modified from Balderrama Prieto and Arcilesi [2025]). ......... 16

**Fig. 2.3:** 1/28 scale He-air gas mixing experimental facility based on AREVA HTGR design of Revankar and Kultgen [2022] (modified from Kultgen [2025]).......... 17

**Fig. 2.4:** CCNY RCTF He-air gas mixing facility showing arrangement of cavities and locations of thermocouples (TC) and oxygen sensors (o) (modified from Abubakar et al. [2024]). ......................................................................................... 19

**Fig. 3.1:** Section views with the temperature and oxygen sensors mounted on the inside of the walls of Cavity 1 in RCTF test facility. ........................................................ 24

**Fig. 3.2:** Section view C-C of the implemented numerical mesh grid in present CFD simulation analyses of cavity 1 in the RCTF. ..................................................... 28

**Fig. 3.3**: Section view of numerical mesh within the fine refinement cylinder region. ... 30

**Fig. 4.1**: Reported experimental cavity temperature and He injection conditions used in performed CFD simulations of Experiment No. 6 of Abubakar, et al. [2024]: (a) initial air temperature in cavity, (b) experiment He injection flow rate, (c) experiment He injection temperature.................................................................. 34

**Fig. 4.2**: Calculated transient cavity pressure for CFD Cases A-D and reported experimental measurements [Abubakar et al., 2024]........................................... 35

**Fig. 4.3**: Cavity pressure parity plot. ..................................................................... 36

**Fig. 4.4**: Case D images of velocity fields in Cavity 1 calculated in the present CFD simulation analyses with LES turbulence model at select times; (0 to 50 m/s) full-

scale color contours........................................................................................ 37
**Fig. 4.5**: Case D images of velocity fields in Cavity 1 calculated in present CFD simulation analyses with LES turbulence model at selected times; 0 to 5 m/s scale color contours.......................................................................................................... 38
**Fig. 4.6**: Case D LES and RANS cavity velocity field comparison at 10 and 20 s during the simulated CFD transient analyses using 0 to 5 m/s Scale............................. 39
**Fig. 4.7**: Q-Criterion isosurfaces for Q = 100 with oxygen concentration contours superimposed at 22 s into the simulated transient, for case D with the LES turbulence model........................................................................................... 40
**Fig. 4.8**: Q-Criterion isosurfaces for Q = 100 with oxygen concentration contours superimposed at a time of 22 s for case D with the RANS turbulence model...... 41
**Fig. 4.9**: Reported oxygen sensor measurements in Experiment No. 6 of Abubakar, et al. [2024]............................................................................................................ 42
**Fig. 4.10**: Calculated progression of the oxygen concentration field in cavity 1 for Case D, CFD analyses with the LES turbulence model at select times during the simulation transient.......................................................................................................... 43
**Fig. 4.11**: Case D LES and RANS cavity oxygen concentration field comparison at 10 and 20 s during the simulated transient using 0 to 20.95 mol % scale color contours. 44
**Fig. 4.12**: Comparison of calculated and the reported oxygen concentrations in cavity 1 by Abubakar et al. [2024]. .......................................................................... 45
**Fig. 4.13**: Comparison of calculated local oxygen concentration for OS3 and OS4 and the reported experimental measurements of Abubakar et al. [2024]......................... 46
**Fig. 4.14**: Calculated images of the progressive development of the temperature field in cavity 1 at select times during the CFD simulated analysis transient.................. 47
**Fig. 4.15**: Images of the calculated temperature fields in cavity 1 in the CFD analyses with RANS turbulence model at 10 and 20 s during the simulated transient. .............. 47
**Fig. 4.16**: Comparisons of calculated temperatures in the present CFD analyses with reported thermocouple measurements by Abubakar et al. [2024]. ....................... 49
**Fig. 5.1:** Cavities 1 and 2 Setup and Instrumentation..................................................... 53
**Fig. 5.2:** Transient Injection Flow Rate and Temperature............................................... 54
**Fig. 5.3:** Employed Numerical Mesh Grid refinements in Cavities 1 and 2. ................... 55
**Fig. 5.4:** Numerical Mesh Grid in the solenoid valve and the pipe connecting Cavities 1

and 2 in the present CFD simulation analyses. .................................................... 56
**Fig. 5.5:** Comparison of calculated pressure with reported measurements in the simulated transient after connecting cavity 1 to cavity 2. .................................................... 58
**Fig. 5.6:** The effect of the duration of the valve connecting cavities 1 and 2 of the flow field in cavity 1, 200 ms after opening the valve. ............................................... 59
**Fig. 5.7:** Calculated flow fields in cavity 1, 3.0 s after being connected to cavity 2........ 60
**Fig. 5.8:** Comparison of the calculated pressure in cavity 1 for the present CFD analyses with the LES turbulence model with reported experimental measurements [Abubakar et al. 2024]. ......................................................................................... 61
**Fig. 5.9:** Time progression of the calculated flow fields in cavities 1 and 2 at selected times during the simulated transient, with 0 to 50 m/s scale of the color contours........ 62
**Fig. 5.10:** Time progression of the calculated flow fields in cavities 1 and 2 at selected times during the simulated transient, with 0 to 5 m/s scale of the color contours. 63
**Fig. 5.11.** The calculated moles of He and air in cavities 1 and 2 during the simulated transient. ........................................................................................................ 64
**Fig. 5.12:** Comparisons of the calculated flow rate of He and air in cavities 1 and 2 during the simulated transient, in the CFD analyses with the LES turbulence model. .... 66
**Fig. 5.13:** Calculated spatial distributions of oxygen concentrations in cavities 1 and 2 at select times during the simulated transient. ........................................................ 68
**Fig. 5.14:** Comparison of the calculated oxygen concentration in cavity 1 to the reported measurements during the simulated transient. ..................................................... 70
**Fig. 5.15:** Comparison of local oxygen concentration in cavity 2 with reported measurements. ............................................................................................... 71
**Fig. 5.16:** Comparisons of the calculated temperature fields in Cavity 1 at select times during the simulated transient, using 296 to 773 K scale color contours. ............ 74
**Fig. 5.17:** Comparison of calculated temperatures in cavity 1 during the simulated transient with the reported measurements in the experiment [Abubakar et al. 2024]. ........ 76
**Fig. 5.18:** Comparison of the calculated local temperatures in cavity 2 with reported measurements in the experiment by Abubakar et al. [2024]. .............................. 78
**Fig. 5.19:** Comparison of the calculated temperature in cavity 1 with the reported DTS temperature measurements [Abubakar et al. 2024]. ............................................ 80
**Fig. A1:** He Feed Tube Configuration without a Flow Development Entrance Section.. 87

**Fig. A2:** He feed tube configuration with a flow development entrance section. ........... 88
**Fig. A3:** Radial cross sections of the implemented numerical mesh grids in the Inconel and stainless-steel sections of the feed tube. ............................................................. 90
**Fig. A4:** Radial He Velocity and Temperature at Exit of the feed tube with and without Development Length. ........................................................................................ 91
**Fig. A5:** Centerline He Velocity and Temperature along the length of the feed tube, with and without Development Length. ....................................................................... 92
**Fig. A6:** Radial distribution of the He flow velocity and temperature at the exit of the feed tube without a flow development section and with and without TC in the stainless-steel section. ............................................................................................... 93
**Fig. A7:** Calculated radial He velocity and temperature profiles at multiple axial locations in the feed tube, with and without TC in the stainless-steel section. .................... 94
**Fig. A8:** Temperature contours in stainless-steel section with (a) and without (b) TC.... 95
**Fig. A9:** Velocity contours in the stainless-steel section with (a) and without (b) TC. ... 95

# List of Tables


**Table 1.1:** Total current and projected nuclear electricity production [IAEA 2025]......... 1

**Table 2.1:** Summary of scaled experiments investigating the He-air mixing in HTGR containment cavities during the blowdown phase of a simulated DLOFC accident. ........................................................................................................................ 11

**Table 3.1:** Cavity solid wall mesh parameters. .............................................................. 26

**Table 3.2:** LIKE Results for hot He injection into Cavity 1. .......................................... 26

**Table 3.3:** Cavity fluid region mesh parameters. ............................................................ 28

**Table 3.4:** Turbulent kinetic energy parameters of various regions in the reactor cavity.31

**Table 4.1:** Input to CFD analyses...................................................................................... 32

**Table 5.1:** Cavity region cell counts. ................................................................................ 55

**Table 5.2:** Effect of CFL choice on the timestep size in the simulated transient............. 57

**Table A1:** Inconel and stainless-steel material properties. ............................................. 88

**Table A2:** Numerical mesh grid refinement parameters. ................................................ 89

**Table A3:** Temperature difference of injection and TC locations at various heater powers. ........................................................................................................................ 95

## Nomenclature

*Acronyms and Abbreviations*

| | |
|---|---|
| CCNY | City College of New York |
| CFD | Computational Fluid Dynamics |
| CO | Carbon Monoxide |
| DLOFC | Depressurized Loss Of Forced Cooling |
| DNS | Direct Numerical Simulation |
| DOE | United States Department of Energy |
| DTS | Distributed Temperature Sensor |
| GA-MHTGR | General Atomics Modular High Temperature Gas-cooled Reactor |
| GT-MHR | Gas Turbine-Modular High temperature gas-cooled Reactor |
| He | Helium |
| HTGR | High Temperature Gas-cooled Reactor |
| HTTR | High Temperature Test Reactor |
| IAEA | International Atomic Energy Agency |
| IEA | International Energy Agency |
| ISNPS | Institute for Space and Nuclear Power Studies |
| LES | Large Eddy Simulation |
| LWR | Light Water Reactor |
| NGNP | Next Generation Nuclear Plant |
| OS | Oxygen Sensor |
| PCS | Passive Containment heat removal System |
| RANS | Reynolds Averaged Navier Stokes |
| RCCS | Reactor Cavity Cooling System |
| RCTF | Reactor Cavity Test Facility |
| Rx | Reactor |
| SCS | Shutdown Cooling System |
| SG | Steam Generator |
| SST | Shear Stress Transport |
| TC | Thermocouple |
| TRISO | Tri-Structural ISOtropic |

| | |
|---|---|
| UNM | University of New Mexico |
| VHTR | Very High Temperature gas-cooled Reactor |
| WALE | Wall Adapting Local Eddy viscosity |

*Dimensionless Numbers:*

| | |
|---|---|
| CFL | Courant-Friedrichs-Lewy number |
| Re | Reynolds Number |

*Variables:*

| | |
|---|---|
| k | Turbulent Kinetic Energy |
| $k_{res}$ | Resolved Turbulent Kinetic Energy |
| $k_{sgs}$ | Subgrid-Scale Turbulent Kinetic Energy |
| R | Turbulent Kinetic Energy Ratio |
| z | Axial Position (in Feed tube) |

# Chapter 1 – Background

Nuclear energy is playing a key role in meeting growing global electricity demand. It is expected to support the growing electricity needs, primarily driven by data centers and Artificial Intelligence applications worldwide [Crownhart 2025, DOE 2025, IAEA 2025]. Large-scale data centers require a continuous, high-reliability electricity supply. In addition, the growing adoption of artificial intelligence would substantially increase the number of data centers to be built in the coming decades. In the United States, electricity demand for data centers alone is expected to increase by 325-580 TWh by 2028 [Shehabi et al. 2024]. Additionally, industrial electricity demand is expected to rise due to the onshoring of manufacturing and large-scale hydrogen production [Shehabi et al. 2024, IAEA 2025, IEA 2025]. Total electricity demand in North America alone is projected to increase at an average annual rate of 3% in the coming decades [IAEA 2025]. Adoption of electric vehicles and industrial and building electrification will increase future electricity demand [IEA 2025]. Nuclear Power is a baseload power option that operates 24/7, with no greenhouse gas emissions. The current worldwide capacity for electricity generation from nuclear power is expected to double by 2050 [IAEA 2025].

**Table 1.1:** Total current and projected nuclear electricity production [IAEA 2025].

| Electricity Production, (TWh) | 2024 | 2030 | | 2040 | | 2050 | |
|---|---|---|---|---|---|---|---|
| | | Low | High | Low | High | Low | High |
| North America | 863 | 853 | 863 | 893 | 1262 | 809 | 1945 |
| World | 2670.3 | 3095 | 3241 | 4051 | 5469 | 4534 | 7867 |

To keep up with rising electricity demand, many types of nuclear reactors are being considered. One of these types is the High Temperature Gas-cooled Reactor, of which over 14 designs are currently under development [IAEA 2024]. These advanced Gen-IV reactors will not only help meet base-load electricity demand but also provide high-temperature process heat for industrial applications. Thus, they are particularly suited for the diverse energy needs of the future energy landscape.

## *1.1 High Temperature Gas-cooled Reactors (HTGRs)*

High Temperature Gas-cooled Reactors (HTGRs) are being developed and deployed in many countries. They offer enhanced safety features and higher operating temperatures than Light Water Reactor (LWR) plants [Fütterer 2015, DOE 2024, Kindra et al. 2025]. There are currently two categories of this reactor type, distinguished by the reactor outlet temperature:

HTGRs with an exit temperature of 1,000 K and VHTRs (Very High Temperature gas-cooled Reactors) with a higher exit temperature of 1,300 K. The VHTRs enable more efficient electricity generation, exceeding 48%, and high-temperature process heat for industrial applications such as hydrogen production [Generation IV International Forum 2014]. The HTGRs, the focus of the present work, are helium (He) cooled and graphite-moderated reactors that have been developed and operated in Europe, the United States, China, Russia, and Japan over the past six decades [Beck and Pincock 2011]. These reactors also enable high energy conversion efficiency in excess of 48% using a superheated steam Rankine cycle, a direct He gas Brayton cycle, or a combined cycle [El-Genk and Tournier 2009]. There are two HTGR core configurations, namely: the pebble bed and prismatic core reactors.

### *1.1.1: Prismatic Core HTGR Layout and GA-MHTGR Design*

Examples of prismatic core HTGRs include the 30 $MW_{th}$ High Temperature Test Reactor (HTTR) built in Japan, the 600 $MW_{th}$ General Atomics Modular HTGR (GA-MHTGR) (Fig. 1.1), and the 22 $MW_{th}$ HOLOS Quad MMR concepts under development [Shiozawa et al. 2004, IAEA 2014, Stauff and Lee 2021]. Fig. 1.1 presents a section view of the GA-MHTGR design, showing the reactor pressure vessel coupled to the steam generator module [IAEA 2014]. This HTGR has a prismatic core, operates at 4-7 MPa, and is He-cooled.

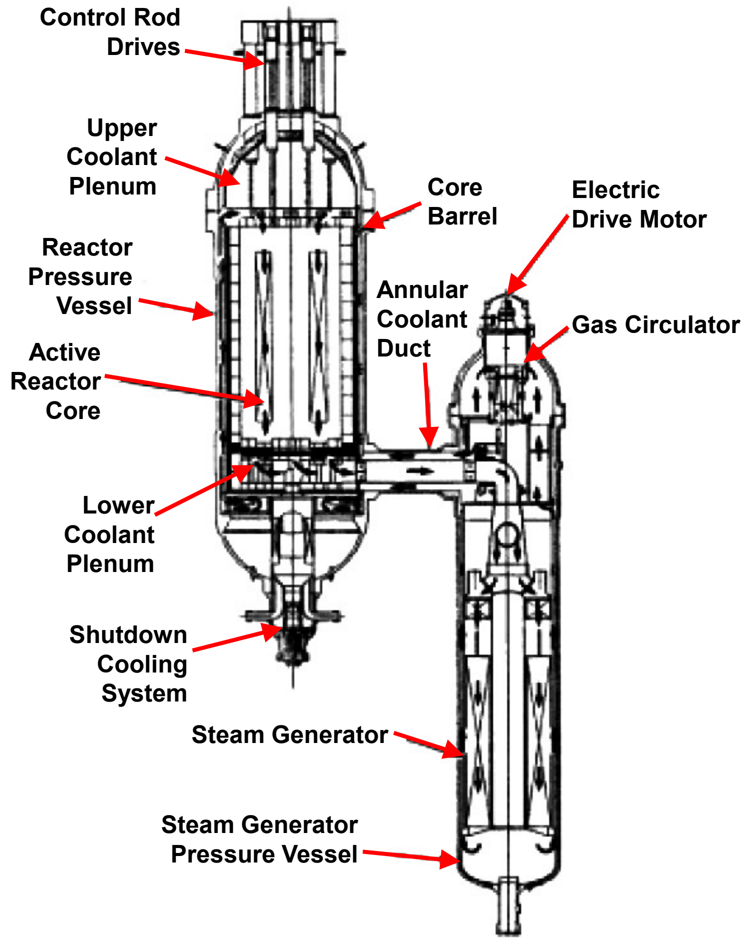


**Fig. 1.1:** GA-MHTGR module and steam generator (modified from IAEA 2014).

The cooler He returning from the steam generator helps cool the pressure vessel as it flows upward [Shiozawa et al. 2004; IAEA 2014] through the space between the core barrel and the pressure vessel. The He then enters the upper plenum and flows downward through coolant channels in the active core to remove the heat produced by nuclear fission. The heated He that exits through the bottom of the annular reactor core to the lower plenum space flows out through the inner portion of the concentric coolant duct connecting the reactor and the energy conversion vessels. The hot He enters the steam generator, producing superheated steam for electricity generation via a Rankine cycle.

The He coolant is circulated through the prismatic core using a gas circulator driven by an electric drive motor. Following a reactor shutdown, decay heat from the core is removed nominally by the independent Shutdown Cooling System (SCS) (Fig. 1.1) [IAEA 2014]. The SCS located at the bottom of the reactor vessel includes a water-cooled compact heat exchanger to remove decay heat and a motor-driven gas circulator to maintain the flow of in-vessel He through the core. The annular prismatic core HTGR, like the GA-MHTGR, comprises three rings of hexagonal fuel element blocks with graphite reflector blocks in the inner and outer neutron reflector regions of the core (Fig. 1.2) [Beck and Pincock 2011].

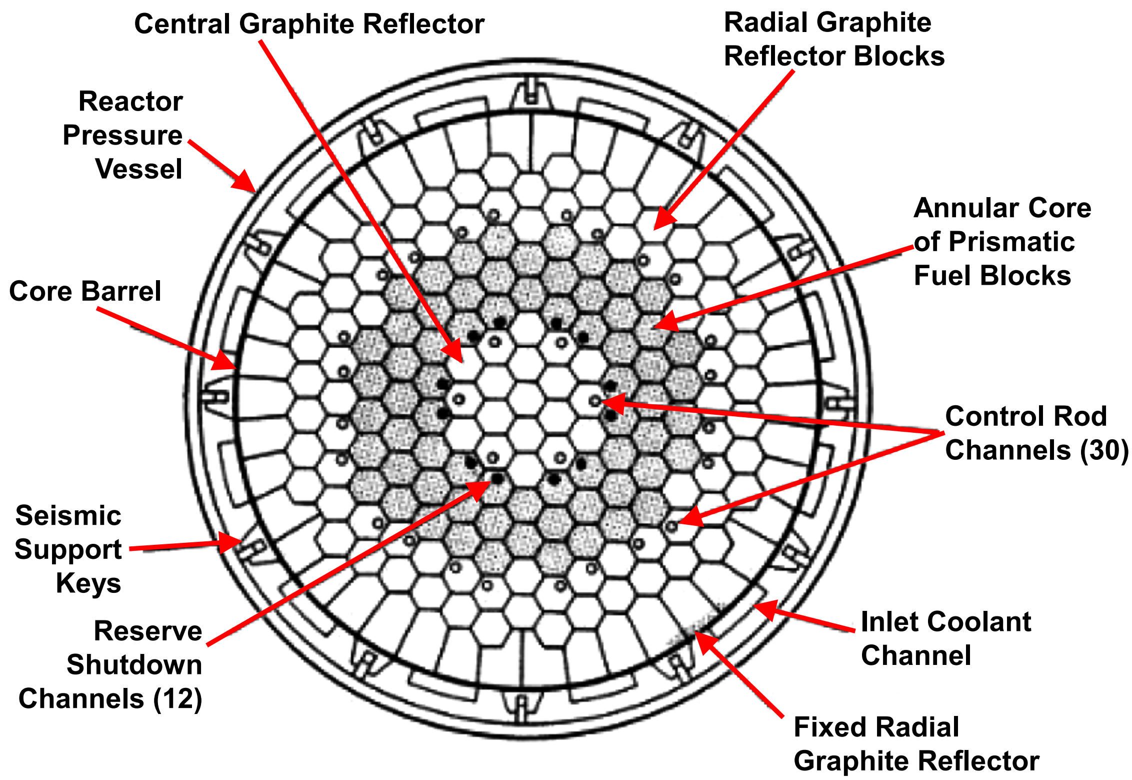


**Fig. 1.2:** Cross-sectional view of the GA-MHTGR prismatic core layout (modified from IAEA [2014]).

Select reflector blocks include channels for $B_4C$ rods for reactor control during startup, shutdown, and nominal operation (Fig. 1.2). Twelve fuel element blocks in the first ring of the annular core include reserve shutdown channels for dropping neutron-absorbing spheres into the core, providing an independent means for shutting down the reactor in an emergency. The cores of Prismatic HTGRs employ stacks (Fig. 1.3a) of hexagonal-prism-shaped graphite fuel blocks (Fig. 1.3b) with some holes for loading stacks of fuel compacts, which are sometimes referred to as fuel rods (Fig. 1.3c). The fuel compacts contain TRISO (Tri-Structural Isotropic) fuel particles. Fuel compacts are TRISO fuel particles dispersed in nuclear graphite. The TRISO particle consists of ~0.6 mm diameter fuel kernels of UCO or $UO_2$ encapsulated in multiple layers of porous carbon buffer, pyrolytic carbon, and silicon carbide (Fig. 1.3e) [Zhou and Tang 2011]. The chemical-vapor-deposited layers provide a barrier to the diffusion of fission products and have been demonstrated to maintain mechanical integrity at temperatures exceeding 1600 °C [Wells et al. 2021]. Holes in the fuel block that are not reserved for fuel are coolant channels for He gas to pass through and remove the fission heat generated within the block (Fig. 1.3a). A small fraction of the total He flow, referred to as bypass flow, passes through the gaps between the hexagonal fuel and reflector blocks [Qin and Song 2022]. Rather than stacking fuel compacts in graphite blocks, pebble bed reactors employ randomly packed spherical fuel elements that can be continuously circulated through the reactor core. This continuous feed of fuel pebbles is a distinct operational difference from that of prismatic-core HTGRs.

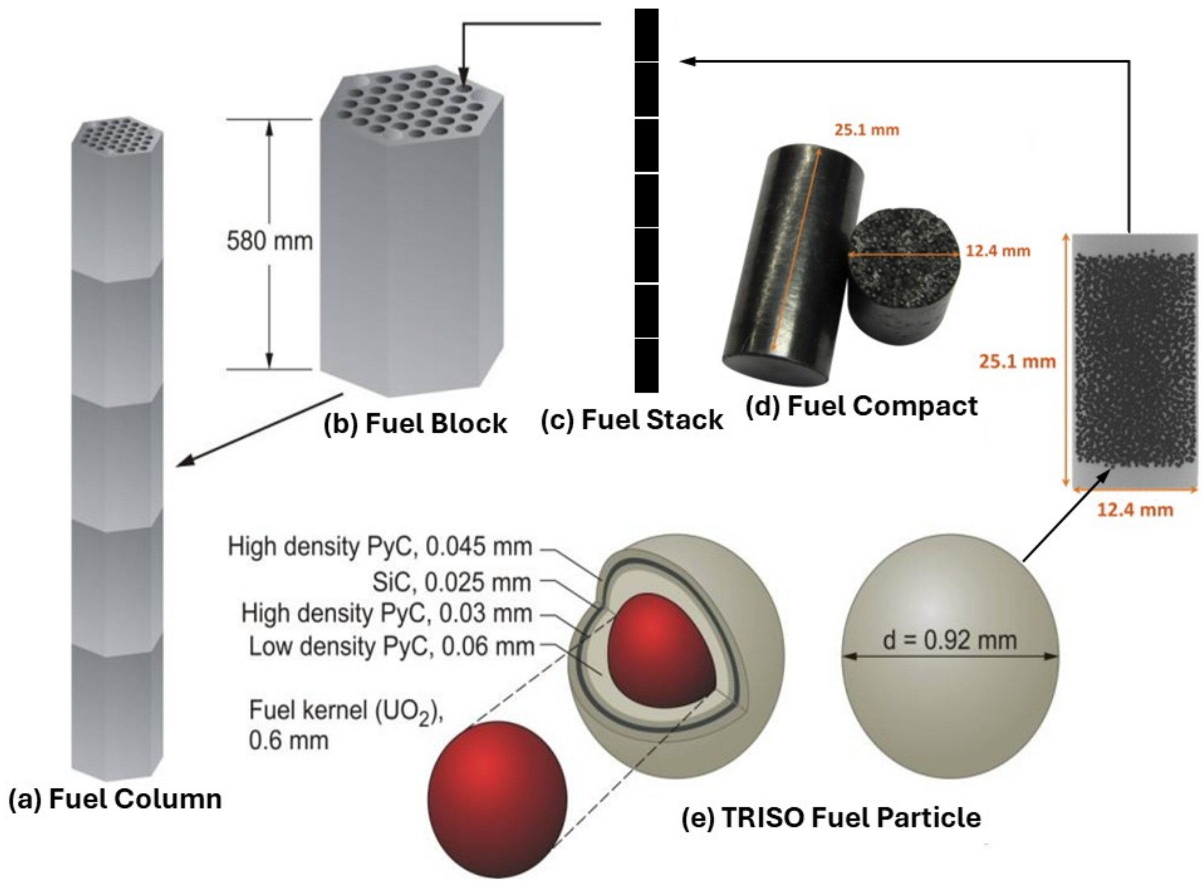


**Fig. 1.3:** Prismatic HTGR Fuel Assembly (modified from Reitsma [2019] and Harp et al. [2014]).

*1.1.2: Reactor Cavity Cooling Systems (RCCSs)*

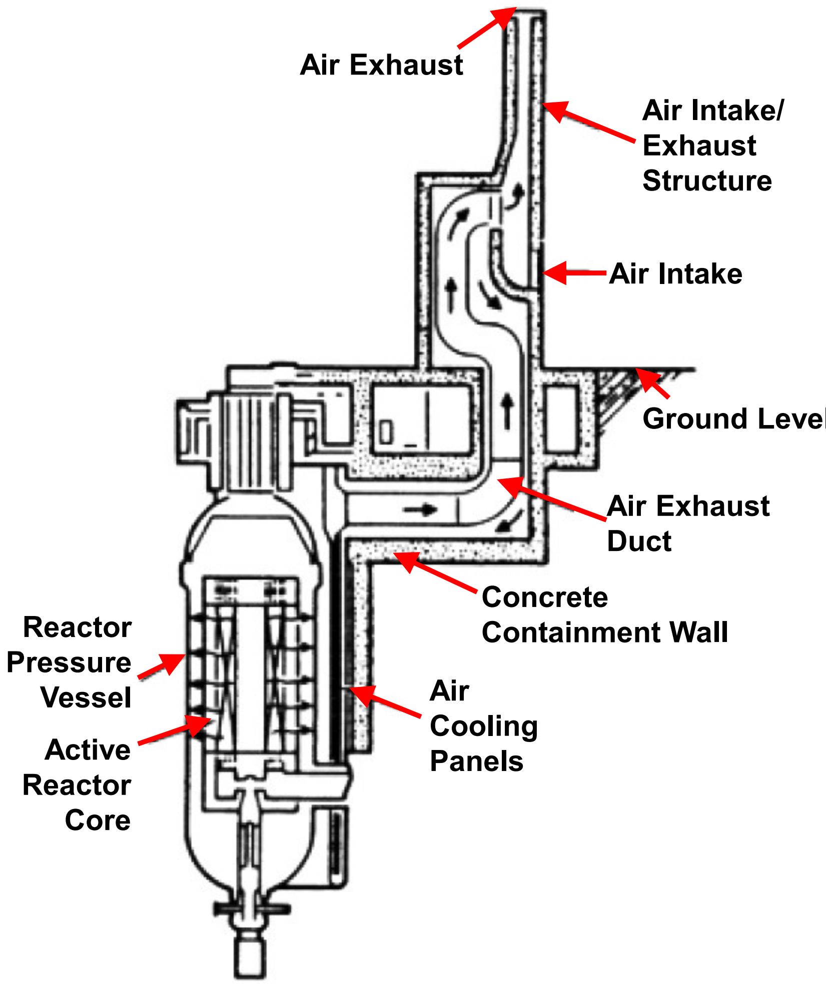


**Fig. 1.4:** GA-MHTGR Reactor Cavity Cooling System (RCCS) (IAEA 2014).

The Reactor Cavity Cooling System (RCCS) is a common design feature of HTGRs [Lisowski et al. 2021]. It is a passive safety feature that removes heat dissipated from the exterior surface of the nuclear reactor's pressure vessel during normal operation and accident scenarios. The system typically consists of cooling panels or water-filled tubes arranged around the reactor cavity that remove heat from the reactor vessel's exterior surface by both radiation and convection. Its primary purpose is to protect the concrete biological shield and containment structures from excessive rise in temperature while providing a passive heat sink that requires no active components or operator intervention [Lisowski et al. 2021]. This passive cooling safety system prevents structural damage during loss-of-coolant accidents or other emergency conditions.

The RCCS is also an auxiliary means for decay heat removal in the GA-MHTGR design (Fig. 1.4). Decay heat generated within the reactor core transfers radially to the pressure vessel wall by conduction and thermal radiation [IAEA 2014]. Enclosed cooling panels affixed to the walls of the reactor cavity then remove the dissipating heat, from the outer surface of the un-insulated reactor vessel, by natural circulation of ambient air (Fig. 1.4). The air within the RCCS ducts is isolated from the air inside the reactor containment cavity to minimize the release of radioactive Argon-41 and other gaseous fission products to the atmosphere in the event of a break in the primary coolant loop [IAEA 2014]. A break in the primary coolant loop and subsequent coolant discharge into the reactor cavity can further affect the RCCS's convective cooling capabilities [Lisowski et al. 2021]. Accidents resulting in the discharge of the pressurized He coolant and the ingress of an ambient air-He mixture into the reactor core are unlikely but of great safety concern in HTGRs [Oh and Kim 2010].

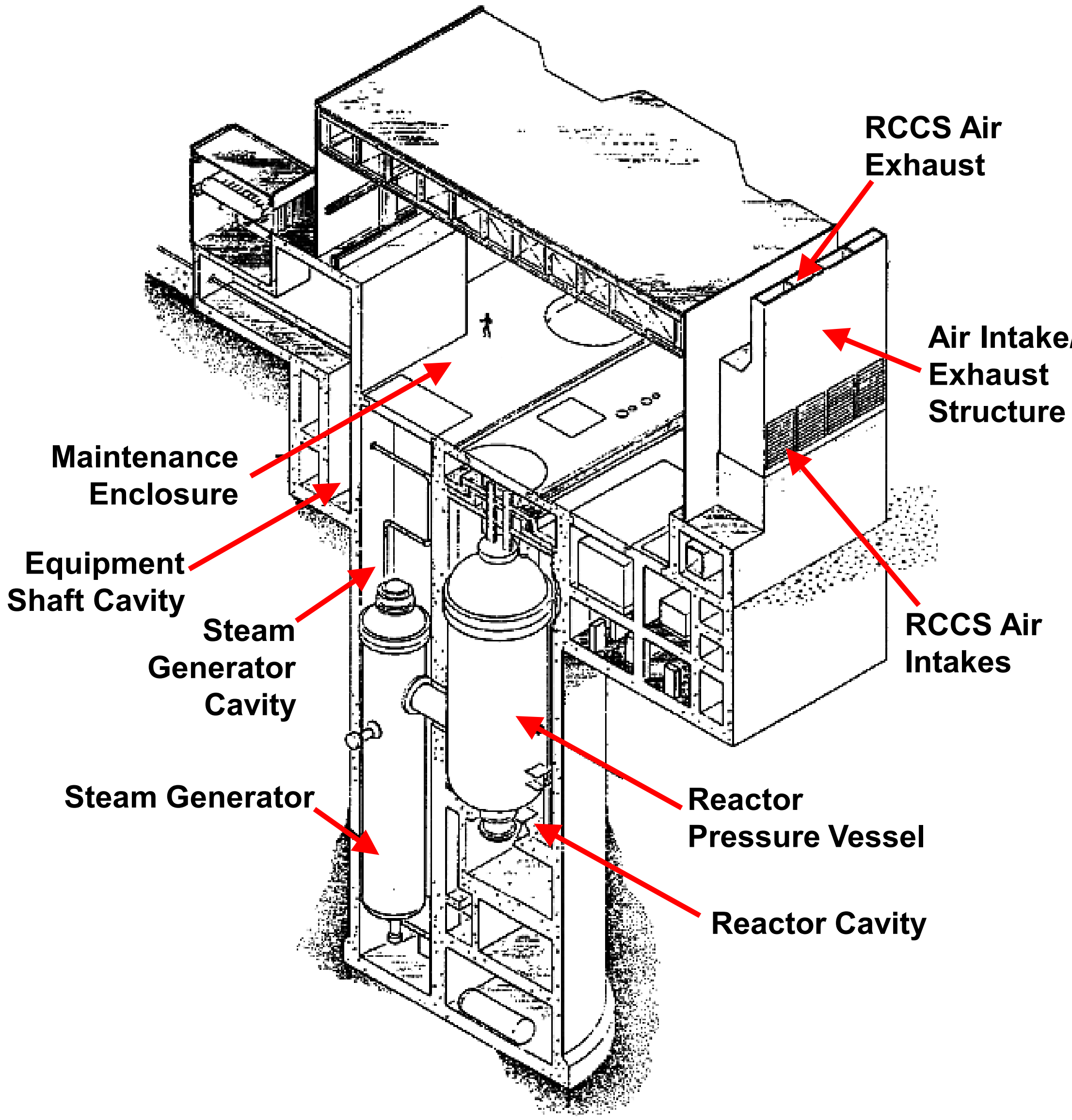


**Fig. 1.5:** Section view of GA-MHTGR containment structure showing reactor and steam generator cavities (IAEA 2014).

### *1.2 Depressurized Loss of Forced Cooling (DLOFC) Accident*

A Depressurized Loss of Forced Cooling (DLOFC) is identified as one of the postulated design-basis accidents for HTGRs, such as the GA-MHTGR [Huning et al. 2021]. Fig. 1.5 presents a section view of the containment for the GA-MHTGR, with rectangular cavities connected to the reactor and steam generator pressure vessels. Following an unlikely break in the primary coolant system, the circulating hot He gas in the primary loop discharges into the reactor and steam generator cavities. Such an accident proceeds in three successive phases [Oh and Kim 2010], namely: (a) the blowdown phase, (b) the refill phase, and (c) the ingress phase.

During the **blowdown phase**, the pressurized He that exits into the containment cavities through a pipe or pressure vessel break(s). It displaces and mixes with the air in the surrounding cavity. As He continues to discharge from the primary system, the pressures in the connected reactor and steam generator cavities approach equilibrium. This marks the transition to the second phase of the accident, the **refill phase**. During this phase, the air within the connected cavities is withdrawn back into the primary loop system where the initial break(s) occurred.

When the decreasing primary loop pressure comes to equilibrium with the pressure within the containment cavities, it marks the issuance of the **ingress phase** of the accident. The cavities will likely be filled with either a well-mixed air-He mixture, with stratified layers of He, or only He or air, depending on the cavity vent paths [Oh and Kim 2010]. At this stage, the He-air mixture may enter the reactor primary loop through the break(s) in the primary cooling system and flow up through the core, causing gasification of the graphite structure and the fuel elements. Air ingress can create multiple safety concerns, including: (a) oxidation of the structural graphite components in the reactor, potentially decreasing their structural integrity, (b) remobilization of radionuclides and $^{14}C$ within the core graphite, and (c) potential generation of flammable gases such as carbon monoxide (CO) [El-Genk et al. 2014, Oh and Kim 2009]. The U.S. NRC classifies the air ingress following a DLFOC accident as highly important to the safety analyses of HTGRs [Ball and Fischer 2008a, 2008b].

Analysis of air ingress following a DLOFC has conservatively assumed that pure air enters the HTGR core, causing gasification of the graphite structure and fuel elements [Oh and Kim 2010, El-Genk and Tournier 2012 and 2013, El-Genk et al. 2014]. However, the He gas that escapes into the reactor cavity is likely to mix with the ambient air before the DLOFC accident's ingress phase begins. Thus, the gas entering the reactor would more realistically be a mixture of air and He with a range of molecular mixing ratios that depend on the accident scenario and transient progression. The composition of this mixture will depend on the break size, location, and orientation, as well as on the local pressures in both the reactor and the energy conversion module cavities. The design of the reactor containment and possible venting to other compartments or to the environment will also affect values of these pressures [Wilson et al. 2012]. Some HTGR containment designs provide a path for venting the reactor cavity during the blowdown phase [Li et al. 2020]. This allows the high-pressure He gas exiting the reactor vessel to partially displace the air within the reactor cavity and force it out through the vent.

During the ingress phase, the concentration of oxygen within the He-air mixture decreases with time. Thus, closing the vent would retain a He-rich mixture within the reactor cavity. The reactor cavity would then have less oxygen available to enter the reactor vessel, limiting the gasification and damage to the reactor.

During the air ingress phase of the accident, the partial pressure of the air entering the reactor core will be affected by the He-air mixing and possible stratification inside the reactor cavity [Oh and Kim 2010, Wilson et al. 2012]. Additionally, the mixing and stratification affect the heat transfer properties of the gas mixture and, consequently, the rate of heat removal by natural convection from the outer surface of the reactor vessel. Therefore, representative safety analysis of a postulated DLOFC and prediction of potential consequences require a good understanding of He-air mixing and stratification within the reactor and energy conversion cavities during the early phases of the accident.

The safety significance of He-air mixing and stratification during a DLOFC accident underscores the need for both experimental and computational investigations of these phenomena. While conservative safety analyses have traditionally assumed pure air ingress into the reactor core, the actual gas composition entering the reactor during the ingress phase depends strongly on the mixing dynamics during the preceding blowdown and refill phases. Understanding these dynamics requires a detailed characterization of the spatial and temporal distributions of the He-air mixture within the reactor and steam generator cavities. To this end, several scaled experimental facilities have been constructed, and simulation efforts have investigated He-air mixing in HTGR containment cavities, which are reviewed in the following section.

# Chapter 2 – Introduction

Many experimental and computational investigations of air ingress into HTGRs following depressurization during a DLOFC accident have been conducted [Oh et al. 2009, Andre et al. 2019, Oh and Kim 2011, Balderrama Prieto and Arcilesi et al. 2025, Ham et al. 2016]. However, there has been much less focus on the mixing of the He gas with air and stratification during the blowdown phase of the accident. Several small-scale experimental facilities have been constructed to investigate He-air mixing within the cavities surrounding the reactor vessel and the heat exchanger or energy conversion equipment.

## *2.1 Literature Review*

Table 2.1 summarizes the reported experiments by Yang et al. [2018], Balderrama Prieto and Arcilesi [2025], Kultgen [2025], and Abubakar et al. [2024, 2025] of He-air mixing within scaled-down HTGR containment cavities during the simulated blowdown phase of a DLOFC accident. These experiments investigated the effect of the location of He coolant gas injection into the reactor and the steam generator/power-conversion cavities. They compared the oxygen concentrations and the temperatures of the He-air mixture at various locations within cavities during simulated transients.

**Table 2.1:** Summary of scaled experiments investigating the He-air mixing in HTGR containment cavities during the blowdown phase of a simulated DLOFC accident.

| Reference | Focus/Methodology | Findings | Comments |
|---|---|---|---|
| Yang et al. [2018] | • Investigated the effects of He gas injection location and venting flow paths on the composition of the He-air mixture during the blowdown and the refill phases of DLOFC.<br>• Injected He through ports at the top of the reactor and the steam generator cavities.<br>• Experiments employed a gas leakage rate proportional to that expected for NGNP | • With an upper vent path open, the injected He at the top of the steam generator cavity exits without mixing with air in the lower cavities.<br>• With a lower vent flow path, good mixing of He and air occurred in the steam generator cavity. | • Experiments used unheated He gas.<br>• The vent path was sealed until the pressure differential between the reactor and steam generator cavities was > 6.89 kPa<br>• Did not report measurements of the oxygen concentration in the reactor cavity in experiments. |

| | | | |
|---|---|---|---|
| | design [Ball et al. 2008]. | | |
| Balderrama Prieto and Arcilesi [2025] | • Investigated effects of changing the sizes and locations of He venting along the reactor pressure vessel and the venting duration on the He-air mixing during the simulated blowdown and refill phases of a DLOFC transient.<br>• Vent on the PCS cavity closed after a period in experiments. | • Increasing the venting time increased the oxygen concentration in the He-air mixture at the end of the simulated transient.<br>• The break location negligibly affects oxygen concentration in the gas mixture within the reactor cavity. | • Injected He into the scaled GT-MHR containment through break ports along the sides of the reactor pressure vessel. This vessel contained heated, pressurized He before a simulated break. |
| Kultgen [2025] | • Investigated effects of the injection flow rate, temperature, and location into the Rx and SG cavities on the He-air mixing during the blowdown and refill phases of a simulated DLOFC accident.<br>• He gas injection was at fully developed conditions, constant temperature, and flow rate. | • Lower oxygen concentrations with He injection into the Rx cavity compared to those in the SG cavity.<br>• Axial location of break affected the oxygen concentration in the He-air mixture for He injection in the SG cavity, but not in the Rx cavity.<br>• Stratification in the He-air mixture increased with increased He injection. | • Path to vent is closed until internal pressure exceeds 108 kPa. |
| Abubakar et al. [2024, 2025] | • Investigated effects of He injection rate, temperature, and axial location along the wall of the Rx cavity in a simulated blowdown phase of a DLOFC.<br>• Used He injection nozzles with circular and rectangular | • The He injection through the lower port increased mixing more than the upper port injection.<br>• A circular nozzle caused greater stratification in the reactor cavity, while high velocity flow through a rectangular | • Investigated He gas injection temperature up to 500 °C<br>• Connected the reactor and steam generator cavities when the differential pressure exceeded 6.89 kPa.<br>• Cavities did not include dummy |

| | | | |
|---|---|---|---|
| | openings flush with cavity wall, and upward and downward facing horizontal slots in the He injection tube.<br>• Investigated effects of the shape and orientation of the injection orifice on gas mixing in the cavities. | nozzle induced greater mixing.<br>• Upward-oriented horizontal break increased stratification, compared to the downward-oriented break. | reactor or steam generator vessels. |

Yang et al. [2018] investigated He-air mixing in a 1/28-scale experiment of the Next Generation Nuclear Plant (NGNP) HTGR containment. The facility comprises separate cavities representing those surrounding the reactor pressure vessel, the steam generator vessel, and the equipment shaft in the NGNP design (Fig. 2.1). They investigated the air-He mixing during a DLOFC accident with different He leak locations and a connection pathway between the three cavities. The experiments measured temperatures, pressures, and oxygen concentrations in a He-air mixture across the three cavities.

They investigated the effects on He-air mixing and He gas stratification using different He injection nozzle configurations. The facility includes a magnetic louver connected to either the steam generator cavity or the equipment shaft cavity (Fig. 2.1), which opens to connect the reactor and SG cavities when the differential pressure reaches a setpoint of 6.89 kPa (1 psig). This allows pressure relief and venting of the gas mixture to the environment. The cavities include valves that provide gas-mixture leakage paths during the tests (Fig. 2.1). These valves are designed to match the gas leakage rate predicted for the NGNP containment design [Yang et al. 2018]. The measured leaking rates are calibrated during testing, and the proportional decrease in the reactor cavity pressure over time is reported to be consistent with the expected leak rate.

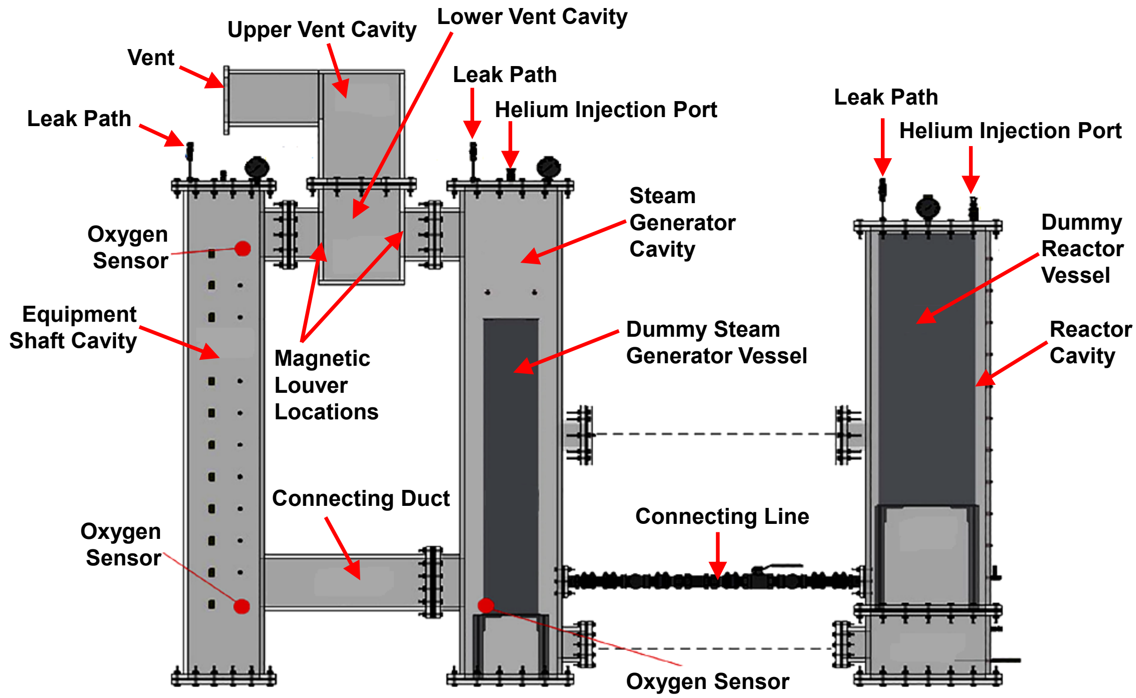


**Fig. 2.1:** Experimental 1/28-scale He-air mixing facility (modified from Yang et al. [2018]).

Experiments performed by Yang et al. [2018] focused on the refill phase of a DLOFC accident, and limited mixing data is reported during the initial blowdown phase. The results showed that oxygen concentrations are highest in the lower portions of the cavities, while the lighter He accumulates at the top.

Yildiz et al. [2018] used the GOTHIC thermal-hydraulic code, developed to model nuclear containments [Numerical Applications Inc. 2014], to simulate the experimental facility described by Yang et al. [2018]. Simulations of the depressurization phase poorly predicted the spatial distributions of the oxygen concentrations within the cavities. Still, they showed a qualitative agreement with the He-air stratification recorded in the experiments [Yildiz et al. 2018].

Balderrama Prieto and Arcilesi [2025] constructed a 1/20 scale experimental facility based on the containment design of the Gas Turbine Modular He Reactor (GT-MHR) to investigate DLOFC transients. The experimental facility consists of two separate cavities representing the reactor cavity and the cavity surrounding the Brayton energy conversion turbomachinery (Fig. 2.2). The reactor cavity encloses a pressure vessel representing the reactor pressure vessel, and the energy conversion cavity encloses a dummy vessel representing the power conversion module. The reactor vessel includes an inlet for He gas injection and electric heaters for heating the contained gas. Before the start of the experiments, the He gas in the reactor vessel is pressurized to 965 kPa and heated to ~403 K. The reactor vessel had multiple break outlets with mounting points for pneumatic valves on the sides, to simulate different break sizes and locations. The two cavities are instrumented with thermocouples (TCs), oxygen sensors (OSs), and sensors to measure the local temperatures, oxygen concentrations, and flow velocities during the simulated accident transients. The vent mounted near the bottom of the energy conversion cavity discharges the He-air mixture into the environment. The experiments investigated the effects of break size and location on He injection from the reactor vessel into the surrounding cavity on oxygen concentration within the cavities of both the reactor and the energy conversion module [Balderrama Prieto and Arcilesi 2025]. Additionally, the experiments investigated the effects of the vent's size and location, and the venting time, on the He-air mixing and the oxygen concentrations in the cavities (Fig. 2.2).

The results confirmed the strong effect of venting time on the depressurization and the He-air mixing in the cavities [Balderrama Prieto and Arcilesi 2025]. Increasing the venting time lowered the gas-mixture temperatures in the cavities during the simulated accident and at the end of the transient. Increasing the venting time beyond 22 seconds increased the oxygen concentration and the gas mixture temperature in the cavities at the end of the venting period. The oxygen sensors mounted higher up along the walls of the cavities recorded lower concentrations than those mounted closer to the bottom, indicating He gas stratification in the He-air mixtures within the cavities [Balderrama Prieto and Arcilesi 2025]. The results also showed that the time to depressurize the reactor vessel decreases as the break size increases. However, the break location had little effect on the measured oxygen concentration within the cavities (Fig. 2.2).

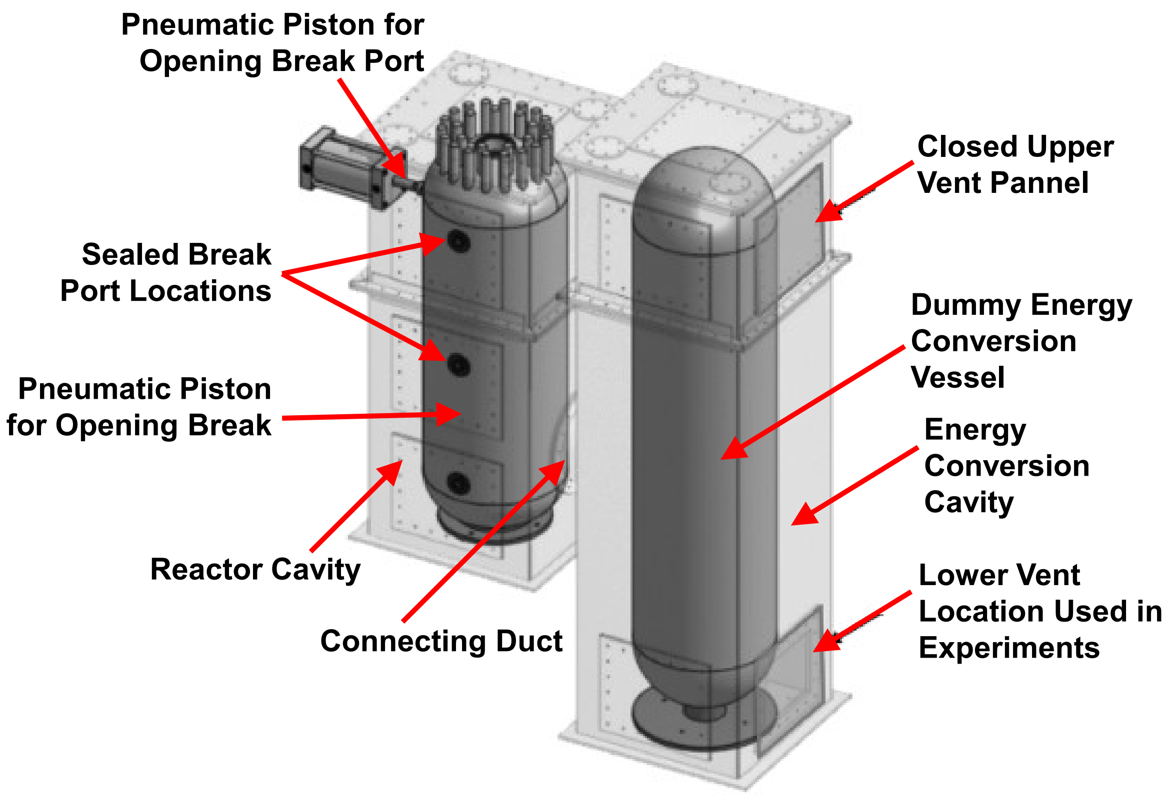


**Fig. 2.2:** Scaled HTGR Experiment of Balderrama Prieto and Arcilesi [2025] based on the GT-MHR design (modified from Balderrama Prieto and Arcilesi [2025]).

Sabharwall et al. [2022] have performed (Computational Fluid Dynamics) simulations of the experiments conducted in the facility shown in Fig. 2.2 using the STAR-CCM+ commercial code. The choices of the turbulence flow model and the numerical meshing refinements have not been reported. However, the results suggested that the observed increase in oxygen concentrations in the cavities during the experiments may be due to air backflow from the reactor cavity to the energy conversion cavity [Sabharwall et al. 2022]. The simulation results showed airflow along the lower portion of the connecting pipe into the reactor cavity, with the hotter He exiting through the upper portion.

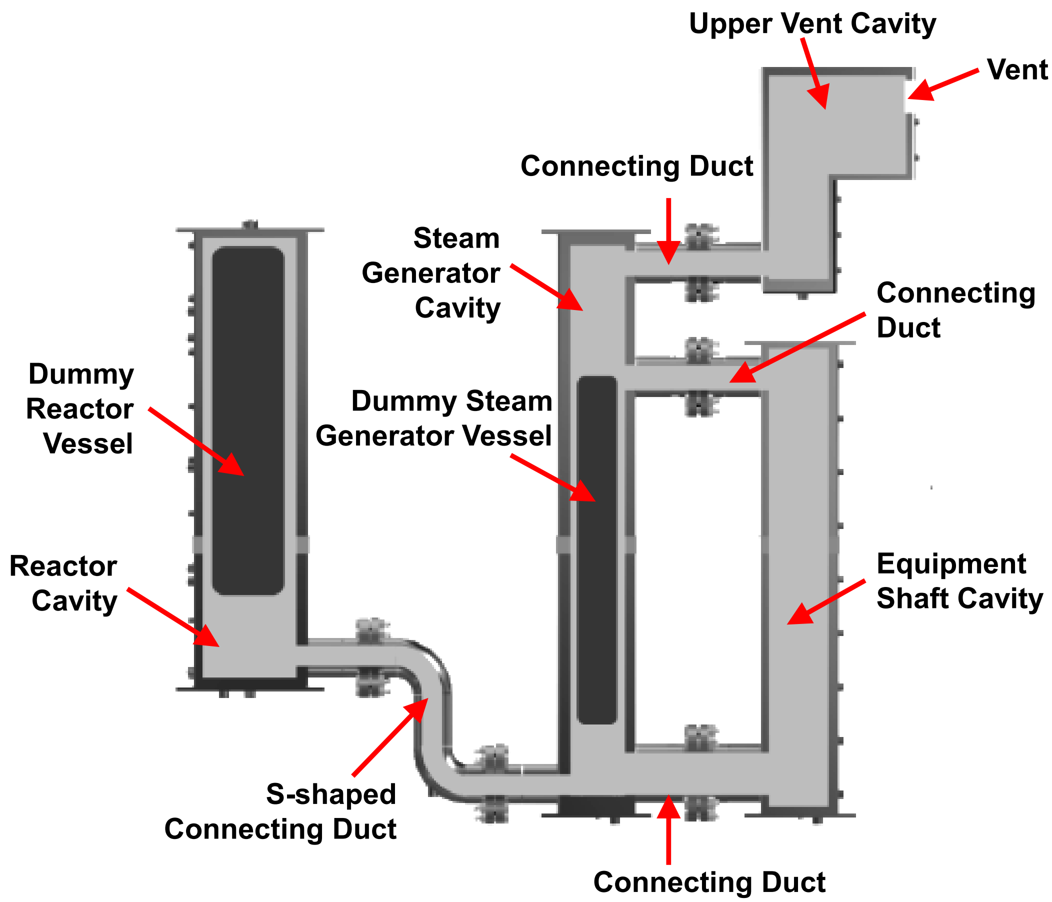


**Fig. 2.3:** 1/28 scale He-air gas mixing experimental facility based on AREVA HTGR design of Revankar and Kultgen [2022] (modified from Kultgen [2025]).

Kultgen [2025] constructed an experimental facility at Purdue University that represented a 1/28-scale model of the AREVA HTGR design to investigate a DLOFC transient [Revankar and Kultgen 2022]. The facility comprises a reactor cavity connected to the steam generator cavity and upper and lower vent cavities connected to the steam generator cavity (Fig. 2.3). The mock reactor and steam generator vessel in the respective cavities are for investigating the effects on the flow and mixing of the He-air mixture in the cavities [Kultgen 2025]. Heated He is injected into the cavities at different locations along the upper and lower sections of the reactor vessel and along the wall of the steam generator module. During the experiments, the electric heater wrapped around the He supply line heated the injected He gas to 673 K (400 °C) in the cavities. A manifold diverts the heated He flow, which reaches a constant temperature and velocity before being injected into the cavities. The cavities are instrumented with zirconia OSs to measure local gas composition, pressure transmitters to measure pressure, and K-type TCs to measure gas temperature.

The heated He gas at a constant temperature and flow rate is injected into the cavities for a fixed period determined by the volume of He gas in the source cylinder [Kultgen 2025]. The facility is initially sealed to prevent gas leakage with a valve programmed to open, when the measured pressure exceeds 108 kPa, venting the He-air mixture from the upper vent cavity (Fig. 2.3). The experiments investigated the effects of the He flow rate and the axial location of the break of the He injection along the wall of either the reactor vessel or the steam generator vessel into the respective cavities.

Results showed that the He gas injection into the steam generator vessel wall yields higher final oxygen concentrations in the reactor cavity than direct He injection into the reactor vessel cavity [Kultgen 2025]. In experiments with He injection along the reactor cavity wall, the oxygen concentrations at the end of the transients were <5 mol%. The axial location of the He gas injection within the steam generator cavity affected the oxygen distribution in the steam generator cavity at the end of the transient, but not in the reactor cavity. The He injection from the port near the bottom of the steam generator cavity increased the He accumulation at the top of the reactor cavity compared to the He gas injection through the port near the top of the cavity. The lower injection location increased the He flow in the S-shaped connecting pipe located near the bottom of the steam generator cavity [Kultgen 2025]. He injection near the top of the steam generator cavity produced uniform He-air mixing in the reactor and steam generator cavities. It also increased the He stratification in the top of the vent space cavities (Fig. 2.3) [Kultgen 2025]. He-air stratification was more pronounced in the experiments with larger break sizes.

Kultgen [2025] performed CFD simulation analyses of the Purdue HTGR Test Facility using the COMSOL commercial code [COMSOL Inc. 2020] with a simplified ½-scale of the experimental facility and a symmetry-plane boundary condition [Kultgen 2025]. The simulations used a coarse numerical mesh grid with the realizable k-ε turbulence model to minimize computational cost, and a multi-species transport model for the He-air flow. The simulations accounted for the heat losses through the stainless-steel walls of the test facility using a simplified 'thin shell' model. The simulation results were qualitatively in general agreement with the measured pressures but showed significant discrepancies with the measured oxygen concentrations [Kultgen 2025].

Recently, researchers at the City College of New York (CCNY) conducted experiments in the Reactor Cavity Test Facility (RCTF) to investigate the mixing of injected hot He with air in the reactor and other connected cavities during a simulated DLOFC event. They examined the effects of different break geometries, orientations, and locations on the mixing of the injected hot He with air in the cavities, as well as on the spatial distributions of temperature, oxygen concentration, pressure, and mixing velocities [Abubakar et al. 2024, 2025]. The Test Facility comprises a series of connected rectangular cavities representing those of the reactor, steam generator, the equipment shaft, and the upper and lower vent spaces (Fig. 2.4). The facility, modeled after the GA-MHTGR design, can be configured to represent different HTGR containment designs by opening and closing the connections between the cavities [Abubakar et al. 2024]. A valve isolates the reactor cavity from the steam generator cavity until the measured pressure difference between these cavities reaches 6.89 kPa. Beyond this point, the two cavities are connected. The experiments investigated the spatial and temporal distributions of the He-air mixture temperature and the oxygen concentration within these cavities during the blowdown and refill phases of simulated DLOFC events.

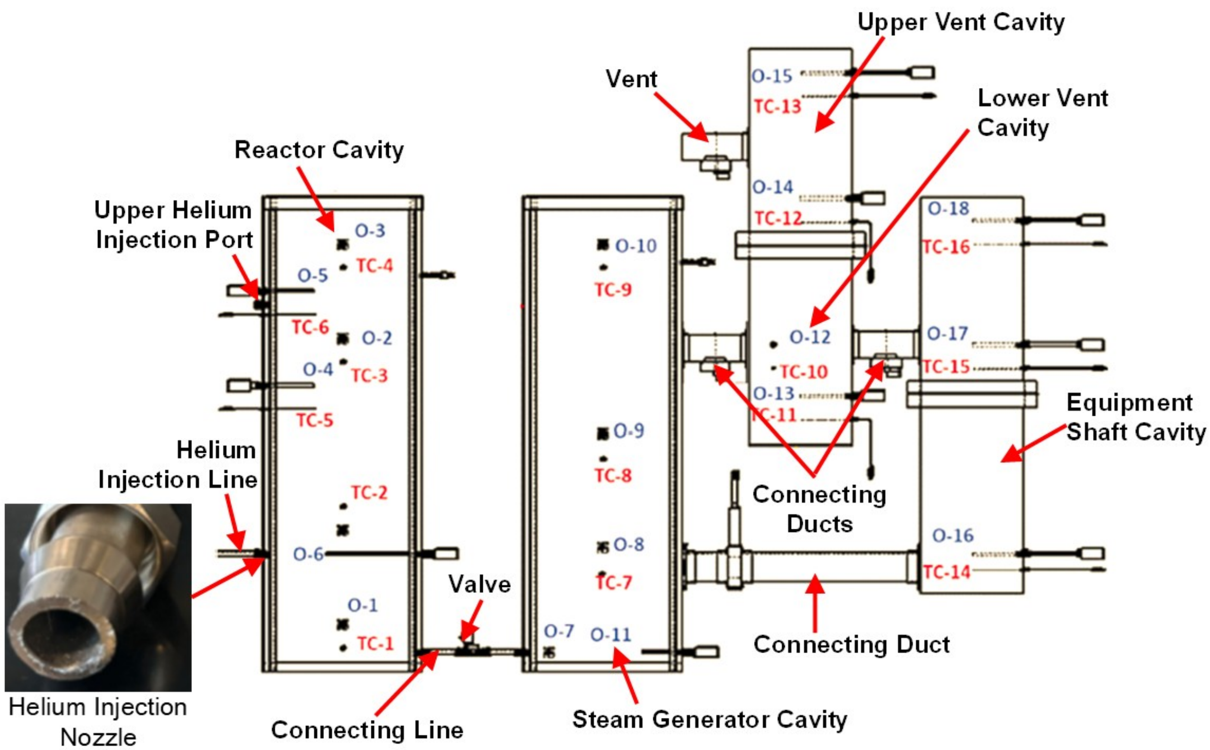


**Fig. 2.4:** CCNY RCTF He-air gas mixing facility showing arrangement of cavities and locations of thermocouples (TC) and oxygen sensors (o) (modified from Abubakar et al. [2024]).

The CCNY facility is designed to replicate a hypothetical small pipe rupture in the primary loop of an HTGR, resulting in the release of high temperature, pressurized He from the reactor vessel into the surrounding and connected cavities. The He feeding pipe is heated to increase the room-temperature He flow exiting a gas cylinder to the desired injection temperature into the reactor cavity, up to 873 K (600 °C) [Abubakar et al. 2025]. More details of the thermal-hydraulics analyses of the He feed tube are given in Appendix A.

The cabinets representing the various cavities in Fig. 2.4 are instrumented with TCs and OSs mounted to the walls of the cavities at different axial locations, besides a fiber-optic distributed temperature sensor in the reactor cavity (Fig. 2.4). The performed experiments investigated the effects of the He injection temperature and flow rate, and the injection nozzle geometry on the He-air mixing and the stratification within the cabinets representing the various containment cavities in a HTGR plant. [Abubakar et al. 2024, 2025]. Also investigated is the effect of the axial location of the He injection through the upper and lower ports in the reactor cavity on these results (Fig. 2.4) [Abubakar et al. 2024].

Hot He injection through the lower port on the side of the reactor cavity improved He-air mixing in the cavity. The hot He injection through the upper port of the reactor cavity resulted in extensive He stratification, with more of the injected He present at the top of the cavity. Results also showed that changing the hot He injection velocity and/or the orientation of the injection nozzle affected the He-air mixing and the gas-mixture stratification in the reactor cavity [Abubakar et al. 2025]. A hot He injection velocity of 50 m/s through a circular nozzle led to greater stratification in the reactor cavity. On the other hand, a higher injection velocity of 120 m/s for the hot He through a rectangular nozzle resulted in greater mixing and less stratification in the reactor cavity. Orienting the opening in the injection nozzle upwards induced less overall mixing, while orienting the opening downward promoted He-air mixing in the reactor cavity [Abubakar et al. 2025].

Liu et al. [2025] performed CFD simulation analyses of the He-air mixing in the CCNY RCTF facility, including the reactor and steam generator cavities. They used the Code_Saturne [Fournier 2011] CFD code with the Unsteady Reynolds Average Navier Stokes (URANS) Shear Stress Transport (SST) k-ω turbulence model to investigate the effects of nitrogen and the He gas injection. The analyses that accounted for heat losses from the exterior of the steel walls of the cavities, using a convective boundary condition with a specified ambient air temperature, were only for the reactor cavity (cavity 1). They did not account for the period in the experiment during which the valve separating cavities 1 and 2 remains closed (Fig. 2.4). The results predicted that the plume from the jetting hot He into the reactor cavity would rise due to buoyancy in the initially air-filled reactor cavity. The calculated temperatures and oxygen concentrations show significant discrepancies relative to the reported experimental measurements early in the simulated transient. These differences diminished with increasing transient time, when predictions agreed with the reported temperature and oxygen concentration measurements to within ~1% and ~5%, respectively [Liu et al. 2025].

Experimental investigations, such as those by Abubakar et al. [2024, 2025] at CCNY, provide valuable insights into the mixing dynamics of He and air in the compartmentalized reactor and steam generator cavities. However, the discrete sensor measurements in the experiments cannot provide a complete view or characterization of the complex gas mixing within the cavities, which can be obtained through CFD simulations. When guided by reported experimental measurements, such analyses can provide insight into the flow dynamics of pressurized, high-temperature He injection into the air-filled cavities during the simulated blowdown phase of a DLOFC accident. However, ensuring solution convergence in CFD simulations requires systematic benchmarking against experimental results, which is the focus of the present work conducted at the University of New Mexico's Institute for Space and Nuclear Power Studies (UNM-ISNPS). This work presents CFD simulation analyses of the CCNY experiments to investigate He-air mixing in cavities 1 and 2 of the scaled RCTF at CCNY (Fig. 2.4). The specific research objectives are detailed next.

### *2.2 Research Objectives*

The objectives of this research are to numerically investigate the He-air mixing in the various containment cavities of an HTGR during the blowdown phase of a simulated DLOFC accident. The results of the present CFD simulation analyses, performed using the STAR-CCM+ commercial code [Siemens PLM 2023], are compared with the reported measurements from the RCTF experiments conducted at CCNY [Abubakar et al. 2024]. The present CFD analyses investigate the effects of the implemented turbulence model, numerical mesh refinement, time-step size, and hot He inlet flow conditions on the CFD simulation results. These include the pressure in cavity 1 and the spatial distributions of temperature and oxygen concentration in cavities 1 and 2. The comparison of the effects of using the Large Eddy Simulation (LES) turbulence model and the Shear Stress Transport (SST) k-ω Reynolds Averaged Navier-Stokes (RANS) model on the results of the CFD simulation analyses of the CCNY experiments.

The simulation analyses performed model: (a) the initial portion of the blowdown phase, with the valve isolating the reactor cavity from the steam generator cavity closed, and (b) the subsequent period after the isolation valve opens and the He-air mixture flows out from the reactor cavity, into the steam generator cavity. The obtained results and spatial distribution images of the flow field quantify He-air mixing, stratification, and species transport within the connected cavities during the simulated DLOFC transient. The results include the spatial distributions of oxygen, temperature, gas-mixture velocities, and gas-mixture pressure in the reactor and steam generator cavities.

# Chapter 3 – Methodology and Approach: Cavity 1

This section outlines the methodology for simulating the transient DLOFC accident experiment performed at the RCTF facility of the CCNY [Abubakar et al. 2024 and 2025]. The CFD simulation analyses use the commercial STAR-CCM+ CFD code [Siemens PLM 2023] with the LES and RANS turbulence models. The portion of the transient analyzed is the initial period of the simulated blowdown phase, before the isolation valve opens and connects the reactor cavity to the steam generator cavities (cavities 1 and 2). Analyses model the scaled reactor cavity in the experiments conducted by Abubakar et al. [2024 and 2025], including the stainless-steel walls. Fig. 3.1 shows various section views of cavity 1, indicating the locations of the oxygen and temperature sensors mounted on the inside of its walls.

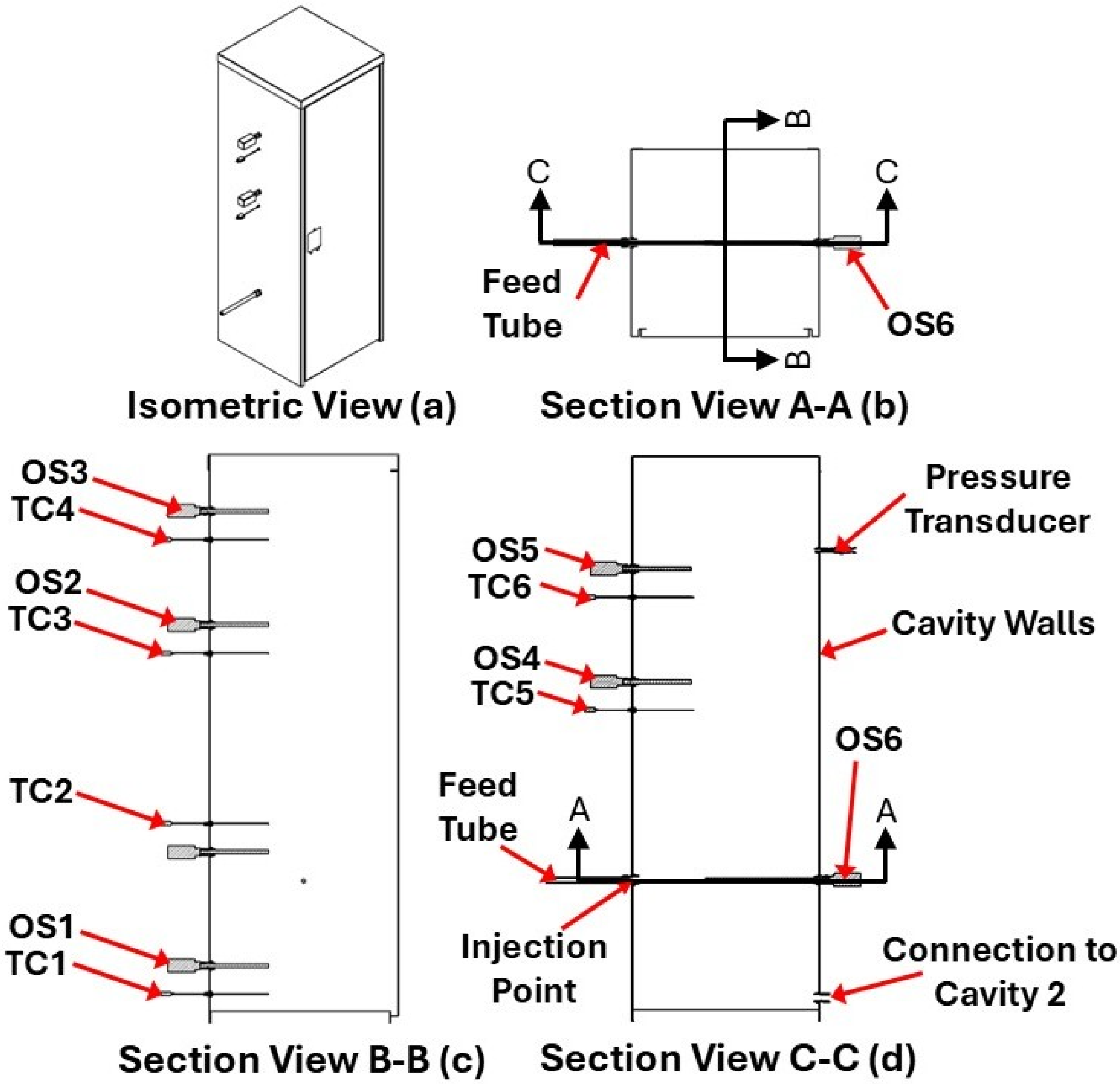


**Fig. 3.1:** Section views with the temperature and oxygen sensors mounted on the inside of the walls of Cavity 1 in RCTF test facility.

### *3.1 Approach*

The injected hot He gas mixes with the air initially present in cavity 1. These gas species are approximated as ideal gases, and their diffusive mixing within the cavity is modeled using the multi-component non-reacting gas model [Siemens PLM 2023]. The CFD simulation analyses using the STAR-CCM+ CFD commercial code [Siemens PLM 2023] and two separate turbulence models are used to handle the transient He-air mixing in cavity 1. These are: (a) the Large Eddy Simulation (LES) turbulence model with the Wall-Adapting Local Eddy-viscosity (WALE) subgrid-scale model, and (b) the Shear Stress Transport (SST) k-ω Reynolds

Averaged Navier-Stokes (RANS) model. Both turbulence models incorporate the all y+ wall treatment model [Siemens, 2023].

### *3.1.1 Assumptions and Boundary Conditions*

The specific heat and thermal conductivity of 316 stainless steel are evaluated using polynomial functions of temperature [Mills, 2002], and the material properties of both air and He are determined as functions of temperature at atmospheric pressure. The molar masses of air and He are taken as 28.9586 g/mol [Lemmon et al., 2000] and 4.002602 g/mol [Ortiz Vega et al., 2023], respectively. The temperature-dependent dynamic viscosity and thermal conductivity of air are those reported by Kadoya et al. [1985]. The dynamic viscosity and thermal conductivity of He are taken from values reported by Arp et al. [1998]. The specific heat values for He and air are defined using isobaric (1 atm) temperature correlations from Ortiz Vega et al. [2023] and Lemmon et al. [2000], respectively. The diffusivity of He in air (at atmospheric pressure) is based on the temperature-dependent correlation by Marrero and Mason [2009]. The dynamic viscosity, specific heat, and thermal conductivity of the He-air mixture are determined as molecular mass-weighted averages. The density of the He-air mixture is calculated from the mixture's molecular weight. The turbulent Prandtl and Schmidt numbers are both set equal to 0.9, which is recommended for conventional fluids [Siemens PLM 2023].

The outer surfaces of the stainless-steel cavity walls are treated as fully insulated (adiabatic boundaries), while heat exchange is permitted at the inner wall surface with the gas mixture inside the cavity. The modeled He injection into the cavity uses a 20-diameter entrance length to develop the flow as it would have been in the feed pipe before it reaches the injection point. In the experiment, the feed tube consists of two sections (See Appendix A), a heated Inconel section followed by a smaller diameter insulated stainless-steel section. The He mass flow rate at the inlet of this entrance length is assumed uniform. The time-varying mass flow rate and temperature of the injected helium into Cavity 1 are those reported in the experiments by Abubakar et al. [2024]. Finally, the cavity volume is initially assumed to be filled with ambient air.

### *3.1.2 Numerical Mesh Grid and Turbulent Parameter Estimates*

The numerical mesh grid for the cavity walls employs the polyhedral mesher with the thin mesher option to generate parallel prismatic layers across its width. Additionally, a single prism layer is applied at the inner wall surface to accurately calculate the thermal gradient at the solid-gas interface and in the adjacent gas boundary layer. (Fig. 3.3). The base size for the solid wall meshes is 5 mm, with the prism layer being 0.2 mm thick, yielding a mesh grid with 1,093,619 cells in the cavity 1 walls (Table 3.1 and Figs. 3.2 and 3.3).

**Table 3.1:** Cavity solid wall mesh parameters.

| Parameter | Value | Units |
|---|---|---|
| Base Cell Size | 5 | mm |
| Number of Thin Layers | 2 | None |
| Number of Prism Layers | 1 | None |
| Total Prism Layer Thickness | 0.2 | mm |
| Total Grid Count | 1,093,619 | Cells |

To resolve turbulent structures, the RANS turbulence model does not require as refined a numerical mesh grid as the LES turbulence model [Rodriguez 2019]. To ensure sufficient refinement of the LES turbulence model, a base mesh for the fluid region in cavity 1 is generated using the core mesh cell size λ, which equals the approximated Taylor eddy size. The Taylor eddy size, also known as the Taylor microscale, is the length scale above which turbulent structures in LES turbulence models are theoretically fully resolved. Turbulent structures resolved by an LES model are within the energy-containing and inertial subranges of the Kolmogorov energy spectrum, which correspond to integral and Taylor eddies, respectively. In the LES model, the smallest and lowest-energy eddies, known as the Kolmogorov eddies, are modeled using a subgrid-scale model [Nicoud and Ducros 1999]. Since the Taylor microscale in the experiment cannot be directly calculated, it is therefore estimated using the LIKE algorithm, as outlined by Rodriguez [2019]. The results of utilizing the LIKE algorithm for the hot He injection in cavity 1 in the present CFD simulation analyses are shown in Table 3.2.

**Table 3.2:** LIKE Results for hot He injection into Cavity 1.

| LIKE Jet Parameter | Value | Units |
|---|---|---|
| Characteristic Length (Inlet Diameter) | 13.8 | mm |
| Characteristic Velocity (Average Inlet Velocity) | 23.8 | m/s |
| Reynolds Number | 603 | Dimensionless |
| Integral Eddy Size | 10.7 | mm |
| Taylor Eddy Size | 5.28 | mm |
| Kolmogorov Eddy Size | 0.659 | mm |

From experimental studies of the turbulent properties of free jets, it has been found that the integral eddy scale is approximately the same as the characteristic length of the jet orifice at the orifice exit [El-Gabry et al., 2014]. While this is for a free jet, the diameter of the stainless-steel section of the feeding pipe provides a baseline for the integral eddy scale at the injection point into cavity 1. The pipe inner diameter of 13.8 mm compares well with the value of 10.7 mm calculated using the LIKE algorithm (Table 3.2). El-Gabry et al. [2014] experimentally found that the turbulent length scales for a jet decrease as the fluid moves further from the jet injection orifice. Preliminary analyses used a base mesh size slightly lower than the Taylor Eddy Size of 7.5 mm to uniformly mesh the entire cavity, in which the injection jet penetrated straight to the opposite wall without expanding. Experimental work [Settles and Liberzon 2022] has shown that, for jetting He into air, the jet diameter increases further downstream of the injection orifice, suggesting that further mesh refinement is necessary.

To better capture the physics of the injection He jet in cavity 1, the present analyses use two concentric cylindrical mesh-refinement regions. Both regions are centered on the He injection nozzle into the cavity. Considering the turbulent parameters approximated by the LIKE algorithm and the expected decrease in turbulent length scales shortly beyond the injection point, the refinement sizes of the two cylindrical regions were determined. These regions are meshed using a hexahedral core mesh with prism layers on all surfaces contacting the solid cavity walls. The total thickness of the prism layers is 1 mm in all regions, each with 5 sublayers and a 1.2 stretching ratio.

The fluid domain is then split into three separate regions, using two concentric cylinders. A fine mesh refinement cylinder with a diameter of 100 mm, extending 250 mm into the cavity from the wall, with a cell size of 1.25 mm. A medium mesh refinement cylinder with a diameter of 300 mm that extends 450 mm into the cavity from the wall and is meshed with a cell size of 2.5 mm. The remaining cavity is meshed with a base cell size of 7.5 mm. The total count for the entire cavity is 4,700,394 cells. The total cell counts in the medium and fine refinement cylindrical regions, and the rest of cavity 1 are of 910,766, 1,204,806, and 2,584,822 cells, respectively (Fig. 3.2, Fig. 3.3, and Table 3.3).

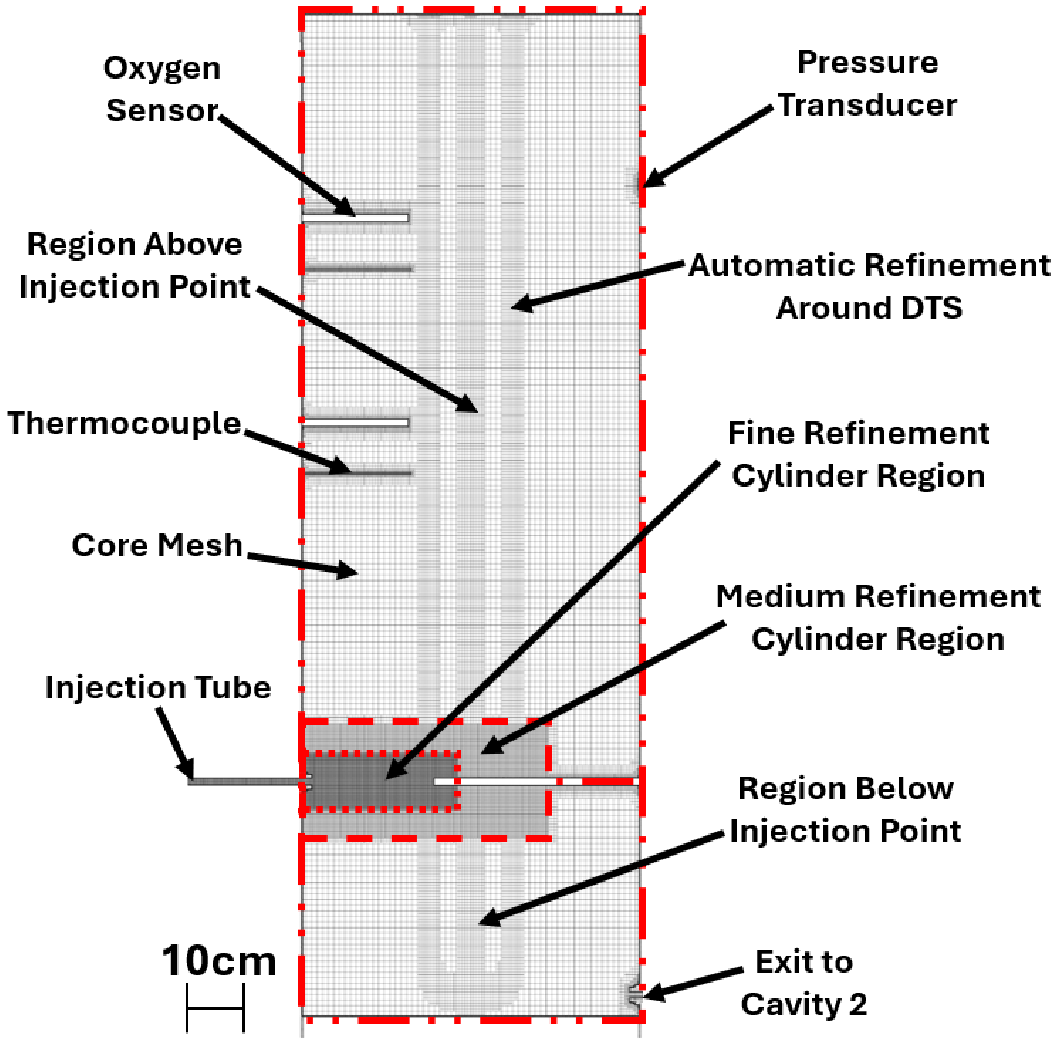


**Fig. 3.2:** Section view C-C of the implemented numerical mesh grid in present CFD simulation analyses of cavity 1 in the RCTF.

**Table 3.3:** Cavity fluid region mesh parameters.

| Region | Parameter | Value | Units |
|---|---|---|---|
| All Regions | Number of Prism Layers | 5 | None |
| | Total Prism Layer Thickness | 1 | mm |
| | Stretching Ratio | 1.2 | None |
| | Total Cell Count | 4,700,394 | Cells |
| Regions Above and Below the Injection Point | Base Cell Size | 7.5 | mm |
| | Total Cell Count | 2,584,822 | Cells |
| Medium Refinement Cylinder Region | Base Cell Size | 2.5 | mm |
| | Total Cell Count | 910,766 | Cells |
| Fine Refinement Cylinder Region | Base Cell Size | 1.25 | mm |
| | Total Cell Count | 1,204,806 | Cells |

### *3.2 Adaptive Time Step Scheme*

The present CFD simulation analyses use an adaptive time step that varies based on the calculated Courant-Friedrichs-Lewy (CFL) number. The CFL number is a metric that determines how many cells a parcel of fluid traverses in a single time step [Courant et al., 1967]. Rodriguez [2019] recommends a minimum CFL of 5 for implicit CFD solvers, while Molkov and Shentsov [2014] report good results for modeling gas release into an enclosure with a CFL of ~30 for similar injection Re. The present analyses for cavity 1 use a CFL limit of 20 to ensure numerical stability during the simulated transient without incurring prohibitive computational cost.

For the adaptive time-stepping scheme used, the minimum and maximum time steps are set to 0.000001 and 0.001 seconds, respectively, and the CFL limits of 1, 5, 20, 40, and 100 are investigated. Similar pressures and spatial distributions of velocity, temperature, and oxygen concentration in cavity 1 are obtained in analyses with CFL values of 1, 5, 20, and 40. With a CFL = 100, the results differed significantly. The simulated 22-second transient is ~30x computationally more expensive with a CFL limit of 1 than with a limit of 20.

While results do not differ greatly between CFL limits of 20 and 40, the present simulation analyses use a CFL limit of 20. The CFL limit of 5, while preferred, is found to be computationally expensive for running multiple cases. Additionally, the lower CFL limit reduces the temporal discretization error and provides a wider margin of solution stability for the solvers. Comparative testing with a static time step of 0.0001s shows that the adaptive time step scheme reduces the total calculation time by 41% while yielding results similar to those with the static time step.

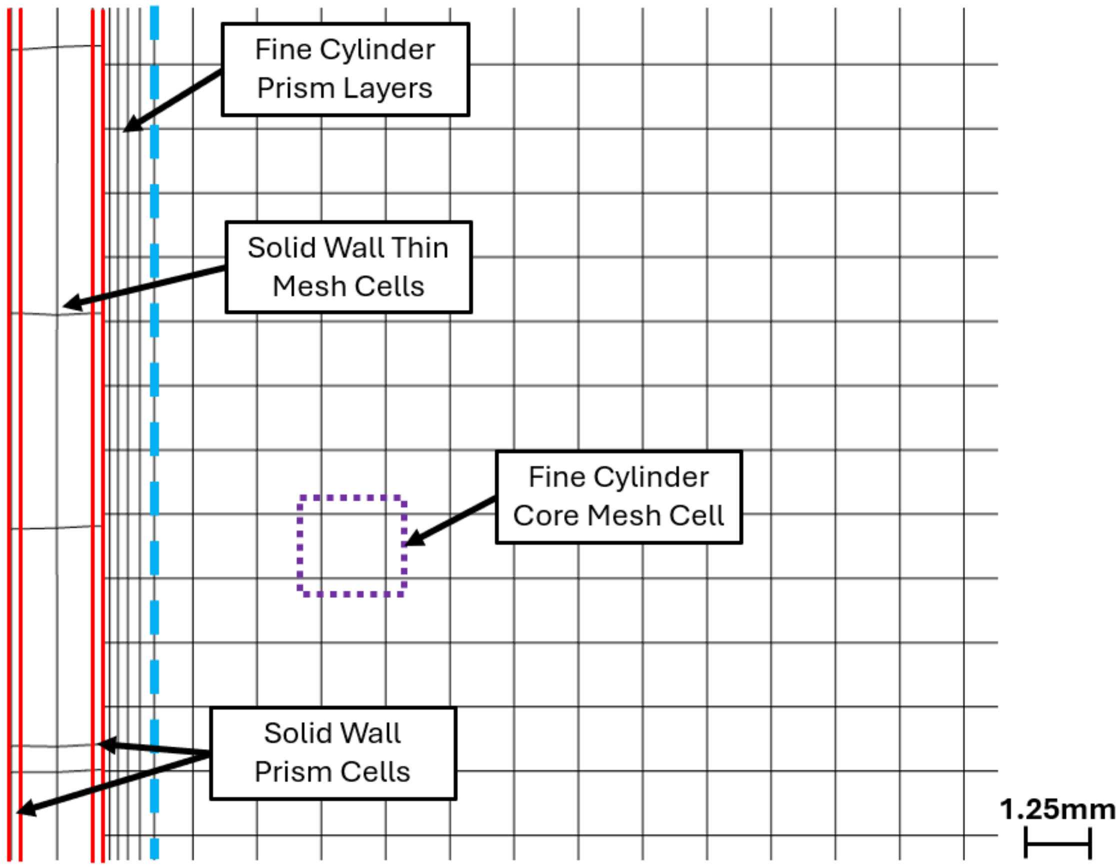


**Fig. 3.3**: Section view of numerical mesh within the fine refinement cylinder region.

### *3.3 Numerical Grid Turbulence Resolution*

The numerical mesh grid refinement for the LES turbulence model is evaluated using the recommended criterion by Pope [2004]. Pope suggests that the calculations with the LES model should resolve ~80% of the turbulent kinetic energy. The 20% remaining is calculated using a subgrid-scale model. The calculated resolved fraction of the total turbulent kinetic energy using the subgrid-scale model, R, is expressed in terms of the resolved turbulent kinetic energy, $k_{res}$, and the calculated turbulent kinetic energy, $k_{sgs}$, as:

$$R = \frac{k_{sgs}}{k_{res}+k_{sgs}} \tag{3.1}$$

In this expression, the sum ($k_{res}$ + $k_{sgs}$) is the total turbulent kinetic energy. Values of R close to zero correspond to a more resolved simulation, which is considered more like a Direct Numerical Simulation (DNS). On the other hand, values of R close to 1 correspond to a less resolved simulation using a Reynolds Averaged Navier-Stokes (RANS) turbulence model. For high R values, most of the turbulent kinetic energy is modeled using the subgrid-scale model.

The greatly varying conditions in cavity 1 during the transient when hot helium is injected into the cavity mean that different regions will experience varying degrees of turbulence resolution. The LES turbulence resolution assessed using the parameter R, is evaluated for five distinct regions within the computational domain (Fig. 3.2): (a) the entire cavity, (b) the region above the injection point of Hot helium into the cavity, (c) the region below the injection point, (d) the medium refinement cylindrical zone surrounding the helium jet into the cavity, and (e) the fine refinement cylindrical zone. Table 3.4 presents the resolved turbulent kinetic energy $k_{res}$, the subgrid-scale calculated turbulent kinetic energy $k_{sgs}$, and the values of R for each region (Eq. 3.1).

**Table 3.4:** Turbulent kinetic energy parameters of various regions in the reactor cavity.

| Region | R | Total Subgrid-Scale Turbulent Kinetic Energy, $k_{sgs}$ (J/kg) | Total Resolved Turbulent Kinetic Energy, $k_{res}$ (J/kg) |
|---|---|---|---|
| Entire Cavity | 0.00379 | 32983 | 8674753 |
| Below Injection Point | 0.356 | 332.6 | 601.4 |
| Above Injection Point | 0.248 | 832 | 2524 |
| Medium Refinement Cylinder | 0.0146 | 621 | 41928 |
| Fine Refinement Cylinder | 0.0036 | 31197 | 8629700 |

The results demonstrate that 99.5% of the turbulent kinetic energy in cavity 1 resides within the fine refinement cylinder, which encompasses the core of the expanding He jet (Table 3.4). The value of R in this region of 0.0036 indicates that nearly all the turbulent kinetic energy is resolved, which confirms adequate resolution of the jet turbulence. The medium refinement cylinder shows the next smallest R value, consistent with its proximity to the primary mixing region of hot helium and air in cavity 1. The upper and lower cavity regions yield higher R values (> 0.2), but the turbulent kinetic energy is much lower than in the most refined mesh regions in the cavity. The low overall R value for the entire cavity of 0.00379 suggests that the implemented numerical mesh grids in the present simulation CFD analyses with the LES turbulence model are sufficiently fine to resolve the turbulence [Pope 2004]. A sufficiently refined numerical mesh grid for an LES turbulence model is also adequate for analyses with the RANS turbulence model, given the less stringent mesh cell size requirements imposed by the turbulent length scales in the flow.

# Chapter 4 – Results and Discussion: Cavity 1

The present CFD analyses simulate four distinct variations of the No. 6 Experiment reported by Abubakar et al. [2024] to investigate the effects of the He injection rate, the initial reactor cavity temperature on He-Air mixing, and the spatial distributions of temperature and oxygen concentration in Cavity 1. The four CFD cases simulated are labeled A-D in Table 4.1. Cases A and C are for an isothermal initial cavity temperature of 22.5°C, derived from reported measurements of the distributed temperature sensor (DTS) in the experiment prior to hot He injection into cavity 1, which is initially air-filled. Cases B and D are for a spatially varying temperature field within cavity 1 based on the reported thermocouple data in the experiment [Abubakar et al., 2024], Fig. 4.1a.

The present CFD simulations linearly interpolate local temperature values from the reported thermocouple measurements. Cases A and B are for the reported flow rate of the injected hot He into cavity 1, while Cases C and D are for a 10% lower flow rate to account for the thermal losses to the cavity walls via the enthalpy of the injected He, which were not measured in the experiments but calculated based on an energy balance of cavity 1. All four cases use the measured transient temperature values of the injected He into cavity 1. This temperature is recorded by the immersed thermocouple in the feeding pipe (Fig. A1.1 in Appendix A) in the experiments.

**Table 4.1:** Input to CFD analyses.

| CFD Cases | Cavity Initial Temperature (°C) | He Injection Flow Rate (g/s) | He Injection Temperature (°C) |
|---|---|---|---|
| A | Uniform = 22.5 | Experimental Data, Fig. 1b | Experimental Data, Fig. 4.1c |
| B | Thermocouple Data, Fig. 4.1a | Experimental Data, Fig. 1b | Experimental Data, Fig. 4.1c |
| C | Uniform = 22.5 | Experimental Data + Account for Wall Heat | Experimental Data, Fig. 4.1c |
| D | Thermocouple Data, Fig. 4.1a | Experimental Data + Account for Wall Heat | Experimental Data, Fig. 4.1c |

Fig. 4.1 presents the recorded initial air temperature in cavity 1, and the flow rate and temperature of the injected hot helium into cavity 1 in the Experiment [Abubakar et al., 2024]. Fig. 4.1a shows the measured initial temperatures by six thermocouples mounted at different heights within the cavity. The lowest thermocouple (TC1) records approximately 23°C, while recorded temperature increase with elevation (TC2, TC5, TC3, and TC6). The two uppermost

thermocouples (TC6 and TC4) both measure ~29.5°C. The performed CFD simulation analyses assume that the temperatures above the TC6 location are the same as this value.

Figs. 4.1b and 4.1c plot the He injection conditions during the first 22 seconds of the simulated transient, before opening the valve separating the reactor and steam generator cavities. As shown in Fig. 4.1b, the He injection flow rate increases rapidly from near zero to approximately 75% of its maximum within the first 8 seconds, then increases steadily thereafter. The He injection temperature increases from ~200°C to ~475°C, then levels off within the first ~8 seconds (Fig. 4.1c).

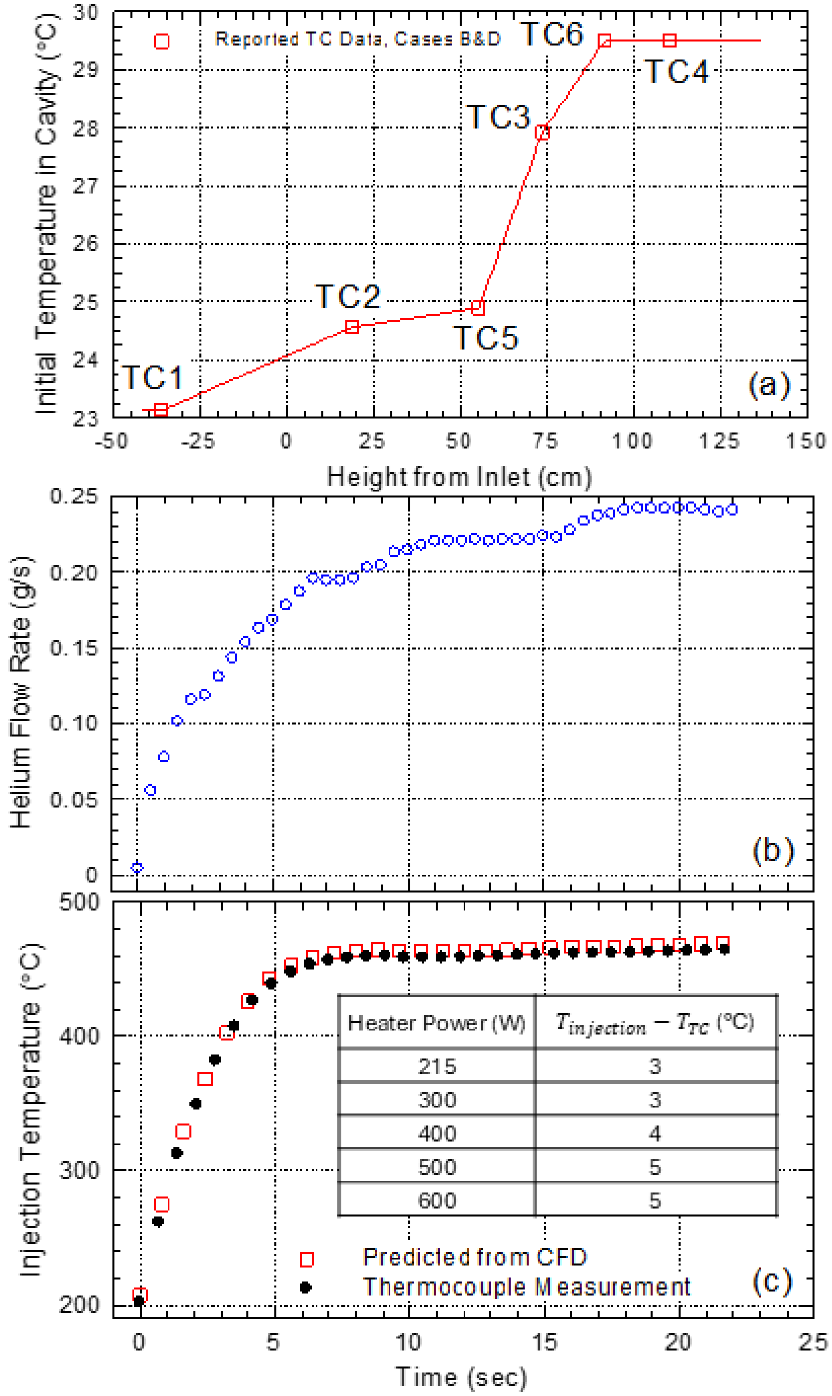


| Heater Power (W) | $T_{injection} - T_{TC}$ (°C) |
|---|---|
| 215 | 3 |
| 300 | 3 |
| 400 | 4 |
| 500 | 5 |
| 600 | 5 |

**Fig. 4.1**: Reported experimental cavity temperature and He injection conditions used in performed CFD simulations of Experiment No. 6 of Abubakar, et al. [2024]: (a) initial air temperature in cavity, (b) experiment He injection flow rate, (c) experiment He injection temperature.

### *4.1 Cavity 1 Pressure*

Fig. 4.2 plots the calculated pressure in Cavity 1 during the simulated transients for the four CFD cases in Table 4.1, along with the reported experimental measurements [Abubakar et al., 2024]. The pressure transducer (PT) located near the top of the cavity, on the wall opposite the helium injection nozzle, measures the pressure within the reactor cavity (Fig. 4.2). The present CFD simulations determine the pressure at the transducer location. Results show that the measured and calculated cavity pressures increase over time during the simulated transients. At 22 s into the transient, the measured pressure is 6.9 kPa relative to that in cavity 2 (Fig. 4.2). The CFD simulation cases consistently predict higher pressure than the experimental values, and the results show that the initial temperature distribution and accounting for the wall heat losses move the predictions closer to the reported measurements.

Fig. 4.2 shows that the results for Cases B and D, which use the thermocouple-measured cavity temperature distribution, yield lower pressure than in Cases A and C at the same hot helium injection rate. The calculated pressure for Case D yields the closest agreement with the reported experimental measurements (Fig. 4.2). The results of Case C exhibit the next best agreement with experimental measurements, followed by Case B. The results for Case A show the greatest deviation from the experimental measurements. The present CFD simulations with both the LES and RANS models yield very similar results, likely because the cavity pressure is affected little by differences in the induced turbulent mixing structures within the cavity.

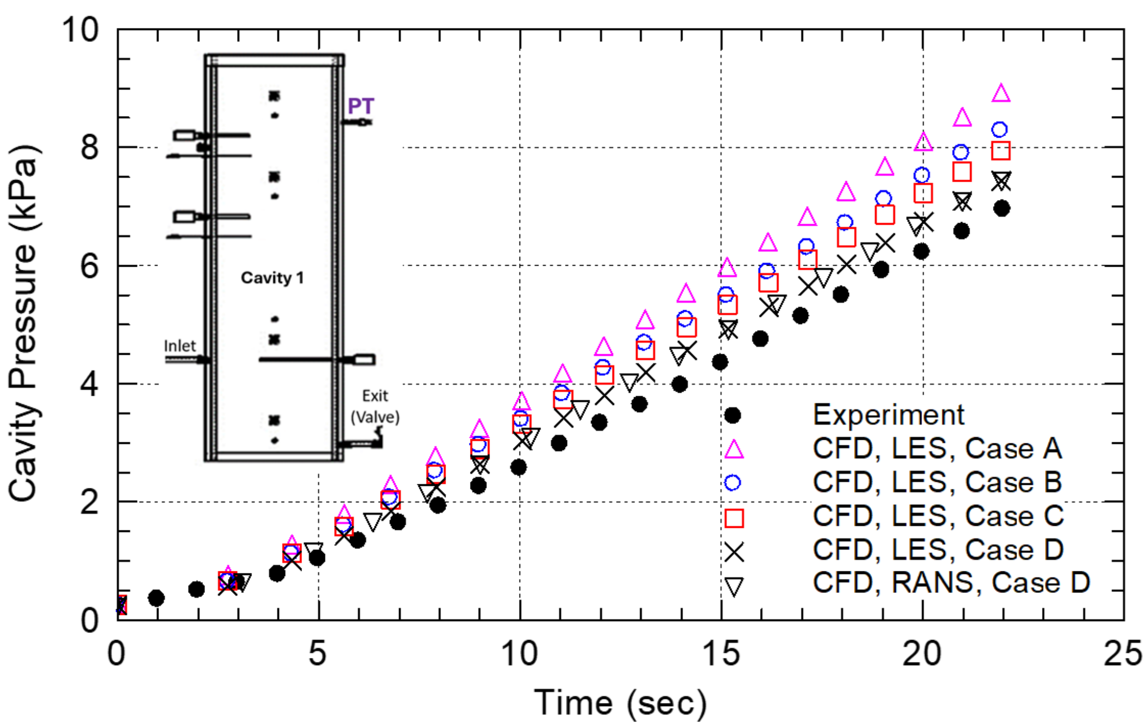


**Fig. 4.2**: Calculated transient cavity pressure for CFD Cases A-D and reported experimental measurements [Abubakar et al., 2024].

Fig. 4.3 plots the calculated CFD pressure values versus the experimentally measured values. The calculated pressure values for the CFD Case D are within +10% of the reported experimental values. The CFD results for Cases A, B, and C exhibit larger deviations, within 10 % to 30 %, compared to the reported measurements. The CFD calculated pressures with both the RANS and LES turbulence models are in close agreement for Case D. Based on the agreement with experimental pressure measurements, Case D is selected for the subsequent analyses and comparison of the calculated spatial distribution of temperature and oxygen concentration with the reported sensor measurements.

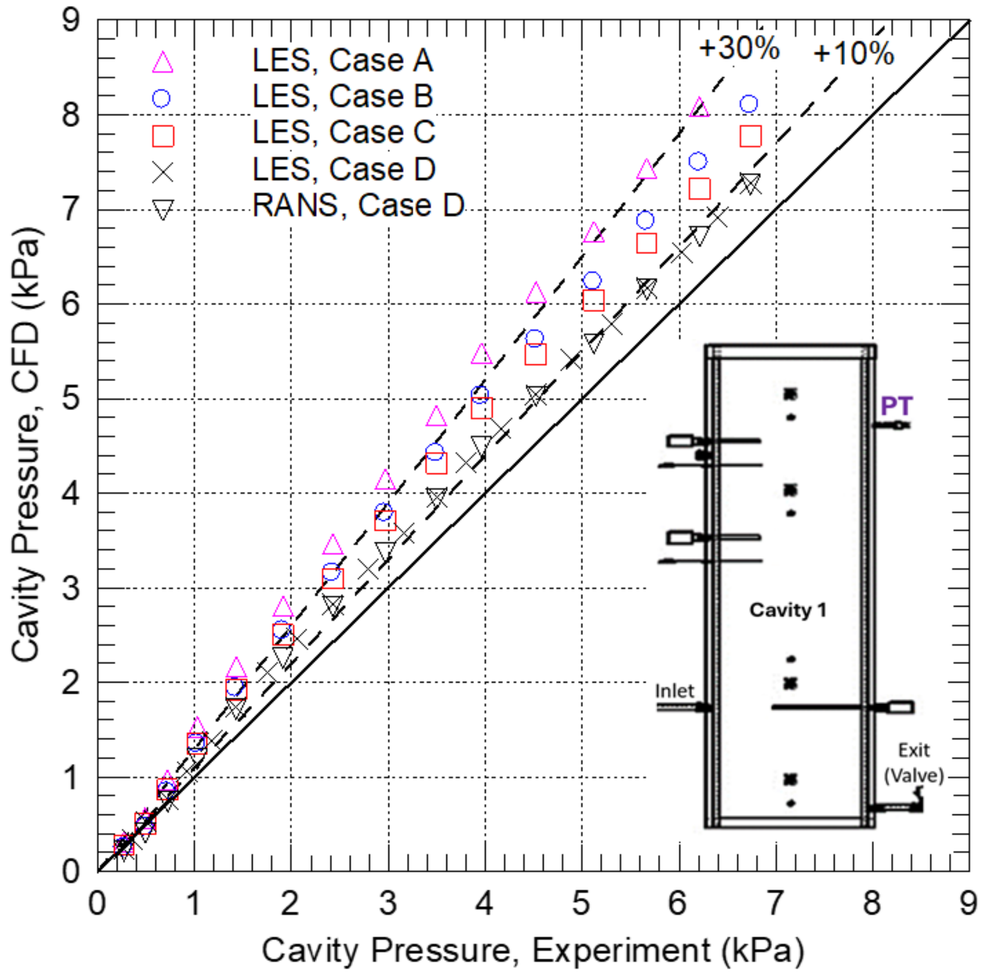


**Fig. 4.3**: Cavity pressure parity plot.

### *4.2 Flow Velocity and Mixing Eddies*

The injected hot helium into cavity 1 forms a plume of He-air mixture. Figs. 4.4 and 4.5 present velocity contours of the He-air mixture at 5, 10, 15, and 20 seconds into the simulated transient.

The images in these figures illustrate the evolution of the flow field within the cavity. The color scale in Fig. 4.4 spans the full velocity range of the simulation, whereas that in Fig. 4.5 shows a smaller velocity range, 0 to 5 m/s, to better illustrate the He-air mixing dynamics in the upper and lower sections of the cavity. The hot He injection velocity reaches ~45 m/s at the cavity entrance, then decreases rapidly with distance from the injection point as the helium jet disperses and mixes with the ambient air initially present in the cavity. The buoyancy of low molecular weight helium causes an upward curvature of the He jet toward the top of the cavity.

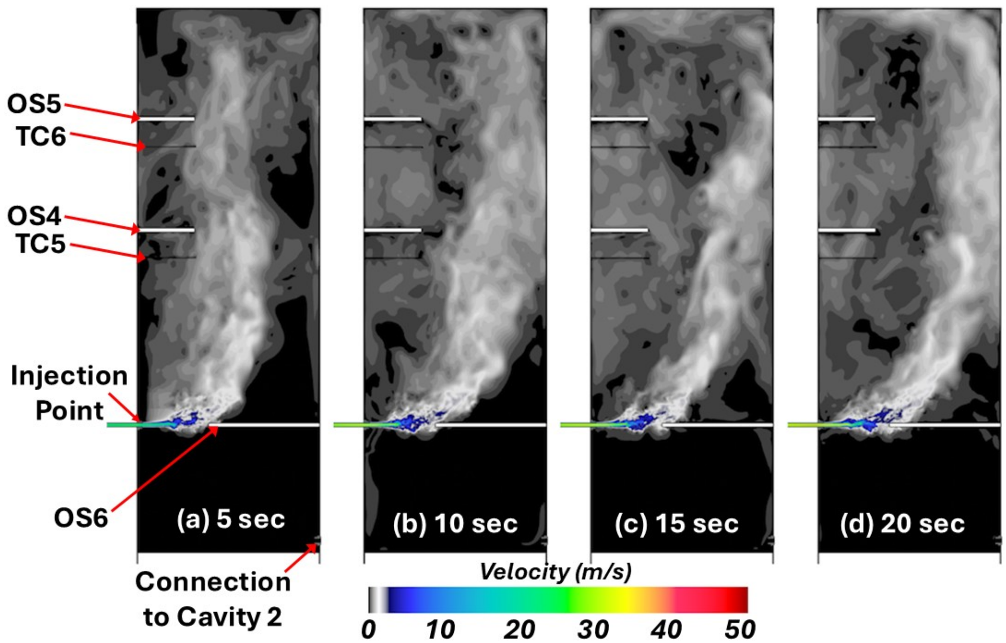


**Fig. 4.4**: Case D images of velocity fields in Cavity 1 calculated in the present CFD simulation analyses with LES turbulence model at select times; (0 to 50 m/s) full-scale color contours.

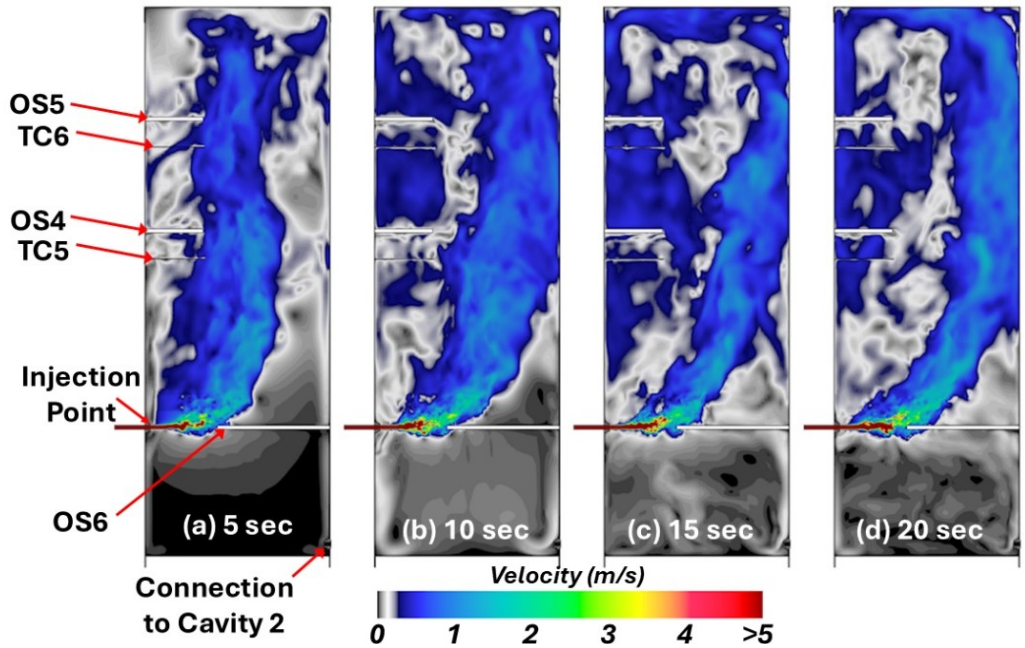


**Fig. 4.5**: Case D images of velocity fields in Cavity 1 calculated in present CFD simulation analyses with LES turbulence model at selected times; 0 to 5 m/s scale color contours.

The velocity fields in Figs. 4.4, 4.5, and 4.6 reveal counterclockwise recirculation patterns of the He-air mixture in the upper section of the cavity. The images in Figs. 4.4b-d and 4.5b-d demonstrate that the recirculation plumes become more pronounced with time during the simulated transient. The hot He-air plume forms and flows upward along the side wall, then descends along the opposite wall toward the He injection point. The calculated recirculation patterns in the CFD simulation analyses, with both the LES and RANS turbulence models are similar (Figs. 4.5 and 4.6). While the CFD simulation analyses results with the LES turbulence model show many small-scale turbulent structures, those with the RANS turbulence model show the injected He jet extending further into the cavity.

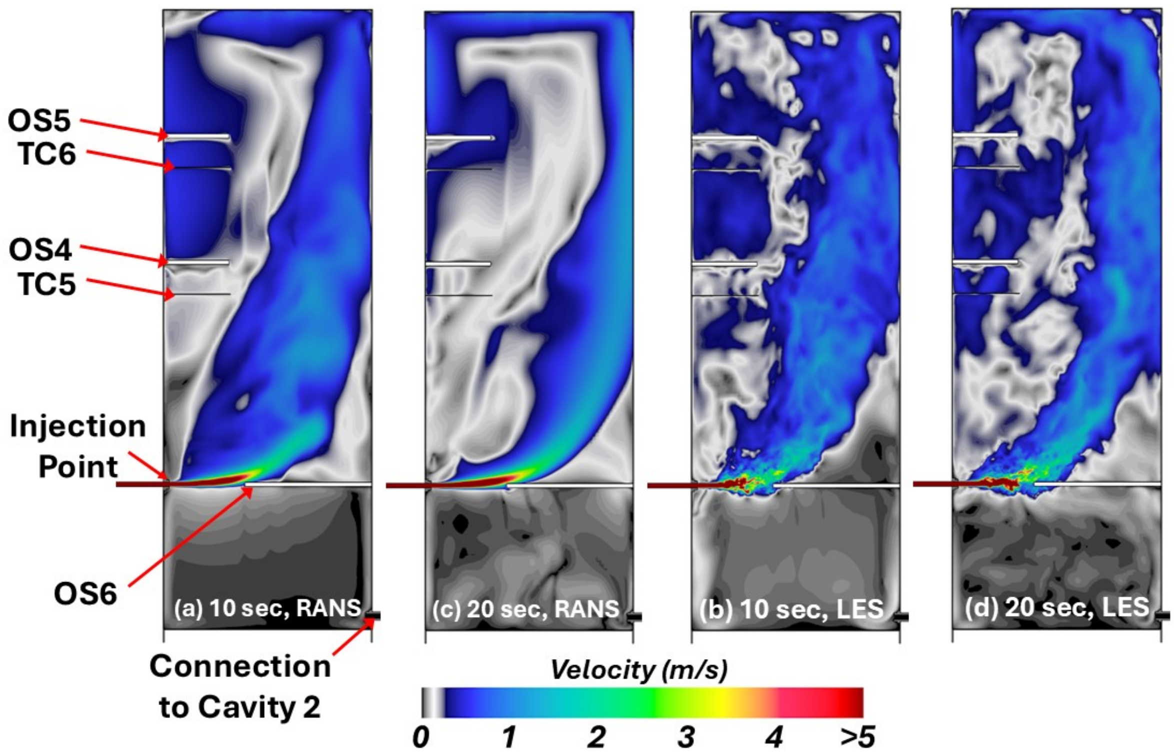


**Fig. 4.6**: Case D LES and RANS cavity velocity field comparison at 10 and 20 s during the simulated CFD transient analyses using 0 to 5 m/s Scale.

Figs. 4.5a-d show that mixing eddies develop in the lower section of the cavity as the transient progresses. However, these eddies remain small, indicating that the vertical stratification persists despite the enhanced mixing at higher flow rates. This stratification pattern has important implications for predicting He concentrations and temperature distributions during actual HTGR depressurization events.

### *4.3 Oxygen Concentration*

Figs. 4.7 and 4.8 plot the calculated 3D Q-criterion isosurfaces superimposed with the oxygen concentration to visually identify the formation of coherent turbulent structures within the cavity. The Q value, the second invariant of the velocity-gradient tensor, relates to the magnitudes of the vorticity and the rate of strain. The region where $Q > 0$ is considered a vortex tube [Hunt et al. 1988]. The use of the Q criterion to identify coherent turbulent structures is supported by the definition of Q and its relation to low-pressure zones, which are concurrent with vortex cores [Dubief and Delcayre 2000]. Both Figs. 4.7 and 4.8 for Q values of 100 show different views of the cavity at 22 s into the transient simulation. This Q value is selected based on the amount of detail discernible [Dubief and Delcayre 2000], and the coherent structures surrounding the plume are visible. As the value of Q decreases, the population of structures isolated by the isosurfaces increases. Reducing the value of Q can lead to an overpopulation of isosurfaces, making it difficult to visualize what is happening in the He-air mixing plume at the cavity center. Conversely, increasing Q can reduce the detail of coherent structures to the point that many are no longer visible.

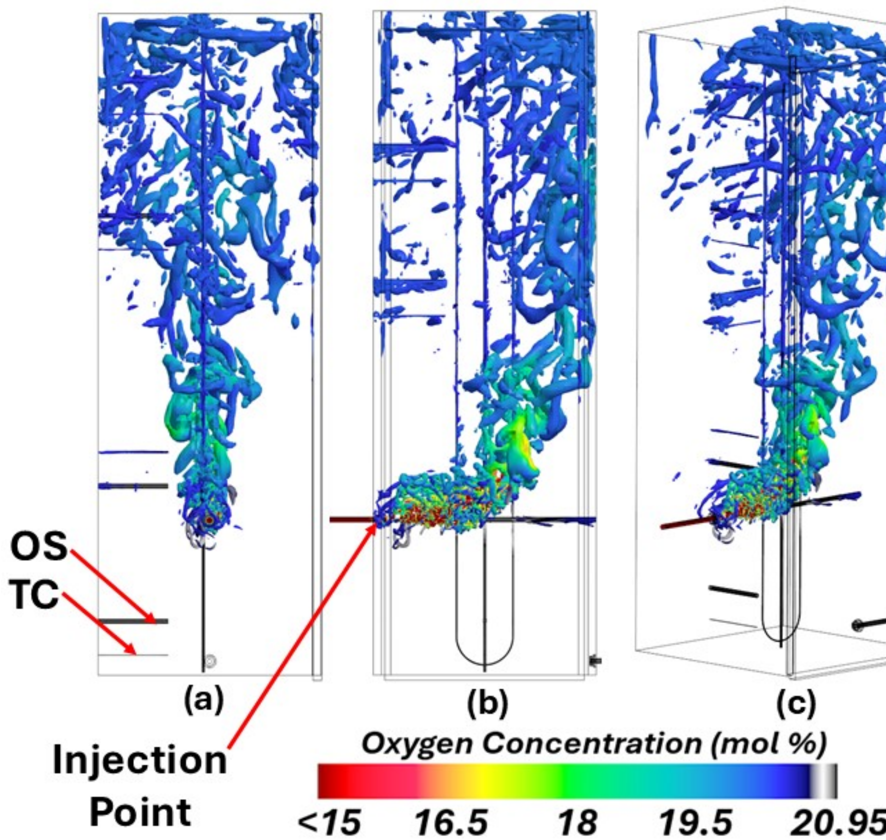


**Fig. 4.7**: Q-Criterion isosurfaces for Q = 100 with oxygen concentration contours superimposed at 22 s into the simulated transient, for case D with the LES turbulence model.

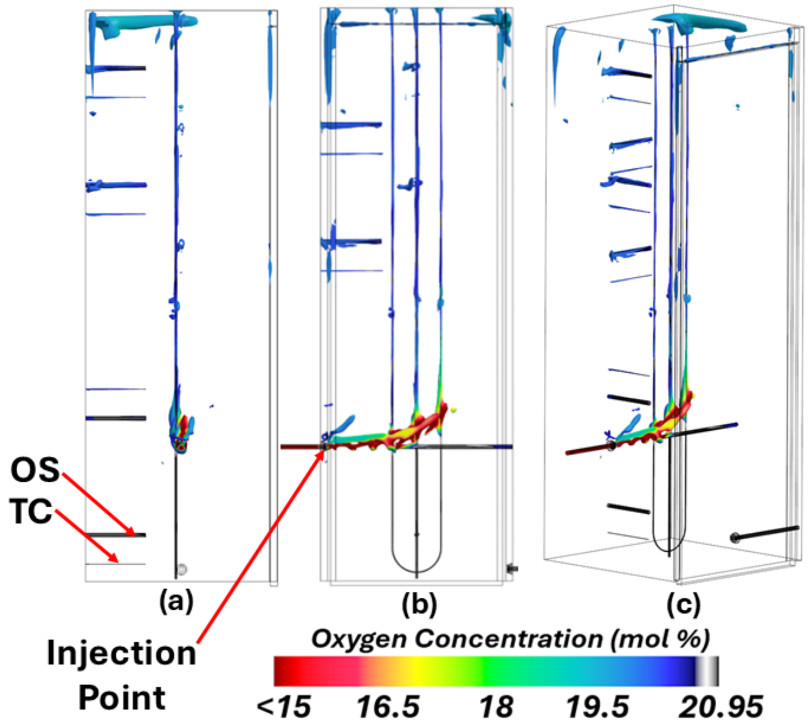


**Fig. 4.8**: Q-Criterion isosurfaces for Q = 100 with oxygen concentration contours superimposed at a time of 22 s for case D with the RANS turbulence model.

At 22s into the transient, the hot helium injection rate reaches ~0.24 g/s and has remained almost constant for nearly 5 s. Note that for a Q value of 100, many more coherent turbulent structures are identified in the LES case (Figs. 4.7 and 4.8). This is likely because more small-scale vortices are resolved in the present CFD simulation analyses with the LES turbulence model than with the RANS model. The small vortices induce small-scale mixing of He and air. The hot helium jet injected into the cavity and the surrounding turbulent structures are much less pronounced in the CFD analyses with the RANS model than with the LES model. The latter shows many more small-scale structures forming around the core of the hot helium jet (Figs. 4.7 and 4.8). In the LES analysis, the oxygen concentration results superimposed on the isosurfaces show intense He-air mixing at shorter distances from the injection point (Fig. 4.11). Additionally, the injected hot helium jet appears more diffusive in the analysis with the LES model than with the RANS model.

The oxygen concentration decreases as the injected He mixes with the air inside the cavity. Six oxygen sensors, labeled Oxygen Sensor (OS) 1-6, measure the oxygen concentration at different locations within the reactor cavity during the experiment [Abubakar et al. 2024]. Fig. 4.9 plots the oxygen concentration measurements for OS 1-6 obtained by Abubakar et al.

[2024] during the pressurization phase of the transient. As Fig. 4.9 shows, the oxygen concentrations that OS1, OS2, and OS6 measure exhibit an increase during the He injection, which is physically inconsistent with the expected dilution effect of introducing He into the air-filled cavity. Furthermore, Fig. 4.9 shows that OS1, OS2, OS5, and OS6 all have initial oxygen concentrations exceeding the ambient air value of 20.95 mol% at the start of the experiment. Similar oxygen sensor inconsistencies have been documented in comparable experimental systems (Balderrama Prieto and Arcilesi 2025 and Kultgen 2025), in which the OSs measure increased oxygen concentration due to pressures higher than that at which the sensor was calibrated. A dedicated discussion regarding these sensors in included in Appendix B. The analysis selects measurements from OS3 and OS4 for comparison with calculated oxygen concentrations from the CFD simulation. As Fig. 4.9 demonstrates, both OS3 and OS4 register initial oxygen concentrations below 20.95 mol% at the start of the hot He injection and record reduced oxygen concentrations as He injection proceeds [Abubakar et al. 2024].

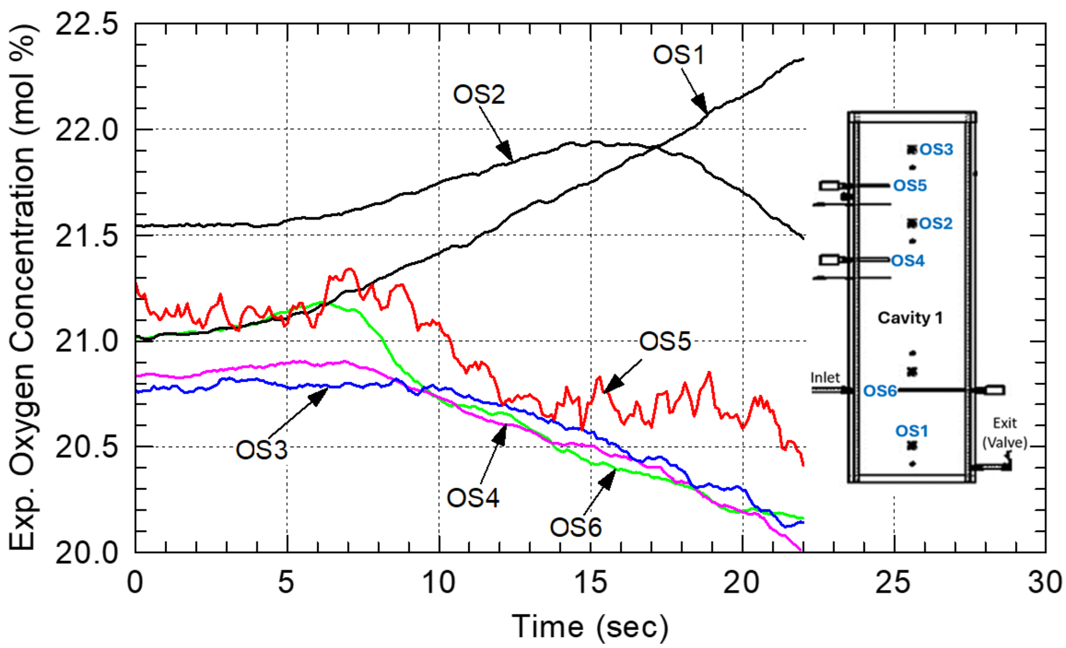


**Fig. 4.9**: Reported oxygen sensor measurements in Experiment No. 6 of Abubakar, et al. [2024].

The numerical simulation captures the spatial and temporal distributions of oxygen concentration within the cavity as the hot He injection proceeds during the simulated DLOFC transient. Figure 4.10 presents this evolution for the CFD Case D at 5, 10, 15, and 20 s into the simulated transient, demonstrating the transport and mixing of He with air in cavity 1. The color contours indicate an oxygen concentration of zero at the He-jet injection point, corresponding to pure He injection. The injected jet of hot He diffuses into the air-filled cavity, and the regions in Fig. 4.10 of lower oxygen concentration spatially correlate with higher He injection velocity (Figs. 4.4 and 4.5), reflecting the coupled momentum and buoyancy-driven transport within the cavity. At 5 s into the simulated transient, the He-air mixing plume turns sharply upward, reflecting a buoyancy-dominated flow, as shown in Figs. 4.4a and 4.5a. The oxygen concentration in the upper section of the cavity, above the injection point of the hot helium, progressively decreases over time as the injected He mixes with air (Figs. 4.10b-d). This indicates the development of a He-rich zone characteristic of stratified conditions. In contrast, results in Fig. 4.10 show that the section of the cavity below the He injection point maintains oxygen concentrations near that of ambient air, indicating that the lower section of cavity 1 remains predominantly air-filled, with almost no He.

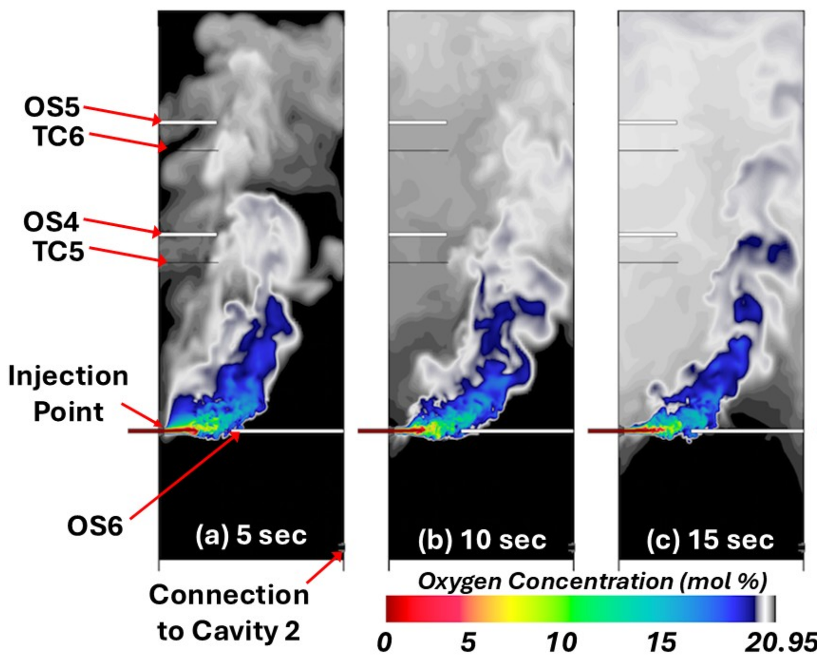


**Fig. 4.10**: Calculated progression of the oxygen concentration field in cavity 1 for Case D, CFD analyses with the LES turbulence model at select times during the simulation transient.

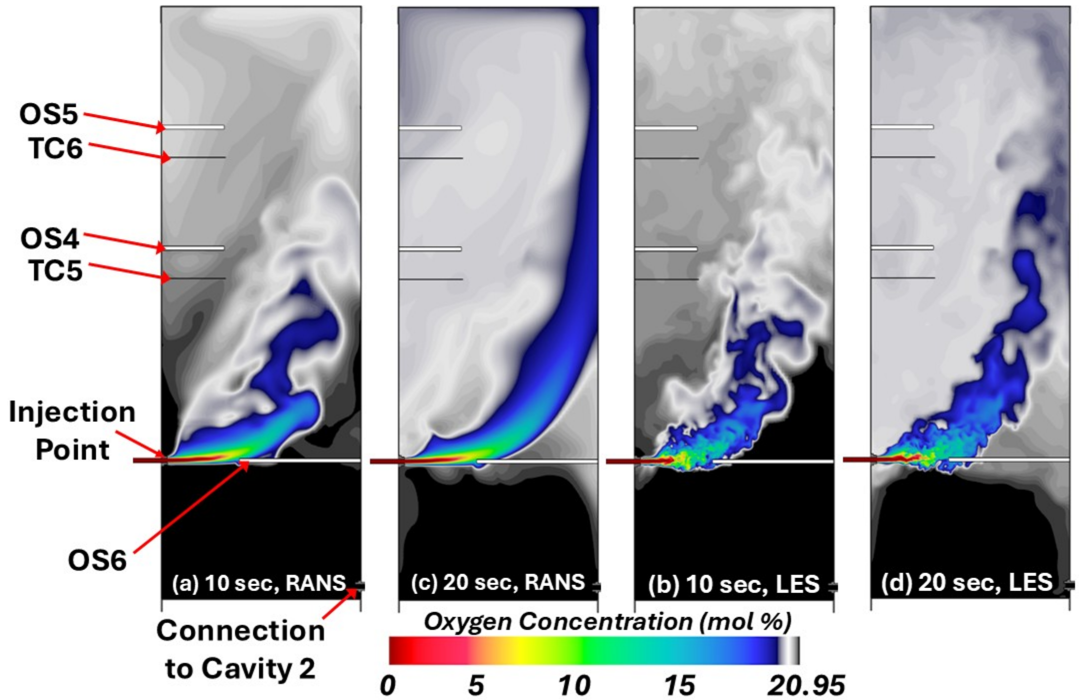


**Fig. 4.11**: Case D LES and RANS cavity oxygen concentration field comparison at 10 and 20 s during the simulated transient using 0 to 20.95 mol % scale color contours.

Fig. 4.11, which compares the results of the CFD simulation analyses using the RANS and LES turbulence models with the experimental measurements, shows that the LES model resolves many small-scale turbulent structures. This shows thorough He-air mixing near the hot helium injection point. The calculated He-air mixing in the analysis with the RANS model indicates a more He-rich mixture near the top of the cavity than with the LES model. The analysis with the RANS model predicts much less mixing. Fig. 4.12 compares the present numerical predictions of the oxygen concentration in cavity 1 with the reported experimental measurements by OS3 and OS4 sensors. Figs. 4.12a and 4.12b present the results for OS3, located higher in the cavity, and for OS4, located at a lower elevation.

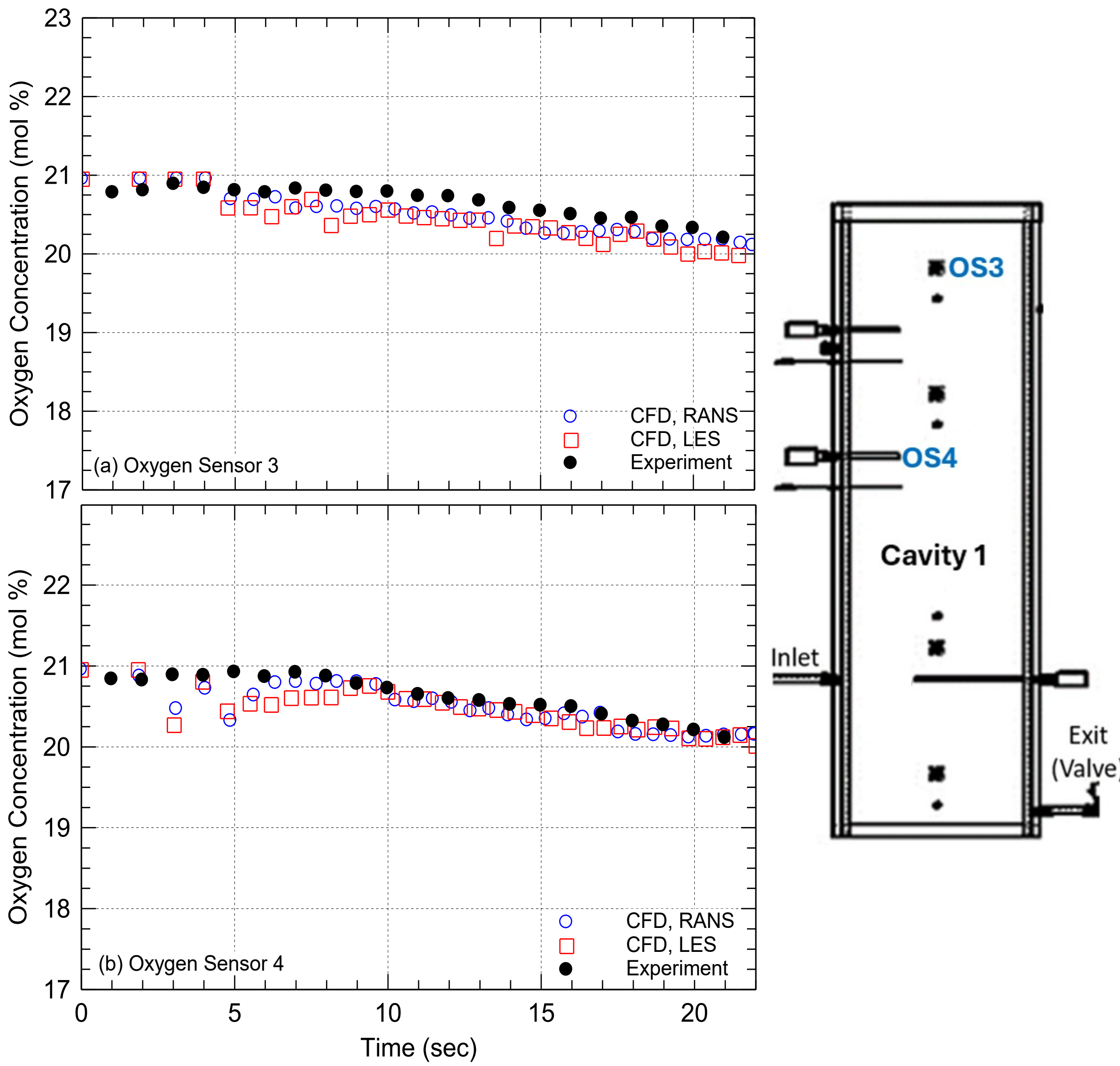


**Fig. 4.12**: Comparison of calculated and the reported oxygen concentrations in cavity 1 by Abubakar et al. [2024].

Due to the lower position of the oxygen sensor OS4 in the cavity, the He plume reaches OS4 first at ~1.8 s into the transient (Fig. 4.12b), while the plume of mixed He and air contacts OS3 later at ~4.1 seconds (Fig. 4.12a). Subsequently, both sensors indicate rapid decreases in oxygen concentration, followed by oscillatory behavior as transient mixing occurs where the sensors are in Cavity 1. The CFD simulation analyses predictions show good qualitative agreement with the reported trend of the experimental data. As shown in Figs. 4.12a-b, both exhibit similar rates of decrease in the local oxygen concentration. However, the results in these figures show that the local oxygen concentration calculated by the CFD simulation at

OS3 and OS4 begins to decrease earlier than the reported measurements indicate. This causes the calculated local oxygen concentrations to be lower than the reported experimental measurements during the simulated He injection transient. This could partially be due to the instrument delay in the measurements reported by Abubakar et al. (2024). The CFD simulation analyses with both the RANS and LES turbulence models produce similar results for the oxygen concentrations near the locations of OS3 and OS4. The most significant difference between the two models is in the He plume itself (Fig. 4.11), where the most notable difference in mixing predictions occurs. The calculated local oxygen concentrations at the OS3 and OS4 locations demonstrate excellent agreement with the reported experimental values to within ±1.5% (Fig. 4.13). The calculated values at the OS4 sensor location are slightly in better agreement with the reported measurements.

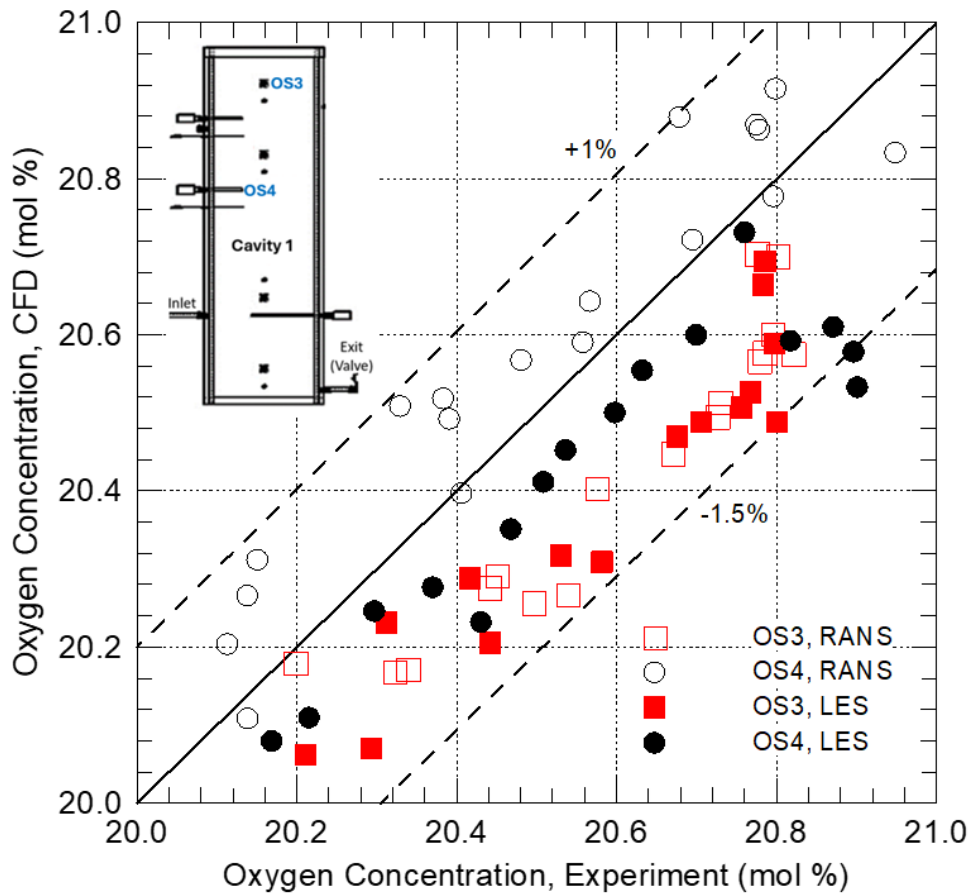


**Fig. 4.13**: Comparison of calculated local oxygen concentration for OS3 and OS4 and the reported experimental measurements of Abubakar et al. [2024].

### *4.4 Temperature*

The injected hot He into cavity 1 at temperatures ranging from 475 to 748 K (202-475°C) mixes with the ambient air initially present in the cavity. The calculated spatial temperature distributions within the cavity are similar to those of the calculated oxygen concentrations (Fig. 4.10 and Fig. 4.14). The He injection at ~748 K (475°C) creates a thermal plume within the cavity (Figs. 4.4 and 4.5).

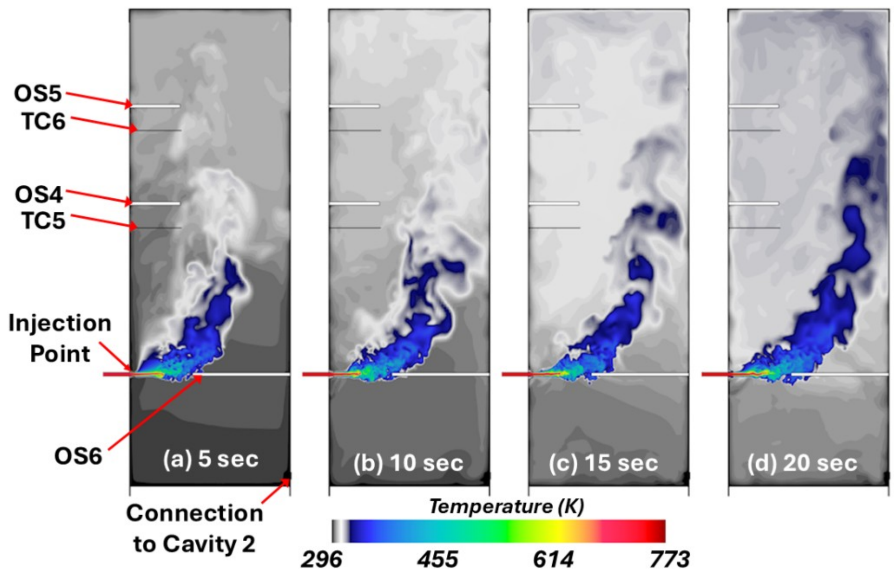


**Fig. 4.14**: Calculated images of the progressive development of the temperature field in cavity 1 at select times during the CFD simulated analysis transient.

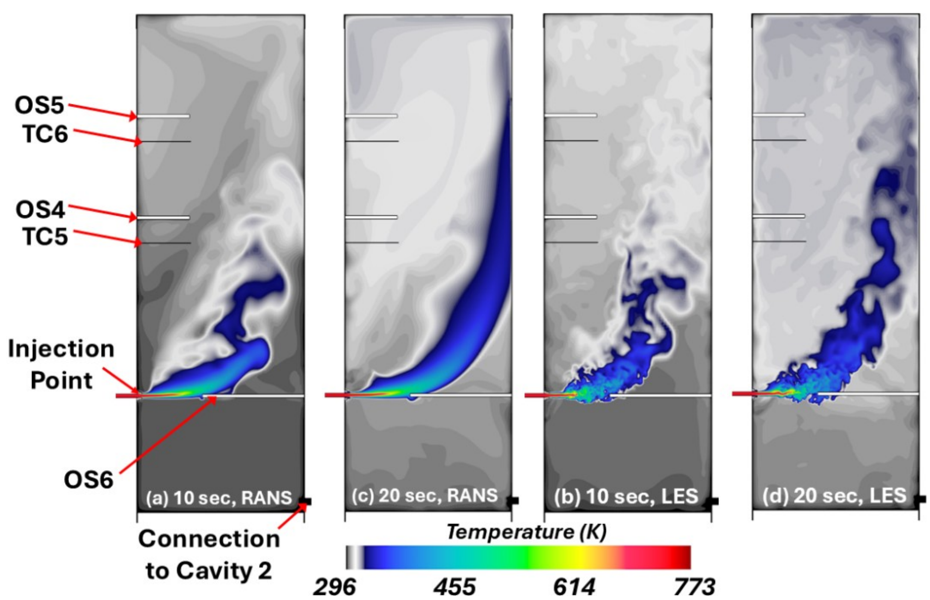


**Fig. 4.15**: Images of the calculated temperature fields in cavity 1 in the CFD analyses with RANS turbulence model at 10 and 20 s during the simulated transient.

The temperature within the cavity increases slightly throughout the simulated transient, rising from an initial volume-average of 296 K to 308 K at the end of the 22 s simulated transient. Results in Figs. 4.14 and 4.15 show that the lower section of the cavity, below the jet injection point, remains relatively cooler due to the lack of turbulent He-air mixing (also evident in Figs. 4.5 and 4.6). The advective behavior in the upper section of the cavity enhances mixing of the hot He with air, as shown in Fig. 4.14, where temperatures increase over time during the transient.

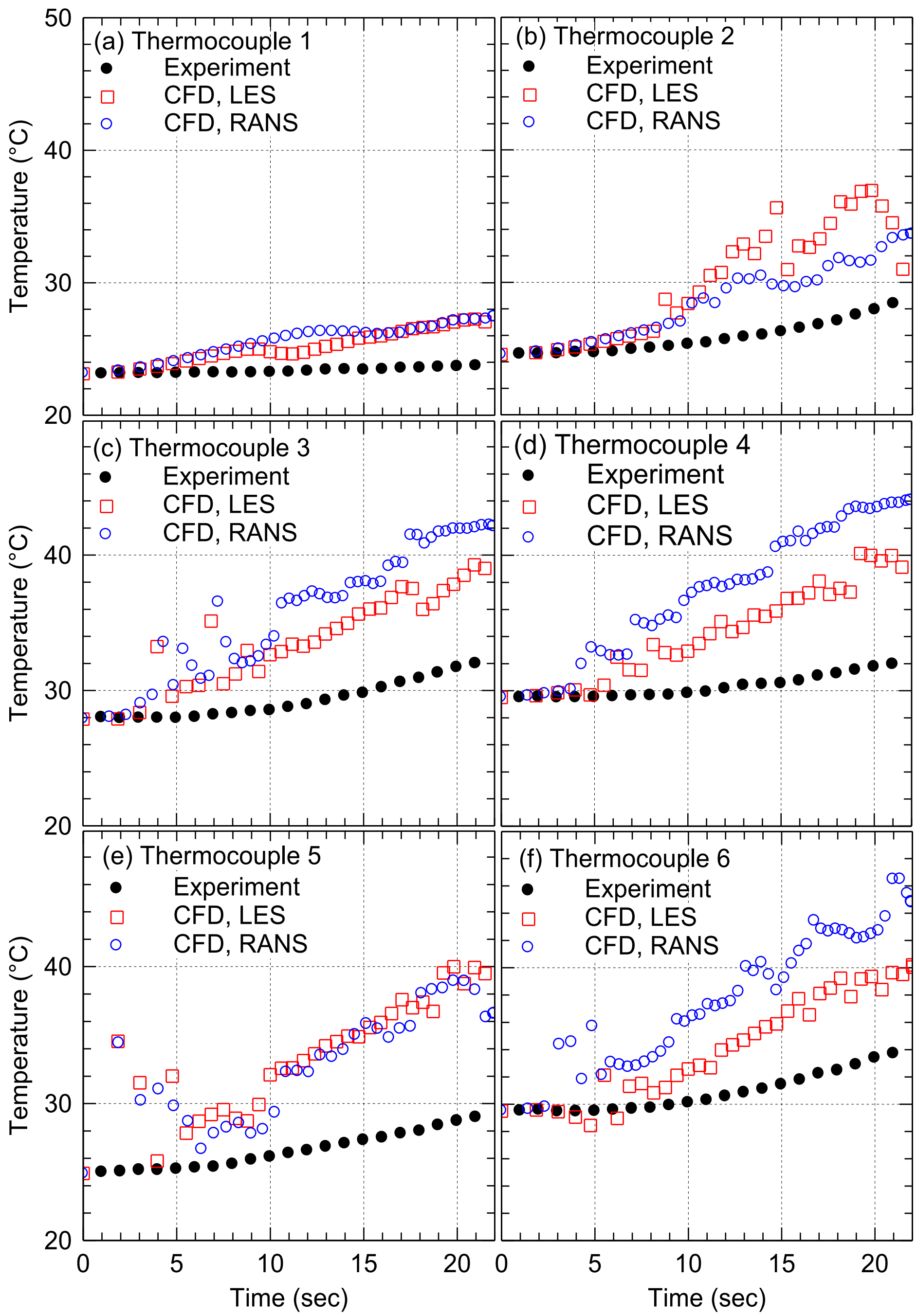


**Fig. 4.16**: Comparisons of calculated temperatures in the present CFD analyses with reported thermocouple measurements by Abubakar et al. [2024].

The CFD analyses, with both the LES and RANS turbulence models, predict similar trends of the oxygen concentrations; however, the LES model yields higher oxygen concentrations due to mixing than the RANS model. In the central recirculation zone of the mixed He-air plume, the RANS model predicts lower temperatures in the center of the recirculation cell than the

LES model. The predicted temperatures in the analysis with the RANS model in the outer region of the recirculation cell near the cavity walls are higher than those with the RANS model (Fig. 4.15). This is corroborated by the temperature measurements at the thermocouple locations.

Fig. 4.16 shows the calculated temperatures at the thermocouple locations near the recirculation zone in cavity 1 (TC3, TC4, TC5, and TC6). All show slightly higher temperatures in the analysis with the RANS model. The CFD simulation analyses with the RANS and LES calculations predict similar temperature increases during the simulated transient, though the results differ slightly from one another. Conversely, the calculated temperatures differ significantly from the reported measurement by Abubakar et al. [2024]. Unlike the pressure and oxygen concentration comparisons, the CFD simulation analyses consistently predict a faster increase in the local temperatures than measured in the experiments. The calculated temperature in Fig. 4.16 exhibits more pronounced oscillations than the reported experimental measurements. The calculated temperatures at the locations of TC3, TC4, TC5, and TC6, located above the hot He injection point into cavity 1, where hot He accumulates due to buoyancy, agree with experimental measurements to within ~7-10 °C (4.16). In contrast, Fig. 4.16a shows that at the TC1 location, below the hot He injection point, the calculated temperature agrees best with the experimental measurements, differing by only 2.5 °C. This smaller difference could be attributed to the limited mixing of the hot He with air in the lower section of the cavity.

### *4.5 Summary*

The CFD analyses investigated the effect of the initial temperature and distribution on the calculated pressure, and the spatial distributions of the oxygen concentration and temperature in the cavity during the 22 s long simulated transient in the experiment [Abubakar et al., 2024]. These simulations are for cavity 1, isolated from cavity 2 by a solenoid valve. The simulation results with Cavity 1 and Cavity 2 connected are presented and discussed in the next chapter.

The calculated pressure during the hot helium injection into cavity 1 agrees with the measurement to within ~10%. The calculated values for the oxygen concentrations at the locations of sensors OS3 and OS4 are in excellent agreement with the reported measurement in the experiment to within ±1.5%, indicating accurate resolution of He-air mixing in cavity 1 in the simulated transient. The temperature predictions, however, reveal a faster rate of increase than reported in the experiment. The calculated temperature at the locations of the thermocouples in the upper section of cavity 1, above the hot He injection point, are 7-10 °C higher than the reported measurements, and only 2.5 °C higher in the lower section of cavity 1.

The CFD simulation analyses with LES and RANS turbulence models predict similar large turbulent structures and recirculation cells above the hot He jet within the cavity; however, the LES model captures more of the small-scale turbulent structures. The analysis with the LES model indicates improved overall mixing of the injected hot He and air in the cavity. The results of the analyses with both turbulence models show similar temperature rise trends, but neither matched the reported experimental measurements [Abubakar et al. 2024]. The measurements indicate that the gas mixture within the cavity did not heat up as quickly as predicted by the CFD simulations, potentially due to heat losses from the cavity walls in the experiments. The present analyses assume the cavity wall outer surface is adiabatic.

The present results have direct implications for the thermal-hydraulic behavior of the reactor cavity in a full-scale HTGR during the reactor cavity pressurization phase of a DLOFC event. The predicted limited mixing below the hot He injection point suggests that the lower section of the cavity remains relatively cool and filled with mostly ambient air. The air in the upper section of the cavity becomes well mixed with time during the simulated hot He injection transient in cavity 1 (or the simulated reactor cavity). Local oxygen concentrations greater than 20 mol% are calculated throughout the 22 s long simulated transient. The concentration is still lower than that of ambient air, but could significantly affect internal core structures during the ingress phase of the accident as the He-air mixture enters the HTGR core. These insights support safety analyses and contribute to more accurate predictions of the consequences of the ingress phase of the accident.

# Chapter 5 – Analyses of Cavity 1 Connected to Cavity 2

Chapter 4 decribed the setup and presented the results of the conducted CFD simulation analyses of injecting hot helium into cavity 1 (representing that of the HTGR), while isolated from cavity 2 (representing that of the steam generator) using a solenoid valve (Fig. 5.1). These analyses are for the first 22 s of the simulated transient (Fig. 5.2). At this time, the pressure in cavity 1 is 7.4 kPa higher than the ambient in cavity 2, which is open to the environment. Additionally, at this time, the connecting value opens connecting cavities 1 and 2 while maintaining the injection of hot helium into cavity 1, under the conditions shown in Figs. 5.2a and 5.2b. This section outlines the methodology for simulating the blowdown of the transient DLOFC accident experiment after the isolation valve connecting cavities 1 and 2 opens.

Fig. 5.1, which depicts the first two cavities of the Reactor Cavity Test Facility (RCTF) at the City College of New York (CCNY), where simulation experiments are conducted [Abubakar et al., 2024, 2025]. This figure shows cavity 1 connected to cavity 2 by a horizontal connecting pipe fitted with an isolation valve (4). Cavity 2 is instrumented with a pressure transducer (5), four oxygen sensors (OS8 – OS11), and three thermocouples (TC7 – TC9) mounted to the cavity walls at differing axial positions. There are two louvered vents located on the cavity wall, opposite the inlet of the connecting pipe. The lower vent (8) remains sealed in the experiments, while the upper vent (7) serves as the outlet to the downstream cavities. The simulated DLOFC transient in this chapter begins at 22 seconds, when cavities 1 and 2 are connected.

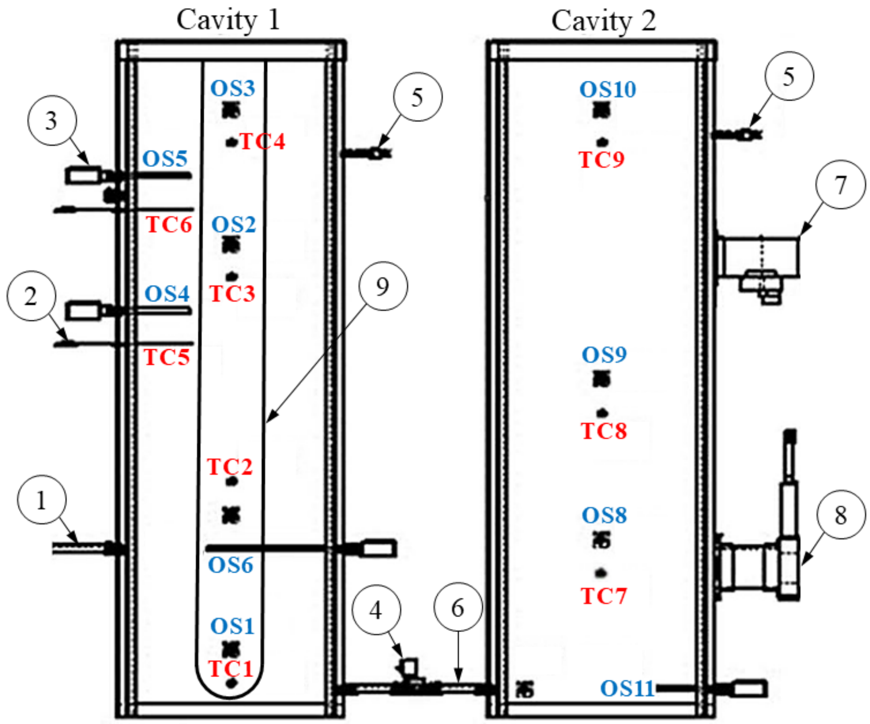


| # | Part |
|---|---|
| 1 | He Injection Pipe |
| 2 | Thermocouple (TC) |
| 3 | Oxygen Sensor (OS) |
| 4 | Isolation Valve |
| 5 | Pressure Transducer |
| 6 | Connecting Pipe |
| 7 | Open Louvered Vent |
| 8 | Closed Louvered Vent |
| 9 | Distributed Temperature Sensor (DTS) |

**Fig. 5.1:** Cavities 1 and 2 Setup and Instrumentation.

### *5.1 Methodology and Approach*

Fig. 5.2a and 5.2b present the flow rate and inlet temperature of the helium gas injected into cavity 1 during the simulated transient when Cavity 1 is isolated and connected to cavity 2. Both cavities are assumed initially to be filled with ambient air. The CFD simulation analyses performed after connecting cavities 1 and 2 use the LES turbulence model.

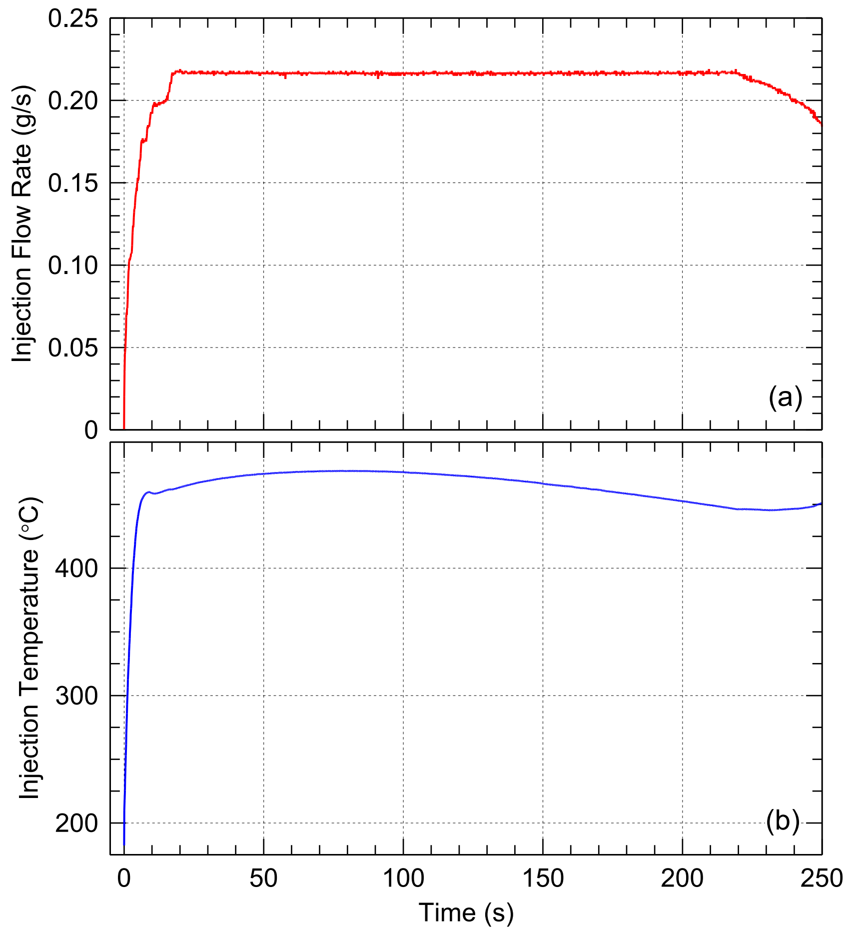


**Fig. 5.2:** Transient Injection Flow Rate and Temperature

### *5.1.1 Numerical Mesh Grid*

The numerical mesh employed for the transient analyses is shown in Fig. 5.3. It is consistent with the meshing strategy adopted in Chapter 4, with the addition of local refinement zones in regions where steep gradients of the calculated parameters are anticipated. The two concentric cylindrical refinement volumes, aligned with the axis of the connecting pipe, resolve the high-velocity jet and associated mixing near the interface into cavity 2. The fine refinement cylinder, which uses the same mesh resolution parameters as the analysis detailed in Chapter 4, is 25 mm in diameter and extends 100 mm into cavity 2. It is surrounded by a medium refinement cylinder with a 100 mm radius and extending 175 mm into cavity 2. Both numerical mesh refinement cylinders are concentric with the centerline of the pipe connecting cavity 1 to cavity 2 (11) in Fig. 5.3.

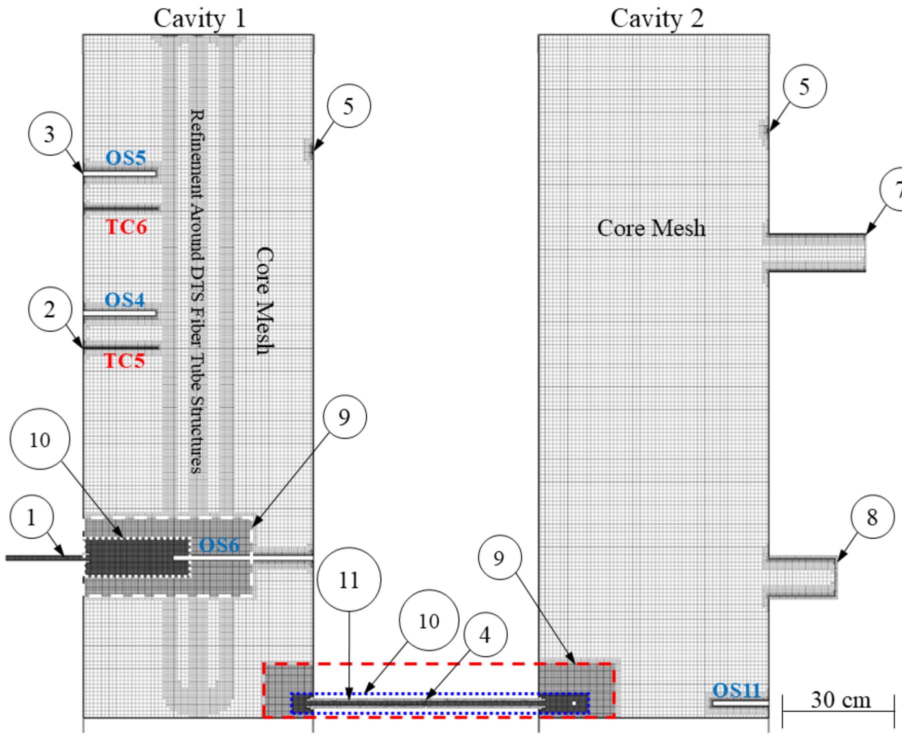


| # | Part |
|---|---|
| 1 | He Injection Pipe |
| 2 | Thermocouple (TC) |
| 3 | Oxygen Sensor (OS) |
| 4 | Isolation Valve Location |
| 5 | Pressure Transducer |
| 6 | Connecting Pipe |
| 7 | Open Louvered Vent |
| 8 | Closed Louvered Vent |
| 9 | Med. Refinement Region |
| 10 | Fine Refinement Region |
| 11 | Connecting Pipe |

**Fig. 5.3:** Employed Numerical Mesh Grid refinements in Cavities 1 and 2.

Table 5.1 provides a breakdown of the total number of computational mesh cells generated along the inside surface of the cavities' walls, the fluid regions of each cavity, and the valve geometry, along with the total cell count. The employed mesh grid provides sufficient resolution to capture the flow and He-air mixing features while remaining computationally tractable for the performed CFD simulation and for transient simulations involving cavities 1 and 2.

**Table 5.1:** Cavity region cell counts.

| Region | Mesh Cell count |
|---|---|
| Cavity 1 Fluid | 4,700,394 |
| Cavity 1 Walls | 1,093,619 |
| Cavity 2 Fluid | 2,581,256 |
| Cavity 2 Walls | 1,082,105 |
| Connecting Valve | 1,909 |
| All Regions | 9,459,283 |

### *5.1.2 Isolation Valve*

The effects of different opening actions for the solenoid value isolating cavities 1 and 2 on computational cost are investigated using the STAR-CCM+ commercial code [Siemens PLM 2023]. Due to the lack of information on the solenoid valve connecting cavities 1 and 2, a gate and a ball valve are considered in the present analyses. The ball valve required an extremely fine numerical mesh to produce numerically stable results. Instantaneously opening the value connecting the two cavities caused numerical instabilities and produced non-physical results. However, a linear translation opening of the valve is numerically stable and does not require excessive mesh refinement in its vicinity. For the gate valve, the employed hexahedral mesh cells are similar in size and match the mesh grid surrounding the valve location. Figure 5.4 presents the mesh grids of the connecting pipe of cavities 1 and 2 and the mounted solenoid valve assembly. Figure 5.4a depicts the valve in the fully closed configuration, and Figure 5.4b depicts the valve in the fully open configuration.

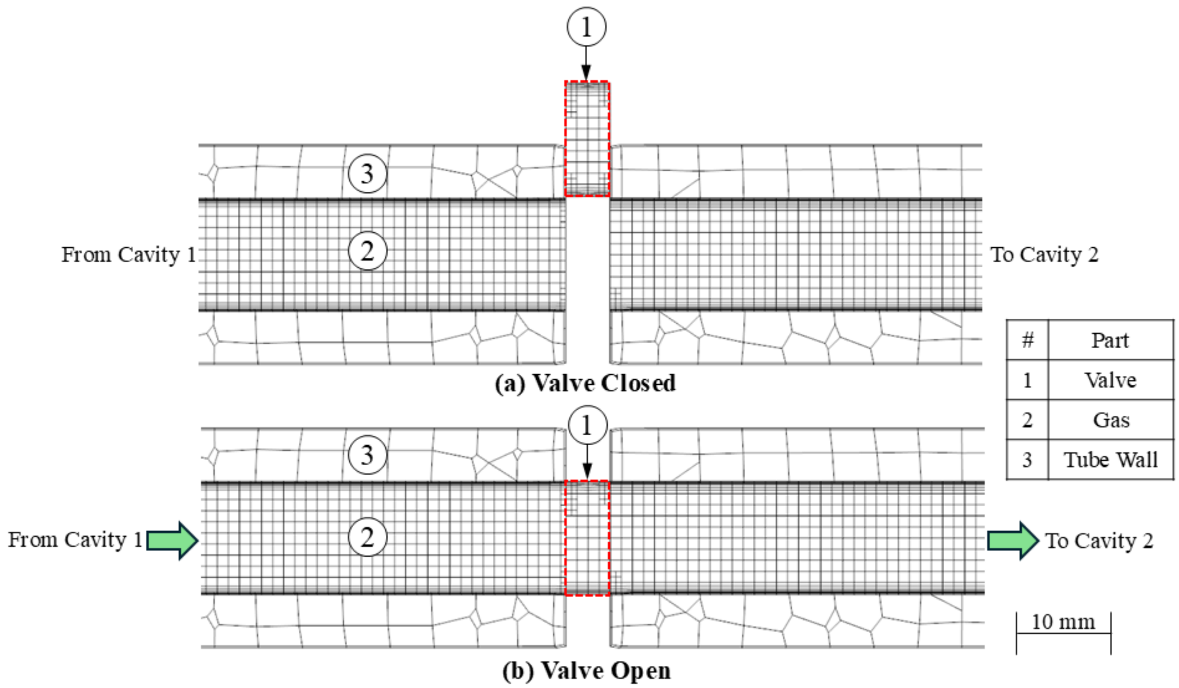


**Fig. 5.4:** Numerical Mesh Grid in the solenoid valve and the pipe connecting Cavities 1 and 2 in the present CFD simulation analyses.

### *5.1.3 Adaptive Time Step*

A CFL number of unity was used in the present CFD simulation analyses to obtain numerically stable results, but the computational cost of the full 250-second transient proved prohibitive, preventing timely results. Consequently, a systematic investigation of the solution's sensitivity is undertaken with CFL limits of 10, 25, 40, and 100, during a simulation period of 22 to 28 seconds, encompassing the valve opening connecting cavities 1 and 2. All simulations used 8 nodes of the Easley cluster at the University of New Mexico Center for Advanced Research Computing, each equipped with 64 Intel Xeon Gold processing units.

The computational performance metrics for each CFL case are summarized in Table 5.2, which reports CPU and wall times, time step sizes, and the mean simulation CFL numbers for each configuration. Because adaptive time step size evolves as the transient progresses, the CPU and wall times, reported for the simulation interval from 24 to 25 seconds, ensure a consistent and representative basis for comparison across all CFL cases. A notable finding is that the mean CFL number remained substantially below the prescribed maximum. This indicates that only a small fraction of the mesh cells in the refined mesh region within the connecting pipe between the two cavities constrain the time step size. This prompts the adaptive time-stepping scheme to adopt very small time steps at the onset of the simulated transient. The pressure differential between the two connecting cavities gradually decreases during the transient, and so do the local velocities. This promotes the adaptive scheme to progressively relax to larger time steps.

**Table 5.2:** Effect of CFL choice on the timestep size in the simulated transient.

| Simulation Max CFL | Simulation Mean CFL | Timestep Size (s) | CPU hrs for 1.0 s simulation | Wall hrs for 1.0 s simulation |
|---|---|---|---|---|
| 10 | 0.00106 | 1.253E-5 to 7.693E-5 | 77731.31 | 79.85 |
| 25 | 0.00404 | 2.859E-5 to 1.756E-4 | 21055.70 | 21.73 |
| 40 | 0.00593 | 4.507E-5 to 2.768E-4 | 15446.65 | 15.44 |
| 100 | 0.01337 | 9.786E-5 to 6.010E-4 | 7871.09 | 8.06 |

### *5.2. Results and Discussion*

This section presents and discusses the results of the CFD simulation analyses when cavity 1 and cavity 2 are connected, which occurs 22s into the simulated transient (Fig. 5.2). The analyses employ the LES turbulence model, and the calculated results include the pressure and the spatial distribution of temperature and oxygen concentration in both cavities. This analysis is for the full 250 s of the conducted DLOFC transient in the experiment [Abubakar et al. 2024]. The obtained images of the flow field in both cavities demonstrate the progress of He-air mixing in the reactor cavity (cavity 1) and the steam generator cavity (cavity 2) during the simulated blowdown phase of the DLOFC accident in HTGRs. The progression of the flow from cavity 1 to cavity 2 and the resulting He-air mixing are insensitive to the time used to fully open the solenoid valve connecting the two cavities. Results are presented in the next subsection.

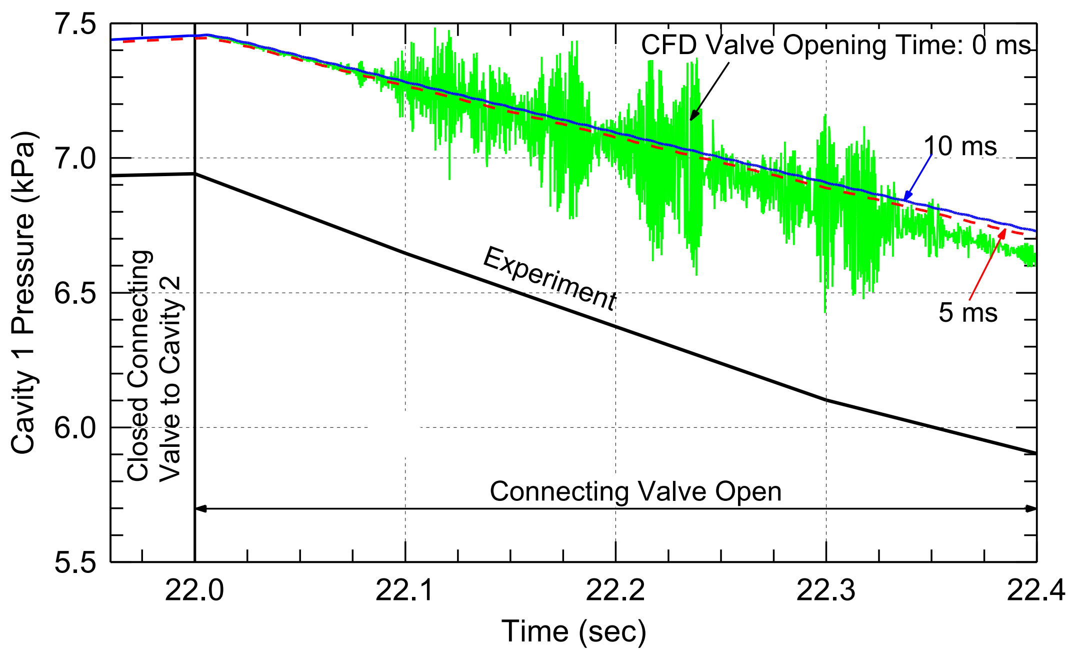


**Fig. 5.5:** Comparison of calculated pressure with reported measurements in the simulated transient after connecting cavity 1 to cavity 2.

### *5.2.1 Effect of the Valve Opening Time*

This subsection investigates the effect of the duration of opening the valve on the pipe connecting cavity 1 and cavity 2 (Fig. 5.2) on the calculated results of the performed CFD simulation analyses. The results are for both instantaneous and gradual opening of the valve for durations of 5 ms and 10 ms (Fig. 5.5). This figure compares the calculated pressure in cavity 1 at the location of the pressure transducer in the experiment (Fig. 5.1). The instantaneous opening of the valve causes pressure oscillations, which are absent in the cases of gradually opening the valve. The time of opening the valve slightly affects the pressure in cavity 1, which increased with increased valve opening duration. Note that the calculated pressure in cavity 1 is consistently higher than the reported measurements in the experiment [Abubakar et al. 2024].

The effect of the oscillations of the calculated pressure in cavity 1 that follows the instantaneous connection of cavity 1 to cavity 2 is further demonstrated by the calculated velocity field in Figure 5.6a. These oscillations, due to numerical instabilities, are entirely absent in Figures 5.6b and 5.6c, which correspond to valve opening durations of 5 ms and 10 ms, respectively. The results of the simulation presented in Fig. 5.5 and in the remainder of this section are from the performed CFD analyses using the LES turbulence model and a CFL number of unity.

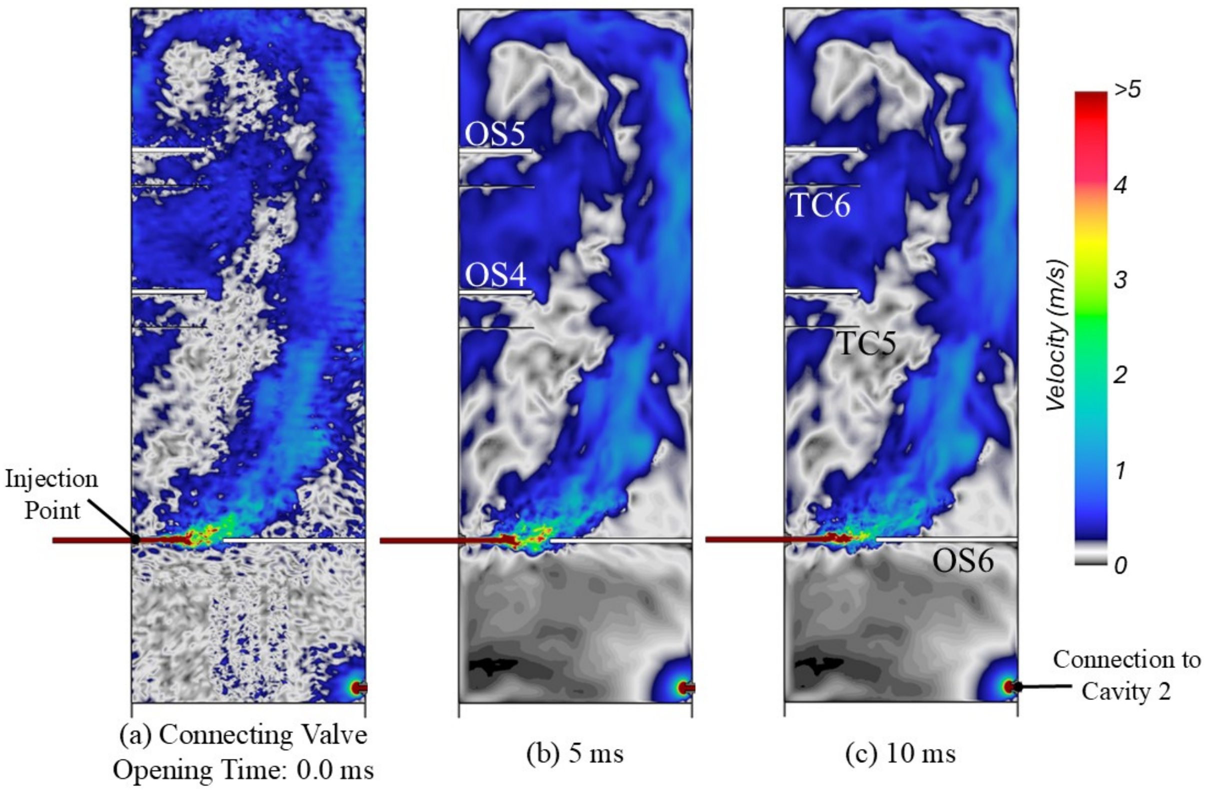


**Fig. 5.6:** The effect of the duration of the valve connecting cavities 1 and 2 of the flow field in cavity 1, 200 ms after opening the valve.

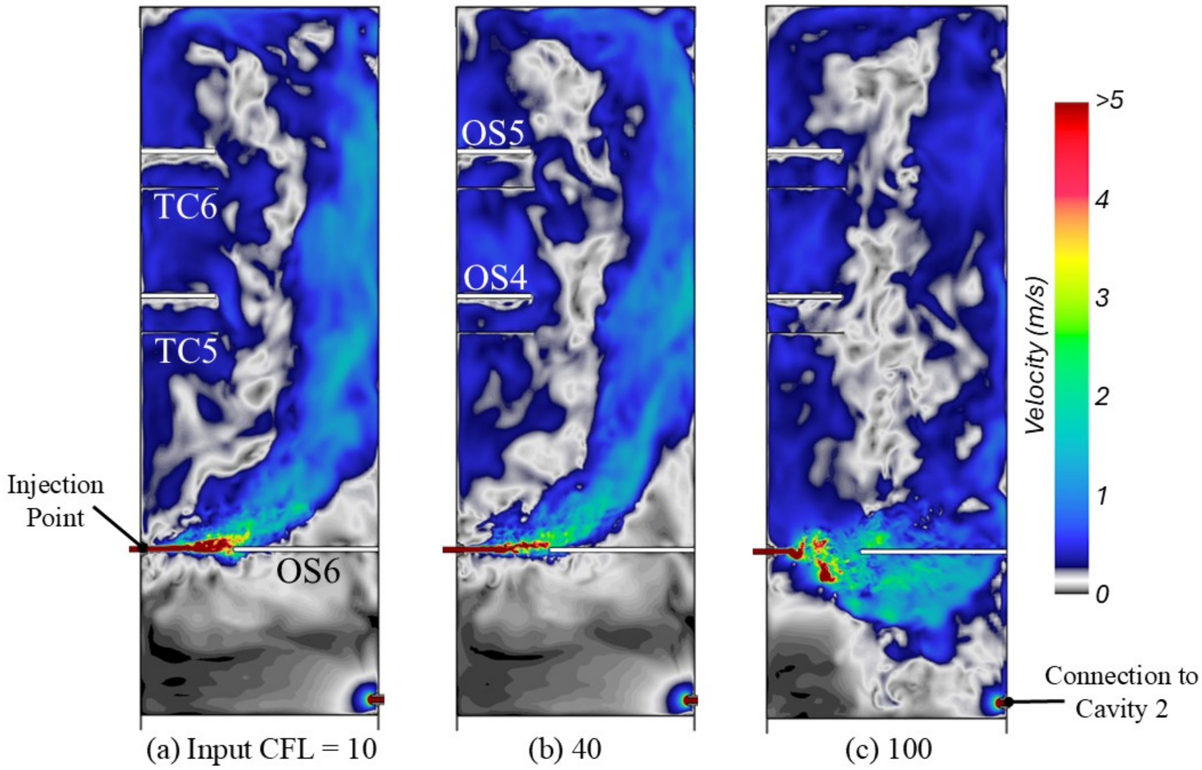


**Fig. 5.7:** Calculated flow fields in cavity 1, 3.0 s after being connected to cavity 2.

### *5.2.2 Time Step Sensitivity*

The CFD results in Figure 5.7 show the calculated flow field in cavity 1 for maximum CFL numbers of 10 (Fig. 5.7a), 40 (Fig. 5.7b), and 100 (Fig. 5.7c) at 25 s into the simulated transient. The flow fields for the cases with CFL limits of 10 and 40 are similar, though not identical. The difference is attributable to the inherently chaotic nature of the resolved turbulent structures in the present CFD analyses with the LES turbulence model. However, the calculated flow field with a CFL limit of 100 case exhibits a substantially different spatial velocity distribution from those with the lower CFL limits, indicating a loss of physical fidelity when using large time step sizes. To balance computational efficiency and solution accuracy, a maximum CFL of 40 is used in the present CFD simulation analyses, as presented in the remainder of this section.

### *5.2.3 Pressure Calculations and Comparison*

Fig. 5.8 compares the calculated pressure in cavity 1 during the entire transient with reported experimental measurements [Abubakar et al., 2024]. Notably, the pressure in cavity 2 remains nearly constant, ~0.05 kPa above ambient. Following the opening of the isolation valve in the pipe connecting cavities 1 and 2, 22 s into the simulated transient, both the calculated and measured pressures in cavity 1 experienced a steep initial drop, followed by a gradual decrease over the remainder of the 250-second simulated transient. The drop in the calculated pressure is initially steeper than measured but remains lower throughout the remainder of the simulated transient.

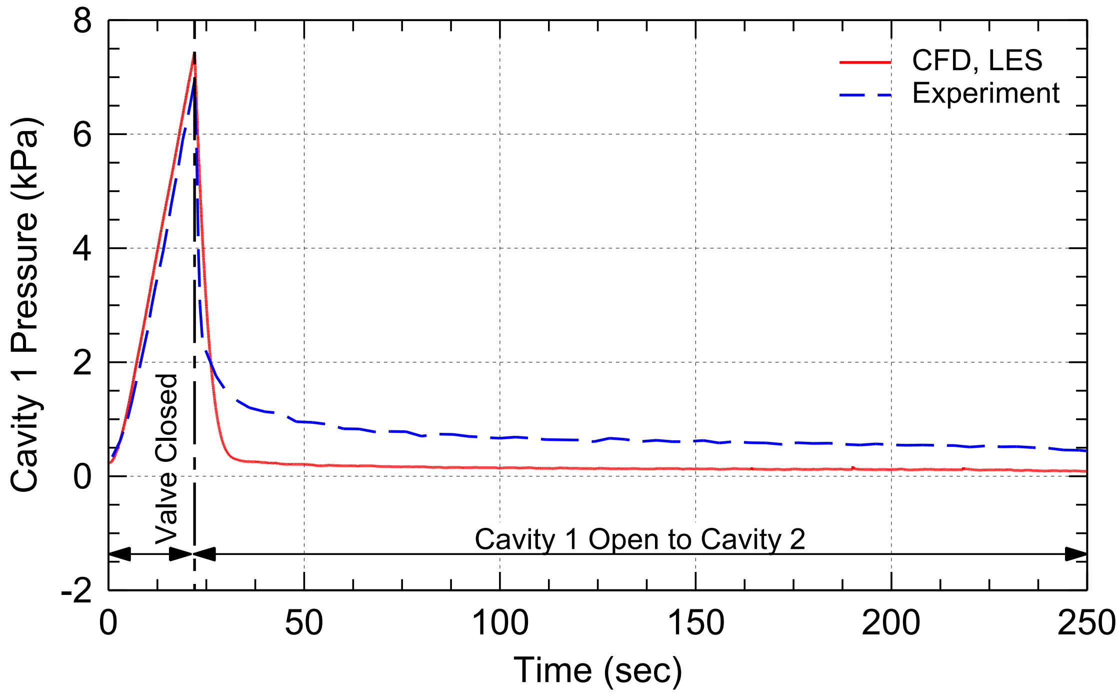


**Fig. 5.8:** Comparison of the calculated pressure in cavity 1 for the present CFD analyses with the LES turbulence model with reported experimental measurements [Abubakar et al. 2024].

### *5.2.4 Flow Field Images*

The images in Figs. 5.9 and 5.10 illustrate the evolution of the flow fields in the connected cavities at 22.1 s, 100 s, 150 s, and 200 s into the simulated transient. Fig. 5.9, which uses a color contour scale ranging from 0 to 50 m/s, shows the velocity features of the injected hot He jet into cavity 1 and of the jet from the connecting pipe into cavity 2. The image in Fig. 5.10 presents the calculated flow field at the same time instances as Fig. 5.9, but with a narrower scale of 0 to 5 m/s to enhance the resolution of low-velocity flow structures within the bulk plumes in the cavities.

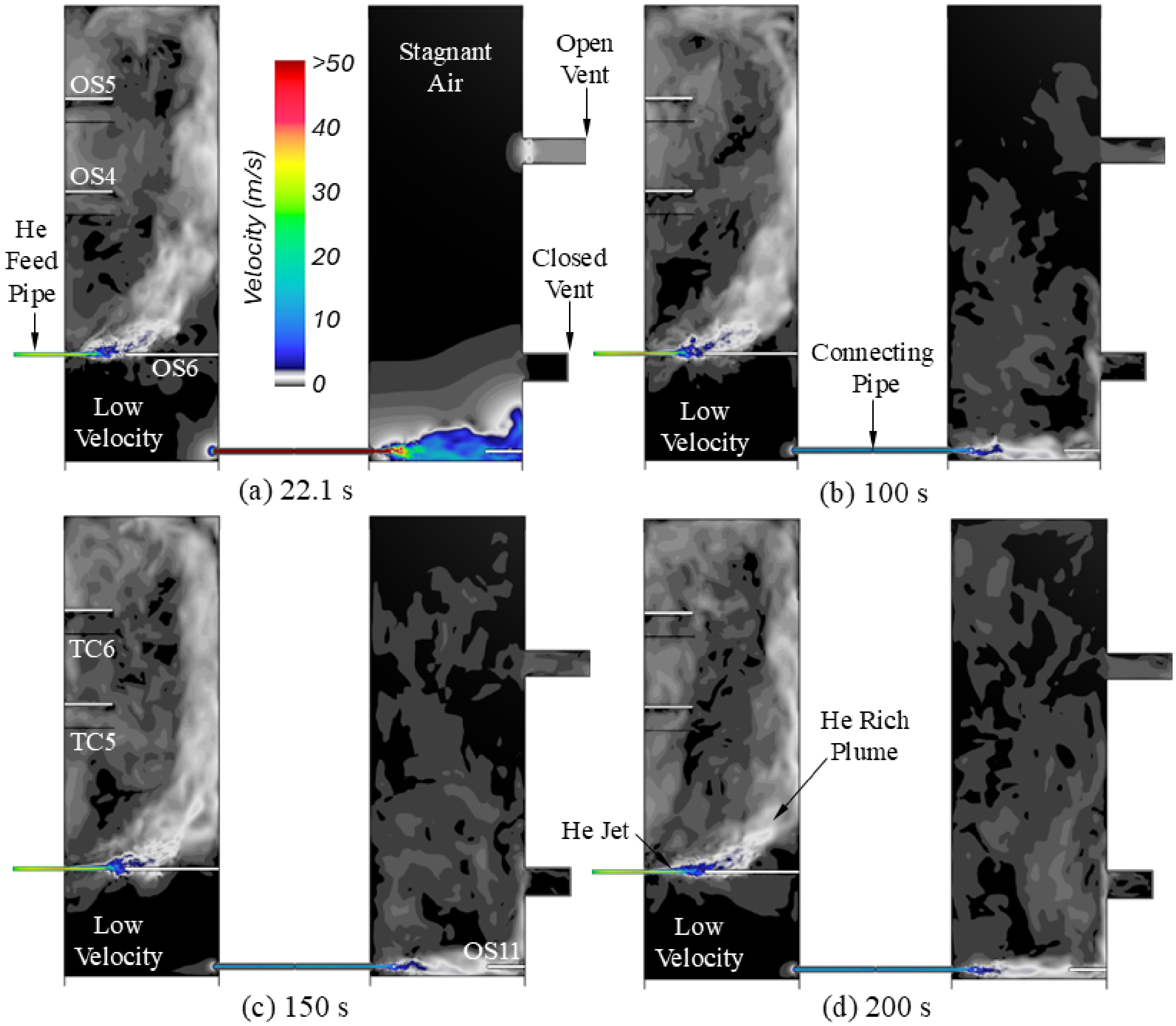


**Fig. 5.9:** Time progression of the calculated flow fields in cavities 1 and 2 at selected times during the simulated transient, with 0 to 50 m/s scale of the color contours.

At 22.1 s (Fig. 5.9a), the morphology of the injected hot He jet into cavity 1 is similar to that observed during the pressurization of cavity 1 before being connected to cavity 2. However, the upward curvature of the He-air mixing plume is reduced with time over the simulated transient (Figs. 5.9a – 5.9c). The injected He jet penetrates progressively deeper into the cavity before curving upward. This may be attributed to the reduced buoyancy of the He-air mixing plume in cavity 1 over time during the simulated transient.

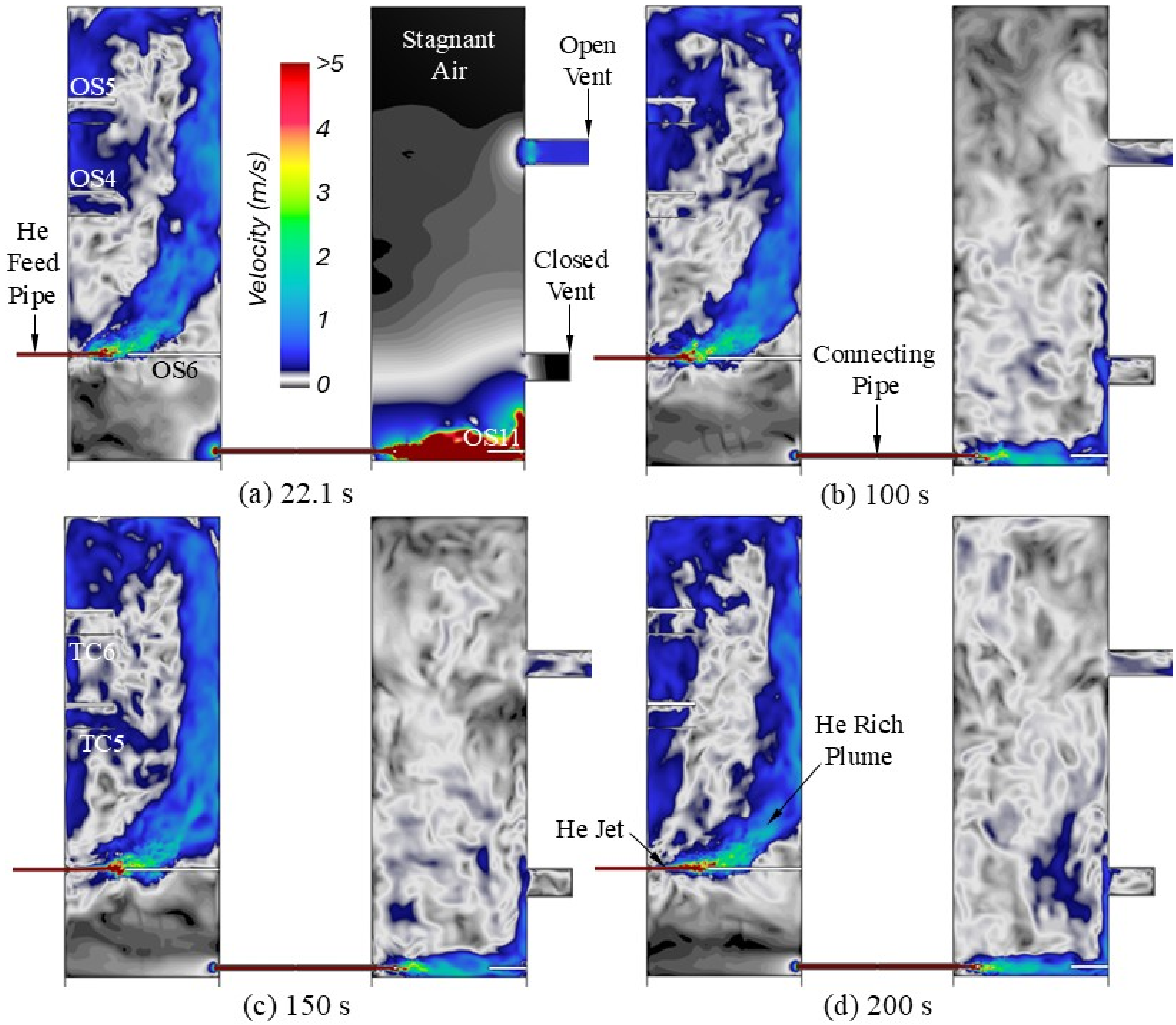


**Fig. 5.10:** Time progression of the calculated flow fields in cavities 1 and 2 at selected times during the simulated transient, with 0 to 5 m/s scale of the color contours.

At 22.1 s into the simulated transient (Fig. 5.10a), the He-air jet entering cavity 2 from the connecting pipe is well-established; however, the flow has not yet propagated to the upper section of cavity 2. Throughout the remainder of the transient, the entering He-air flow into cavity 2 travels horizontally across, impinges on the opposing wall, and deflects upward along the wall's inner surface. This flow pattern in cavity 2 remains consistent throughout the simulated transient. The flow in the cavity's upper section exhibits velocities below 0.02 m/s and contains minor recirculation zones. The flow and He-air mixing in the lower section of cavity 1 remains largely quiescent, with velocities below 0.02 m/s throughout the simulated transient. The sole exception is within a few centimeters before the entrance of the connecting pipe of cavity 1 to cavity 2, where the flow velocity increases due to the area reduction from cavity 1.

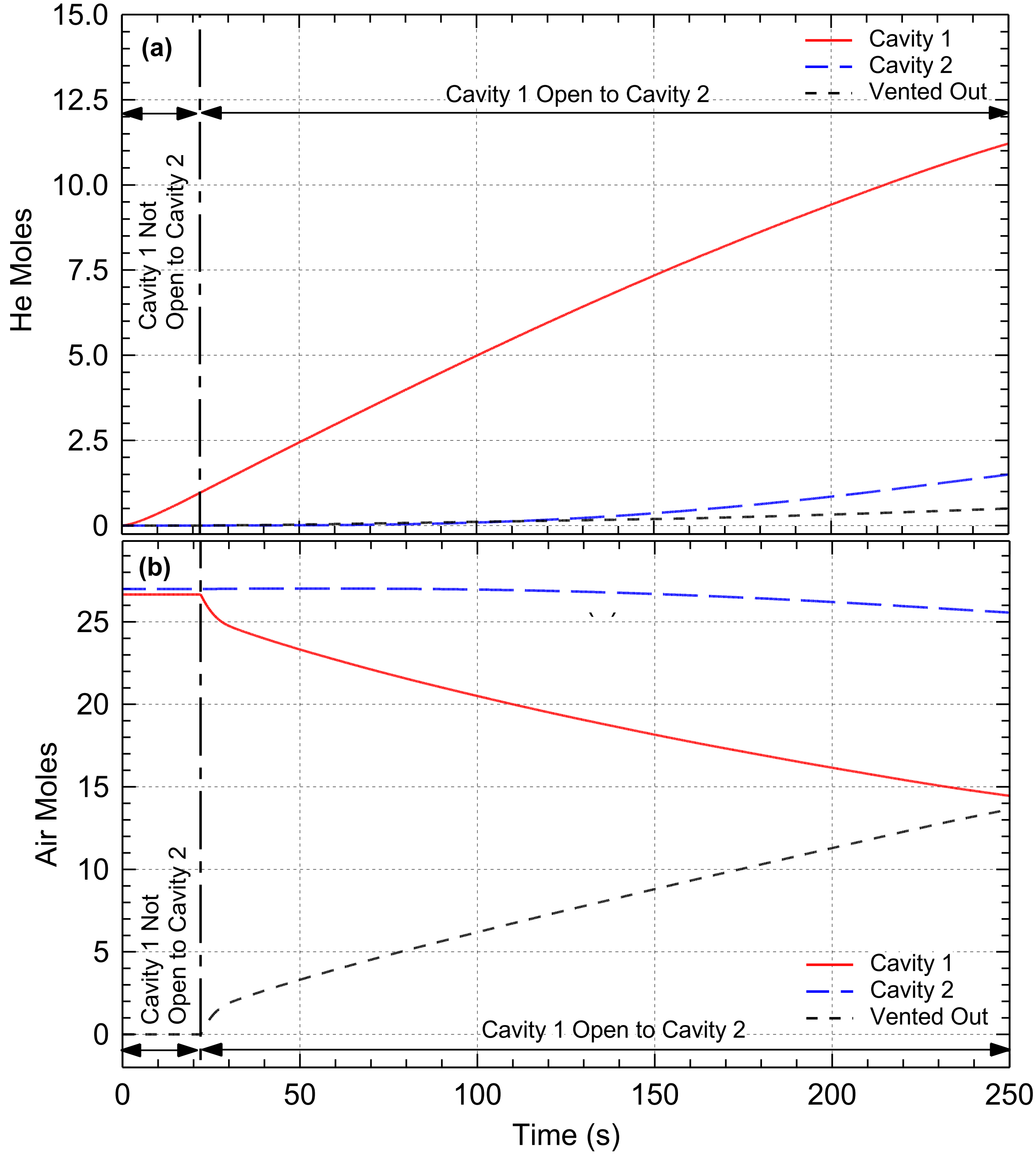


**Fig. 5.11.** The calculated moles of He and air in cavities 1 and 2 during the simulated transient.

### *5.2.5 Cavity Species Composition and Flow Rates*

The evolution of the total moles of each species within cavities 1 and 2, and the total amount of gas ejected from cavity 2 throughout the transient are presented in Fig. 5.11, with Fig. 5.11a and Fig. 5.11b showing the total molar quantities of He and air, respectively. The corresponding species and mixture flow rates at the inlet pipe, connecting pipe, and outlet vent are presented in Fig. 5.12, with molar flow rates shown in Fig. 5.12a, 5.12c, and 5.12e, and mass flow rates shown in Fig. 5.12b, 5.12d, and 5.12f. As shown in Fig. 5.12a, the He flow rate from cavity 1 into cavity 2 increases nearly linearly throughout the simulated transient, consistent with the approximately constant injection rate of the hot He into cavity 1. In contrast, the He inventory in cavity 2 (Fig. 5.11a) remains negligible until approximately 100 seconds into the transient, which is when it begins to rise. This delayed accumulation of He in cavity 2 reflects the time required for sufficient He to accumulate at the bottom of cavity 1 and then be transported into cavity 2.

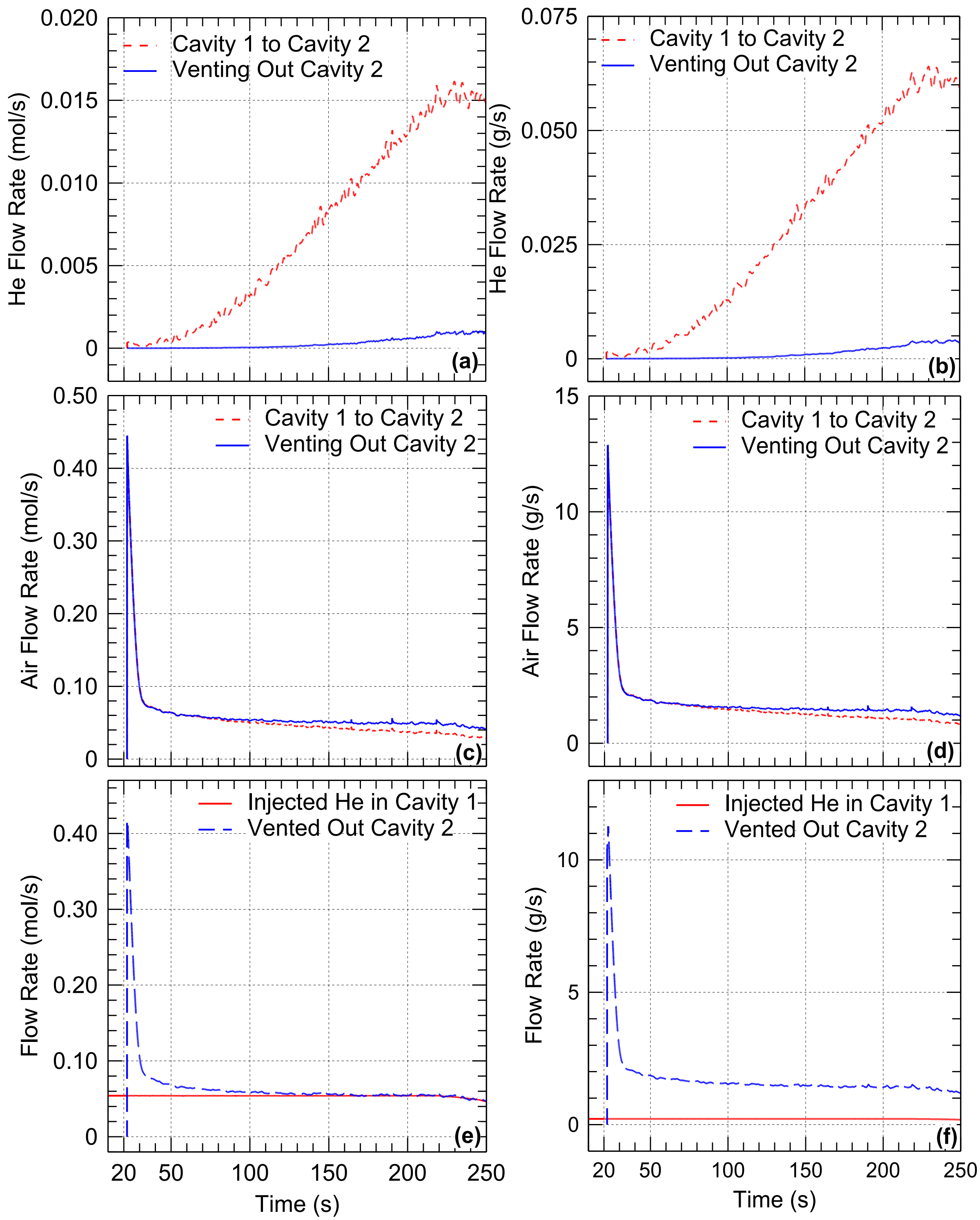


**Fig. 5.12:** Comparisons of the calculated flow rate of He and air in cavities 1 and 2 during the simulated transient, in the CFD analyses with the LES turbulence model.

The results in Fig. 5.11b show that upon connecting cavities 1 and 2, the molar inventory of the air in cavity 1 undergoes a steep decline, then decreases almost linearly throughout the remainder of the transient. The air inventory in cavity 2, by contrast, remains nearly constant until approximately 100 seconds into the transient, which corresponds precisely to the onset of a meaningful He accumulation in cavity 2 (Fig. 5.11a). This suggests the presence of a pocket of air in the lower section of cavity 1, which is partially isolated from the He-rich mixture above. During the time interval between the opening of the isolation valve connecting cavities 1 and 2 to approximately 100 s into the transient, the stagnant air pocket at the bottom of cavity 1 is gradually forced through the connecting pipe into cavity 2, without substantially altering the air inventory in cavity 2 until the He front arrives. From a reactor safety standpoint, if this air inventory enters the reactor vessel, it could prompt high gasification of the nuclear graphite in the HTGR core. Therefore, this scenario is of considerable importance to reactor safety of HTGRs during a DLOFC event.

Figures 5.12a and 5.12b present the calculated molar and mass flow rates of He through the pipe connecting cavities 1 and 2 and the outlet vent of cavity 2. Immediately after opening the isolation valve between cavities 1 and 2, He begins to flow from cavity 1 to cavity 2. The corresponding He flow rate increases progressively with time as its inventory in cavity 1 increases due to the continued injection of hot helium into cavity 1. He flow through the cavity 2 outlet vent remains negligible during the early portion of the simulated transient. However, it increases progressively over time, starting approximately 100 seconds into the simulated transient, consistent with the onset of He accumulation in cavity 2.

The results presented in Figures 5.12c and 5.12d show that immediately after connecting cavities 1 and 2, the air flow rate exiting cavity 2 through the outlet vent is slightly higher than that flowing from cavity 1 into cavity 2 through the connecting pipe. The two rates converge and track each other closely until approximately 100 seconds into the simulated transient. Beyond this time, these flow rates diverge, as the airflow from cavity 1 into cavity 2 through the connecting pipe declines relative to that vented from cavity 2. This is consistent with the progressive depletion of the air inventory in cavity 1.

The calculated flow rates of the He-air mixture entering and exiting cavity 2 are presented in Figs. 5.12e and 5.12f, in molar and mass units, respectively. Both figures show a pronounced initial spike in the flow rate exiting cavity 2 immediately following valve opening, driven by a pressure differential between the two cavities. The hot He injection flow rate into cavity 1 remains essentially constant throughout the remainder of the simulated transient. As the pressure differential between cavities 1 and 2 diminishes, the molar flow rate of the gas mixture exiting cavity 2 (Fig. 5.12e) converges to the molar rate of injected hot He into cavity 1. The mass flow rates presented in Fig. 5.12f do not converge because the molecular weight (and thus density) of the vented gas mixture out of cavity 2 remains substantially higher than that of the injected He into cavity 1. Also, the vented gas from Cavity 2 remains predominantly air throughout the simulated transient.

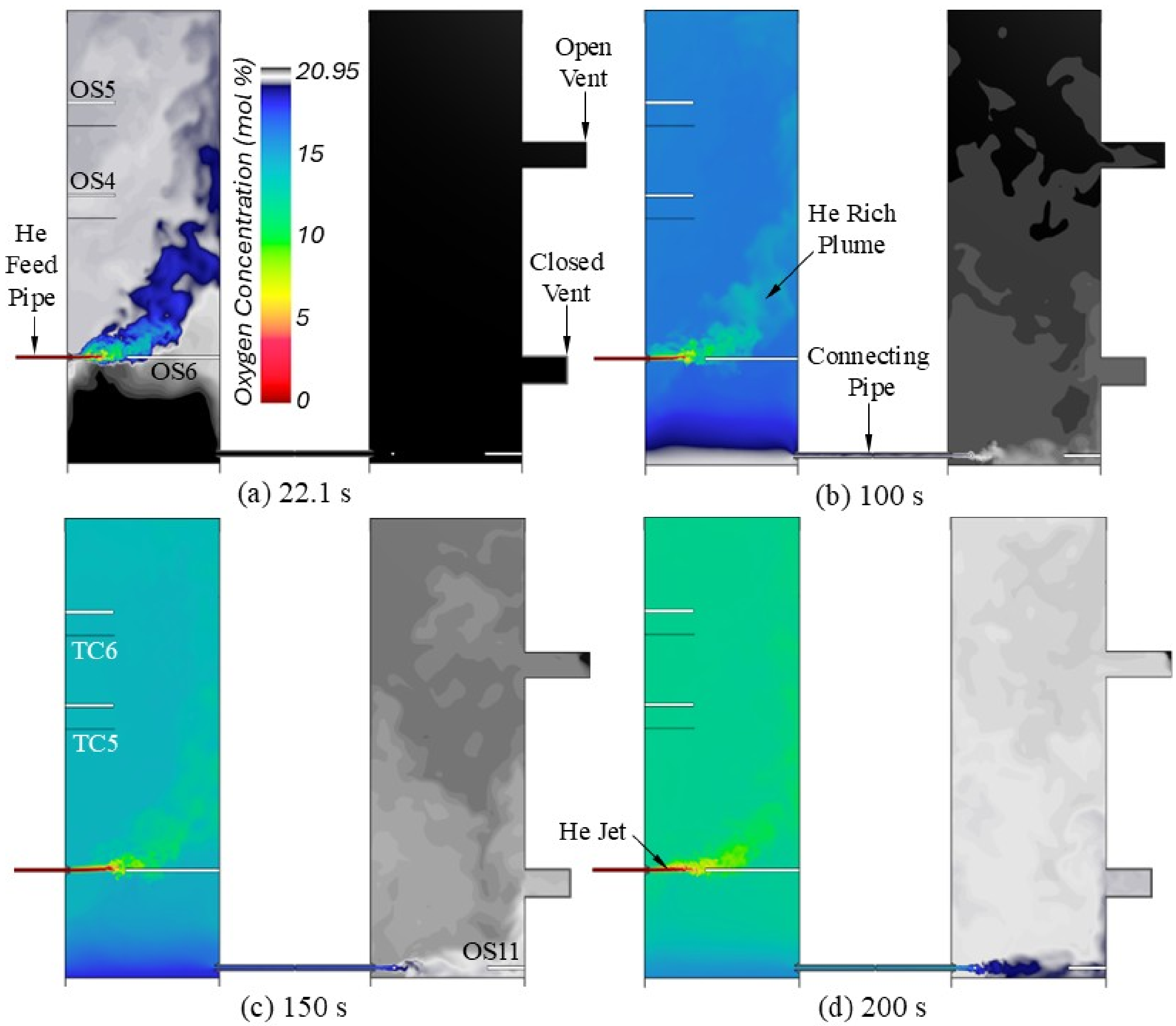


**Fig. 5.13:** Calculated spatial distributions of oxygen concentrations in cavities 1 and 2 at select times during the simulated transient.

### *5.2.6 Spatial Distributions of Oxygen Concentration*

The evolution of the spatial distributions of the oxygen concentration in cavity 1 and 2 is presented in Fig. 5.13 at four instances of time during the simulated transient: 22.1 s (Fig. 5.13a), 100 s (Fig. 5.13b), 150 s (Fig. 5.13c), and 200 s (Fig. 5.13d). At 22.1 s (Fig. 5.13a), there is a well-defined interface between the He-air mixture occupying the upper section of Cavity 1 and the nearly pure air residing in the lower section of this cavity. At this time, Cavity 2 is entirely filled with air. This is consistent with the flow fields presented in Figs. 5.9 and 5.10, which indicate that the gas flow from cavity 1 to cavity 2 has not yet substantially perturbed the gas inventory in cavity 2. At 100 s into the simulated transient (Fig. 5.13b), a ~15 cm tall air-rich mixture in the lower section of cavity 1 is still overlayed by a He-rich mixture. The flow field presented in Fig. 5.9 shows that the flow velocities in this lower section of cavity 1 remain below 0.02 m/s throughout the simulated transient. This suggests that He-air mixing in the lower section of cavity 1 is primarily due to molecular diffusion rather than turbulent diffusion. This distinction is important from a reactor safety perspective because limited mixing of He with air suggests that an oxygen-rich mixture will persist near the lower section of the reactor cavity (or cavity 1).

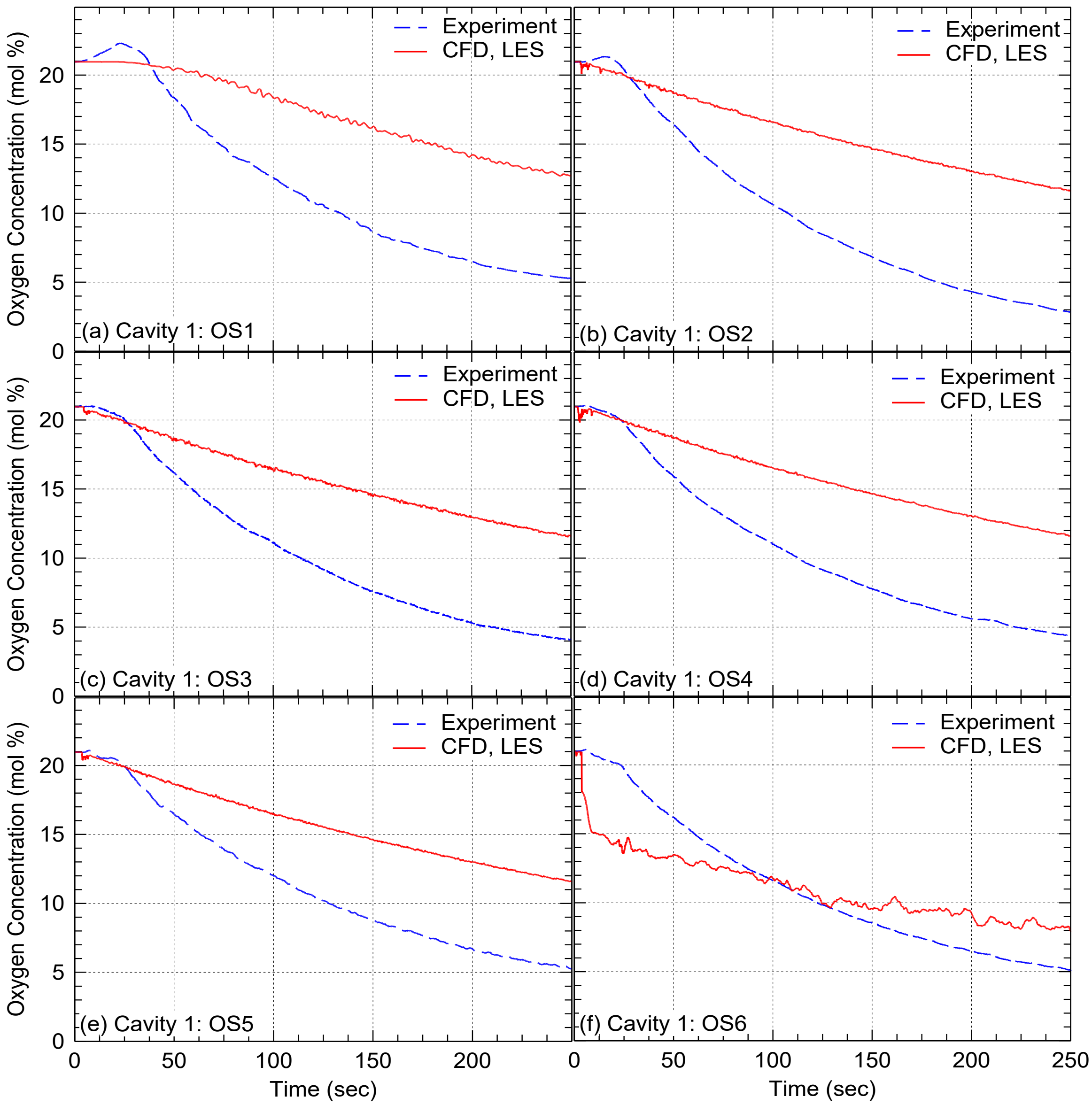


**Fig. 5.14:** Comparison of the calculated oxygen concentration in cavity 1 to the reported measurements during the simulated transient.

As shown in Figs. 5.14 and 5.15, the oxygen concentrations in cavities 1 and 2 decrease progressively with time during the simulated transient. However, the oxygen concentration in cavity 1 decreases faster than that in cavity 2, owing to the continuous injection of hot He into cavity 1 and the delayed transport of He from cavity 1 into cavity 2. The gas entering cavity 2 from cavity 1 is He-enriched relative to the surrounding gas; however, the He disperses rapidly upon entering cavity 2. As a result, the calculated oxygen concentration in cavity 2 decreases slowly with time throughout the simulated transient (Fig. 5.15).

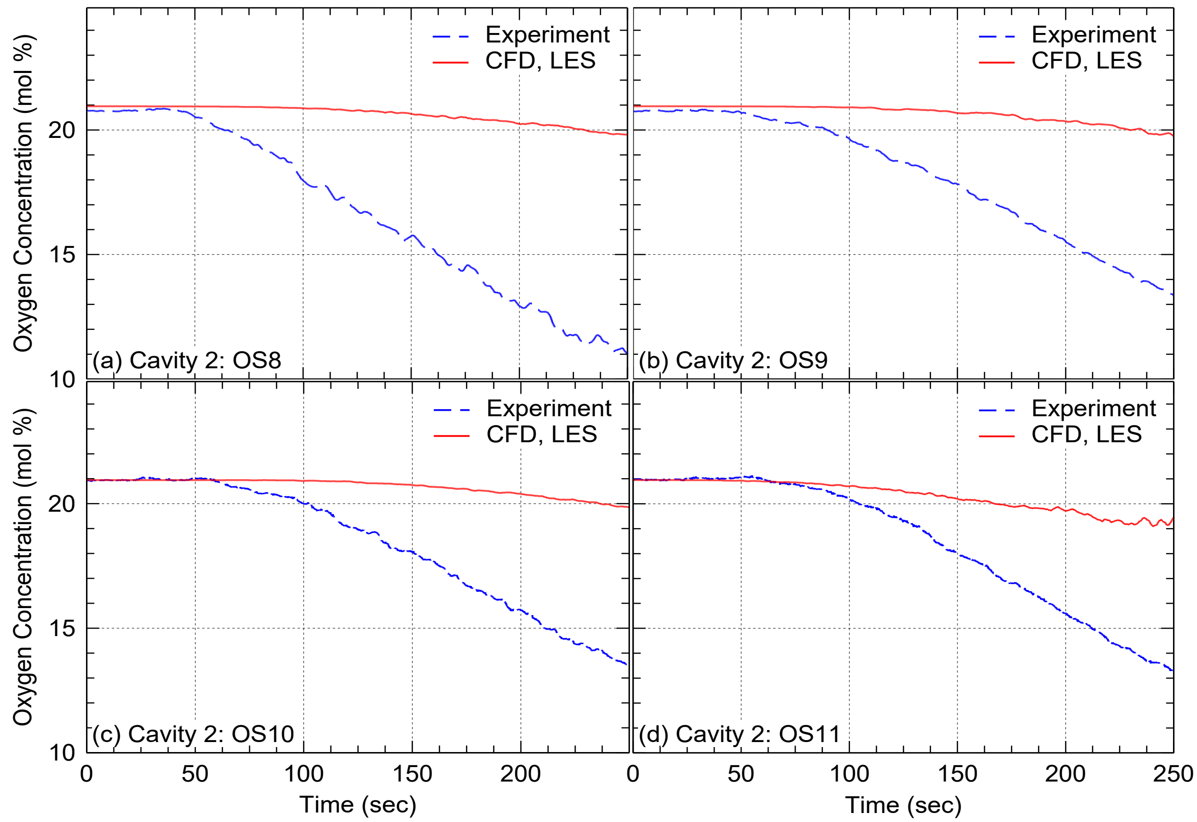


**Fig. 5.15:** Comparison of local oxygen concentration in cavity 2 with reported measurements.

Fig. 5.14 compares the calculated oxygen concentrations in cavity 1 from the present CFD simulation analyses with the reported sensor measurements from the experiment by Abubakar et al. [2024]. At the locations of the oxygen sensors OS1 through OS5 (Figs. 5.14a-e), the calculations predict a nearly linear decrease in oxygen concentration over time during the simulated transient. Nonetheless, the senor's measurements exhibit a more rapid decrease in oxygen concentration over time during the simulated transient. In Fig. 5.14f, the calculated oxygen concentration at the location of OS6 initially drops more steeply than the reported measurements, then decreases more gradually than the experimental data during the remainder of the simulated transient.

The differences between the CFD results and the measured oxygen concentrations at the locations of the oxygen sensors in cavity 1 imply that He-air mixing in the experiment proceeds more rapidly than predicted in the CFD calculations, likely due to multiple contributing factors. The first and most important factor is the questionable accuracy of the oxygen sensors in the experiment in the presence of helium gas. Balderamma Prieto [2022] and Kultgen [2025] documented that the degraded performance of electrochemical oxygen sensors in He-rich environments, such as those encountered during the simulated DLOFC transient, may artificially lower oxygen concentration measurements, as observed in the experimental data. Additionally, Kultgen [2025] contacted the manufacturer of similar zirconia OSs to those used in the experiment. The manufacturer stated that in He-rich environments, zirconia OSs underpredict oxygen concentration. As oxygen concentration increases, the underprediction of oxygen concentration becomes increasingly exaggerated. This likely contributes significantly to the discrepancy between the reported experimental measurements and the CFD simulation analysis. A dedicated treatment of the uncertainties in the experiment OS measurements is provided in Appendix B.

In the present CFD simulation analyses, the solution may not have fully resolved the turbulent diffusivity of the He-air mixture under the prevailing low-velocity flow conditions. In addition, the expressions used to compute species diffusion coefficients in multi-component gas systems may underpredict the effective species mixing rates. Furthermore, the assumed initial temperature and gas composition at the onset of the simulated transient may not precisely reflect the initial conditions in the experiment, due to the lack of reported uncertainties of the experimental measurements.

The results in Fig. 5.15 show that the experimentally measured oxygen concentrations at all sensor locations in cavity 2 decrease considerably and more rapidly than the calculated values in the present CFD simulation analyses. These results again indicate that the calculated He-air mixing in cavity 1 is less regressive than measured in the experiment. Nonetheless, there is a reasonable agreement between the CFD analysis results and the reported experimental measurements in cavity 2 during the first 50 seconds of the transient. Such an agreement suggests that the CFD simulation analyses accurately predict He-air transport and mixing with acceptable fidelity.

### *5.2.7 Temperature Calculations and Comparison*

The calculated spatial distributions of temperatures in cavities 1 and 2 at different times during the simulated transient are presented in Fig. 5.16a (22.1 s), Fig. 5.16b (100 s), Fig. 5.16c (150 s), and Fig. 5.16d (200 s). The temperature in cavity 1 rises gradually during the simulated transient, while cavity 2 remains near 20°C, indicating a limited He inventory and limited mixing with air. The injected hot helium jet into cavity 1, the associated rising plume, and the large counterclockwise recirculation are similar to those indicated in the flow field images presented in Figs. 5.9 and 5.10, and the oxygen concentration spatial distribution shown in Fig. 5.13. At 150 s of the simulated transient (Fig. 5.16c), the rising He-air plume corresponds to the time when the temperature of the injected hot He into cavity 1 is at its highest.

The results in Fig. 5.17 compare the calculated temperatures at the thermocouple locations in cavity 1 with the reported experimental measurements [Abubakar et al., 2024]. Note that during the simulated transient, the calculated temperatures are noticeably higher than measurements at all sensor locations. These temperature decreases occur upon opening the isolation valve and connecting cavities 1 and 2. These temperatures are in better agreement with the experimental data.

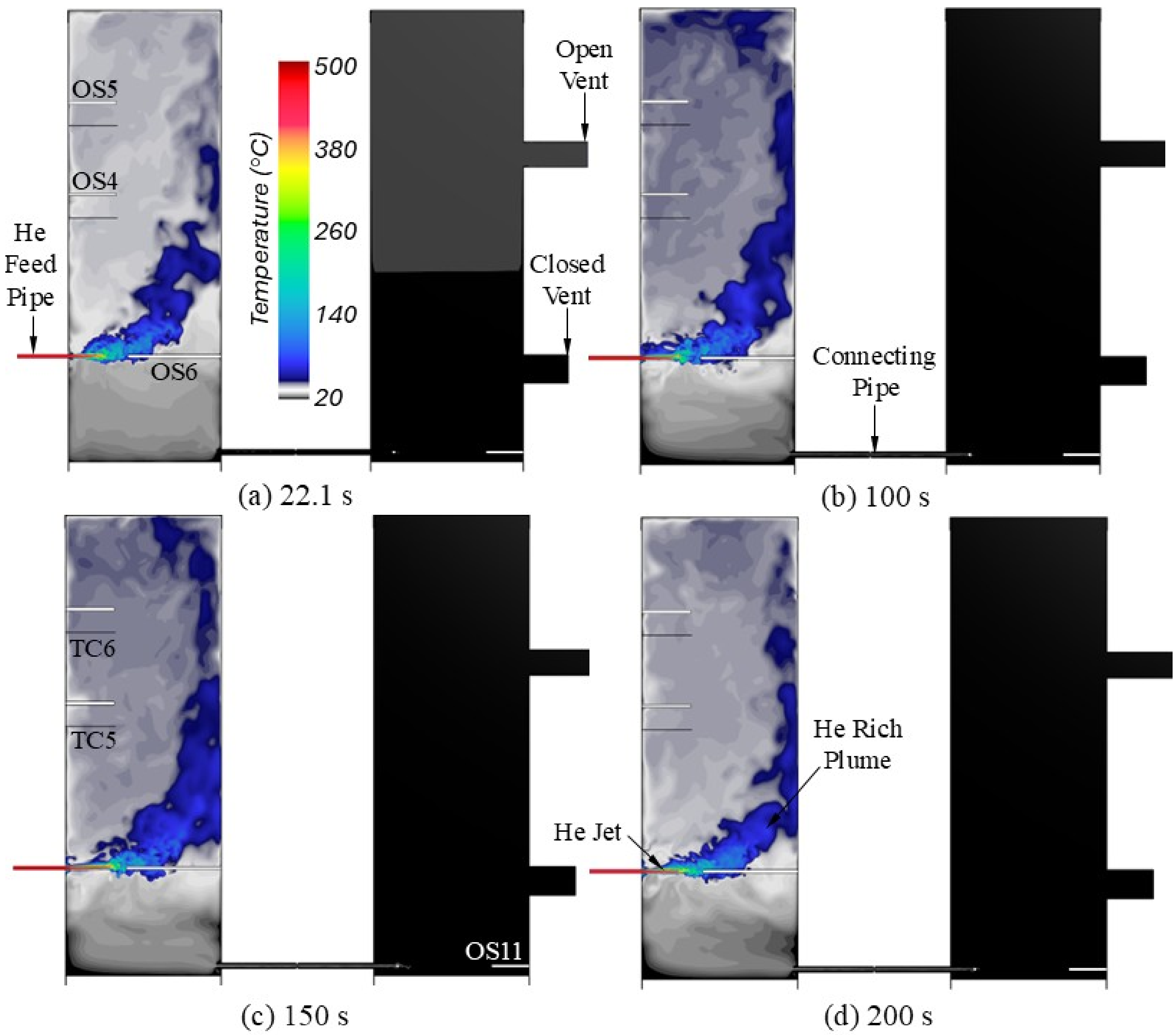


**Fig. 5.16:** Comparisons of the calculated temperature fields in Cavity 1 at select times during the simulated transient, using 296 to 773 K scale color contours.

The results in Fig. 5.17 show that the trend of the calculated temperatures closely matches that of the experimental measurements, with a slight time delay. This behavior is consistent with the temperature of the injected He in cavity 1, which rises rapidly to approximately 480°C at 85 seconds into the simulated transient, then decreases to approximately 440°C by the end of the transient. It is further noted that the He injection temperatures used in the CFD analyses are those measured by the TC downstream of the injection point and are likely higher than the actual injection temperatures due to the TC's distance from the injection point (Appendix A). In addition, these temperature measurements do not account for the fin effect along the thermocouple sheath, which would be expected to artificially lower the recorded temperature below the true value. These effects would likely explain the lower calculated temperatures at the end of the simulated transient compared to the experimental measurements. Another factor that would contribute to decreasing the measured temperatures in the experiments is energy storage and heat losses at the outer surface to the surroundings, which were not measured in the experiments and were only partially accounted for in the CFD simulation analyses.

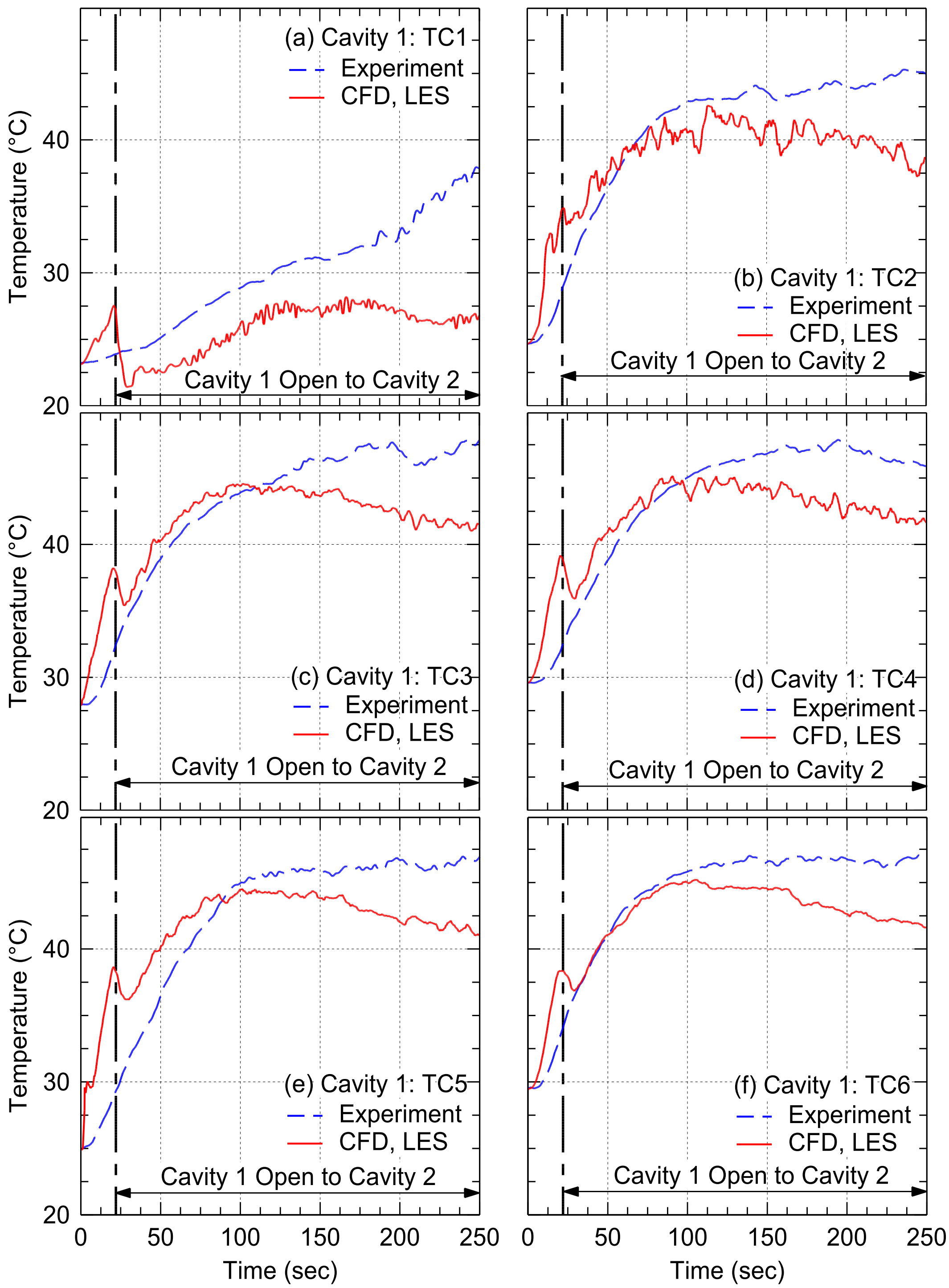


**Fig. 5.17:** Comparison of calculated temperatures in cavity 1 during the simulated transient with the reported measurements in the experiment [Abubakar et al. 2024].

The results in Fig. 5.17a show that following the valve opening connecting cavities 1 and 2, the calculated temperature at the TC1 location in cavity 1 falls below the corresponding experimental measurement and remains lower for the remainder of the simulated transient. The temperature comparison with reported measurements for cavity 2 thermocouples is presented in Fig. 5.18. The calculated temperatures compare favorably with the experimental measurements, with an error of approximately 1.5°C. This level of agreement provides confidence in the fidelity of the temperature predictions in cavity 2, where the flow field is less influenced by the complexities of the hot He injection and mixing in cavity 1, and the associated species stratification.

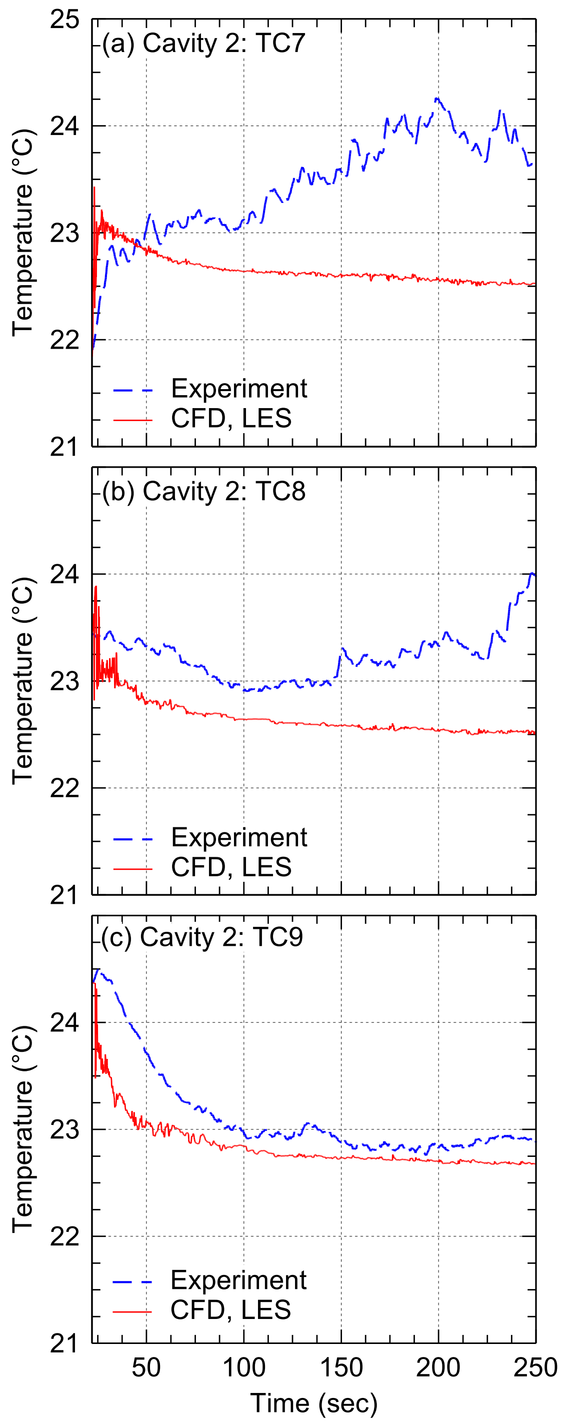


**Fig. 5.18:** Comparison of the calculated local temperatures in cavity 2 with reported measurements in the experiment by Abubakar et al. [2024].

Fig. 5.19 compares the temperature measurements in cavity 1 by the thermocouples and the DTS fiber probe near the hot He injection point with the calculated temperatures from the present CFD analyses at various axial positions. Note that TC measurements do not exactly coincide with those measured by the DTS fiber at the various axial positions in cavity 1 during to the simulated transient. The provided comparisons are at 1 minute (Fig. 5.19a), 2 minutes (Fig. 5.19b), and 4 minutes (Fig. 5.19c) into the simulated transient. The calculated axial location of the peak temperature matches well with that recorded by the DTS fiber probe. At 1 and 4 minutes into the simulated transient, the calculated peak temperature exceeds the experimental DTS probe measurement, while at 2 minutes, the calculated temperature falls slightly below the DTS measurement.

The axial temperature gradient below the injection point in cavity 1, as shown in Fig. 5.19, with decreasing temperature toward the cavity base, is well reproduced by the calculations. The best agreement of the calculated temperature and the experimental data in cavity 1 above the He injection point is best at 4 minutes into the simulated transient (Fig. 5.19c). The calculated temperatures fall between the thermocouple and DTS probe measurements. The localized perturbations in the calculated temperatures at certain axial positions do not appear in the DTS measurements. The latter is due to the spatial averaging inherent in the DTS measurement technique, as well as axial conduction along the DTS metal sheath, both of which tend to smooth out fine-scale temperature variations that the computational model resolves with higher spatial fidelity.

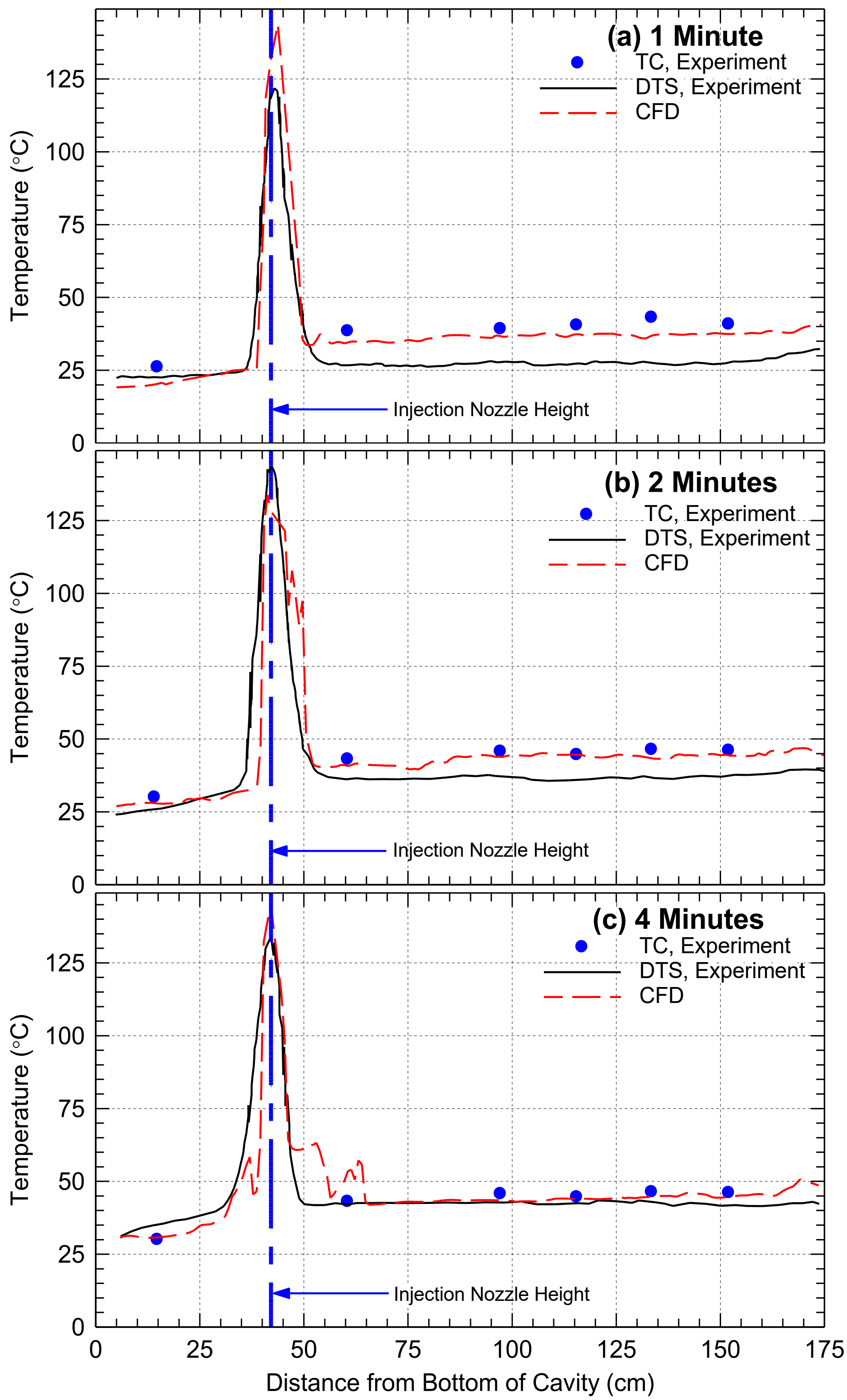


**Fig. 5.19:** Comparison of the calculated temperature in cavity 1 with the reported DTS temperature measurements [Abubakar et al. 2024].

### *5.3 Summary*

This chapter presented CFD simulation analyses of the DLOFC transient in the RCTF following the connection of cavity 1 to cavity 2 at 22 seconds into the simulated transient. Using the LES turbulence model with a maximum CFL of 40, the analyses captured the evolution of pressure, flow fields, species composition, and temperature in both cavities over the full 250-second transient. The progression of He-air mixing was found to be insensitive to the duration of valve opening, provided the valve opened gradually rather than instantaneously. Following valve opening, the pressure in cavity 1 underwent a steep initial drop, followed by a gradual decrease, consistent with the trend of the experimental measurements, though the calculated pressure remained lower than the measured pressure throughout the remainder of the transient.

The spatial distributions of oxygen concentration and temperature revealed key flow features of relevance to HTGR safety. A persistent air-rich pocket in the lower section of cavity 1 poses a potential concern for graphite gasification within the reactor cavity should this air inventory enter the reactor vessel during a DLOFC event. The CFD analyses predicted a nearly linear decrease in oxygen concentration over time at most sensor locations in cavity 1, whereas the experimental measurements exhibited a more rapid decline, likely attributable in part to known inaccuracies of electrochemical oxygen sensors operating in helium-rich environments. DTS calculations in cavity 1 agreed well with experimental measurements, with the positions of highest temperature corresponding to the hot injection jet agreeing particularly well. Agreement between CFD and experiment was more favorable in cavity 2 during the first 50 seconds of the transient, and temperature predictions in cavity 2 agreed with measurements to within approximately 1.5°C throughout the simulated transient, providing confidence in the overall thermal fidelity of the simulation.

# Chapter 6 – Summary and Conclusions

This work presents the results of detailed Computational Fluid Dynamics (CFD) simulation analyses of helium (He) and air mixing in scaled reactor and steam generator containment cavities (cavity 1 and cavity 2) during the blowdown phase of a simulated Depressurized Loss of Forced Cooling (DLOFC) accident in a High Temperature Gas-cooled Reactor (HTGR). The performed simulations using the commercial STAR-CCM+ CFD code and the results of flow mixing, pressure in cavity 1 (reactor cavity), and the spatial distributions of velocity, temperature, and oxygen concentrations are compared to the reported experimental measurements recorded in the Reactor Cavity Test Facility (RCTF) at the City College of New York (CCNY). The two sequential phases of the DLOFC transient analyzed are the pressurization of the reactor cavity (cavity 1) during the initial 22 seconds of the simulated blowdown phase, and the subsequent depressurization of cavity 1 into the connected steam generator cavity (cavity 2), lasting a total of 250 seconds. The depressurization period begins at 22 seconds, when the pressure difference between cavity 1 and cavity 2 reaches 6.9 kPa in the experiment. The opening of a solenoid isolation valve connecting the two cavities triggers at this time.

Determining the mixing behavior of the He gas with air present in the reactor and steam generator cavities has safety implications during the following phase of He-air ingress into the reactor core. This includes oxidation and loss of mechanical strength of the structural graphite components, radionuclide remobilization, the release of radioactive $^{14}C$ nuclides, and potential generation of flammable carbon monoxide. The composition of the gas mixture entering the reactor core during the ingress phase is directly governed by the mixing and stratification dynamics occurring in the containment cavities during the preceding blowdown phase. The objective of the present work is to quantify the extent of the He-air mixing in the reactor and steam generator cavities during the blowdown phase of the accident with sufficient fidelity. This is accomplished through CFD simulation analyses performed in this work, using both the RANS and LES turbulence models. The calculated results include the pressure and spatial distributions of velocities, temperatures, and oxygen concentrations, as well as analyses of the He-air mixing features that occur in both cavities during the conducted transient.

The cavity 1 pressurization analyses are performed for the initial 22 seconds of the simulated blowdown transient for a total of 250 seconds, with hot He injected into the initially air-filled reactor cavity. Four CFD cases are simulated, with cavity 1 isolated from cavity 2 by a solenoid isolation valve. The analyses used the cavity 1 recorded temperature values and spatial distribution from the experiment, and varied the He injection mass flow rate commensurate with the recorded values from the experiment. Accounting for the thermal energy lost to the walls of cavity 1 produces the closest agreement with experimental pressure measurements. Results of using the Large Eddy Simulation (LES) turbulence model with the Wall-Adapting Local Eddy-viscosity (WALE) subgrid-scale model and the Shear Stress Transport (SST) k-ω RANS turbulence model are compared. Both models predict similar large-scale flow features, including a dominant recirculation cell driven by the buoyant helium injection jet, though the LES model resolves substantially more small-scale turbulent structures, producing more vigorous near-field flow mixing.

Calculated oxygen concentrations at the sensor location in cavity 1 are in good agreement with experimental data to within ±1.5%. The predicted temperatures in the upper section of cavity 1, above the hot He injection point, exceed the reported experimental measurements by approximately 7-10°C. This difference may be attributed to unresolved heat loss pathways in the experimental facility and to uncertainty in the He injection temperature into cavity 1 (Appendix A). The results predicted the formation of a He-rich plume in the upper section cavity 1, with a near-pure air zone stratified in the lower section of the cavity throughout the 22 s long pressurization period. The predicted oxygen concentrations in cavity 1 during the 22 s long pressurization phase remain above 20 mol%.

The present CFD simulation successfully modeled the isolation valve mounted on the pipe connecting cavity 1 to cavity 2 as a linearly translating gate valve that smoothly opens completely over a 5 ms or 10 ms period. Instantaneously opening this valve produced numerical instabilities. Using a maximum CFL limit of 40 for variable time step size in the full 250-second simulated transient effectively reduces computational cost without compromising the accuracy of the results or the solution resolution.

The calculated low velocity (below 0.02 m/s) in the lower section of cavity 1 demonstrates that flow in this location is largely quiescent throughout the transient, and as such, the gas mixture here remains mostly air. The calculated oxygen concentrations in cavity 1 consistently underpredict the mixing rate compared to the reported experimental measurements. This is attributed to limitations in the turbulence models for quiescent flow, uncertainty in the transport properties of binary gas mixtures, and oxygen sensor measurements (Appendix B). In cavity 2, the calculated oxygen concentrations also underpredict the reported experimental measurements, though reasonable agreement occurs during the first 30 seconds following the valve opening. Temperature predictions in cavity 2 agree with experimental measurements to within ~1.5°C throughout the simulated transient. Additionally, the calculated axial temperature profiles in cavity 1 are in good agreement with the measurements by the Distributed Temperature Sensor (DTS) fiber probe. The predicted peak temperature location in cavity 1 closely matches that recorded by the DTS probe. These comparisons collectively provide confidence in the results of the CFD simulation analyses performed for both cavities.

The results of this work carry meaningful implications for both HTGR safety analysis and future CFD modeling efforts. The comparison of the analyses with the LES and RANS turbulence models during the pressurization phase in cavity 1 shows that, while both models capture the dominant large-scale flow structures, the LES model resolves the small-scale turbulent interactions relevant to species mixing. These results come at a significant computational price. The primary challenge in this work is access to computational resources available at the high-performance computing facilities at UNM and the DOE Idaho National Laboratory. Simulating the 250 s long depressurization transient at UNM required approximately 2,000 wall hours and over 400,000 CPU hours (using 8 to 16 Intel Xeon Gold processors in parallel) for a 250-second simulation. This precludes the use of a CFL number of unity and restricts the scope of the parametric study.

Two modeling areas warranting further investigation are the turbulent Schmidt number, whose influence on species transport could not be fully characterized, and the properties of the forming gas mixture. A rigorous approach, such as Wilke's mixing rule for viscosity, could improve accuracy compared to the mass and mole fractions weighted averages used in this work. Furthermore, scaling the simulations to a full-size HTGR pressure vessel would incur computational costs orders of magnitude higher than in the present work, rendering the use of the LES turbulence model infeasible and impractical. Future work may therefore explore a hybrid turbulence modeling approach, such as Detached Eddy Simulation (DES). This can improve accuracy relative to the RANS model while reducing computational cost compared to the LES model. This is in addition to investigating using adaptive mesh refinement and concentrating the computational effort in regions of high scalar gradients.

From a safety and licensing perspective, the results of the present CFD simulation analyses contribute to the safety assessment of HTGRs, demonstrating the successful resolution of the local He-air mixing dynamics and identifying localized regions of elevated oxygen concentration and species stratification. These are consequential to reactor safety but beyond the capabilities of system-level codes. As computational resources continue to improve, progressively higher-fidelity analyses of reactor-scale mixing transients will become increasingly attainable, supporting continued design development and licensing of advanced HTGRs and VHTRs.

## Acknowledgements

We wish to thank Professor Masahiro Kawaji and Abdullah Abubakar at City College of New York for graciously providing the experimental data and the solid geometry CAD files for the RCTF used in this work. We are also grateful for the access to the resources of the High-Performance Computing Center at Idaho National Laboratory, which is supported by the Office of Nuclear Energy of the U.S. Department of Energy and the Nuclear Science User Facilities under Contract No. DE-AC07-05ID14517 and the University of New Mexico's Center for Advanced Research Computing, supported in part by the National Science Foundation, for providing access to its high-performance computing capabilities.

# Appendix A – Feed Tube CFD Simulation Analyses

To better simulate the behavior of the He injection into cavity 1, this appendix presents the CFD analyses of the He feed tube for the RCTF [Abubakar et al. 2024]. The feed tube consists of two distinct sections: (a) 3.0 m long Inconel 600 pipe with inner and outer diameters of 1.9 cm and 2.7 cm, respectively (Figs. A1 and A1). It is wrapped with a 600 W insulated heating element that heats the He gas to the desired injection temperature for injection into cavity 1. A variable AC transformer adjusts the power to the heating element. (b) 0.467 m long, thermally insulated stainless-steel tube with inner and outer diameters of 1.38 cm and 2.7 cm, respectively. It is welded to the Inconel section of the feed tube and to a He injection nozzle at the other end through the wall of cavity 1.

At the start of the experiment, the valve on the He supply tank is opened manually to initiate He flow through the feed tube and into cavity 1. The He flow increases until reaching a setpoint, where it remains through the end of the experiment. The heater power is then adjusted to maintain the desired temperature of injected He into cavity 1. This temperature is recorded by a TC inserted through the wall of the stainless-steel section of the feed tube (Fig. A1). The recorded temperature reported by Abubakar et al. [2024 and 2025] is considered equivalent to the temperature of the injected He gas in cavity 1, both in the experiment and in the present CFD simulation analyses. However, given possible thermal losses through the insulated wall of the 24.7 cm long latter part of the stainless-steel tube, the He injection temperature is likely to be a few degrees lower than that recorded by the TC.

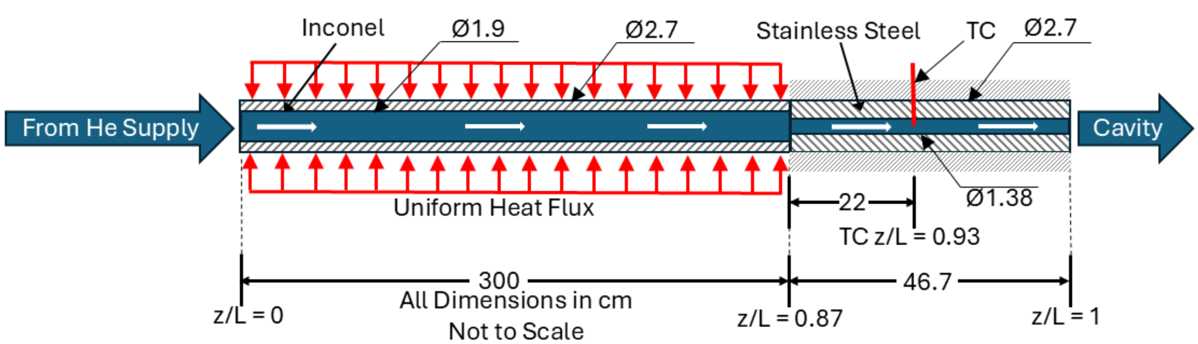


**Fig. A1:** He Feed Tube Configuration without a Flow Development Entrance Section.

The objectives of the feed tube CFD analysis detailed in this appendix are: (1) to investigate the effects of both the TC in the stainless-steel section of the feed tube and the He gas flow and temperature developments in the feed tube, and (2) to quantify the difference between the temperature measured at the TC location and that of the injected He into cavity 1. The analysis calculates radial temperature and velocity profiles throughout the feed tube and at its exit for four geometric configurations and two heater powers. One of the two configurations of the feed tube has an adiabatic, 15 cm long entrance section to facilitate the hydrodynamic development of the He gas flow before it enters the heated Inconel section of the feed tube. The tube configurations investigated, with and without the flow development entrance, are shown in Figs. A1 and A2, respectively.

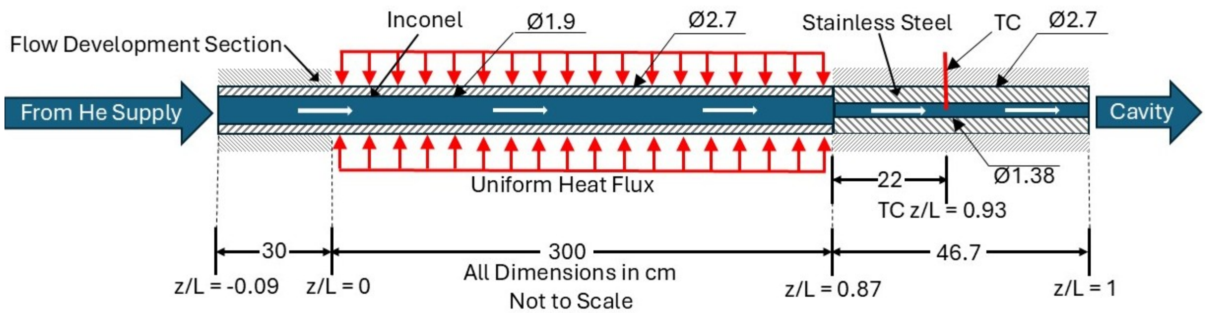


**Fig. A2:** He feed tube configuration with a flow development entrance section.

### *A1 Analysis Methodology*

The steady-state CFD simulation analyses of the He flow in the feed tube (Figs. A1 and A2) use the Star-CCM+ commercial software, version 2306.0001 build 18.04.009 [Siemens PLM 2023]. The walls of the Inconel and stainless-steel sections of the feed tube, and the entrance flow development length, are modeled as solid domains, and the interior is modeled as a He gas domain. The analyses use the reported He mass flow rate (0.24 g/s) for experiment No. 6 [Abubakar et al. 2024]. This condition is imposed at the inlet of the feed tube, with a uniform temperature of 300 K. The exit condition in the CFD analyses of the He feed tube is atmospheric pressure. The walls of the Inconel and stainless-steel sections of the feed tube pipes are initially at 500 °C, and the heater power is uniformly applied along the 3.0 m long Inconel section of the feed tube. The outer surfaces of the flow entrance section, when applicable, and of the stainless-steel section of the feed tube are assumed to be perfectly adiabatic (Figs. A1 and A2). The He thermophysical properties (specific heat, density, and thermal conductivity) are temperature dependent [Vega et al. 2023; Arp et al. 1998].

**Table A1:** Inconel and stainless-steel material properties.

| Material | Density ($kg/m^3$) | Specific Heat (J/kg*K) | Thermal Cond. (W/m*K) | Reference |
|---|---|---|---|---|
| Inconel 600 | 8,470 | 444 | 15.3 | ASTM B167 |
| 316 Stainless Steel | 8,000 | 500 | 16.3 | AISI 316 / UNS S31600 |

The two fluid mesh refinements (a coarse and a fine mesh) implemented have hexahedral (trimmed) mesh cell elements for the He domain and polyhedral mesh cell elements in the feed tube walls. The thin mesh cell elements implemented at the interface between the wall and the He flow capture the temperature and velocity gradients. Additionally, the very thin prism layer captures the interface temperature and the corresponding heat transfer rate within the feed tube walls. In both the coarse and fine mesh grids, the prism layer cell elements have a stretching factor of 1.3 to better resolve the boundary layer at the fluid flow-wall interface. The other mesh parameters are shown in Table A2, and the cross sections of the developed meshes are shown in Fig. A3 below.

**Table A2:** Numerical mesh grid refinement parameters.

| Mesh Grid | Domain | Base Cell Size (mm) | # of Thin Layers | # of Prism Layers | Layer Total Thickness (mm) | Total Cell Count |
|---|---|---|---|---|---|---|
| Coarse | Pipe Walls | 4 | 2 | 1 | 0.5 | 467,460 |
| | He | 1 | N/A | 12 | 1 | 4,150,545 |
| Fine | Pipe Walls | 2 | 4 | 1 | 0.25 | 769,206 |
| | He | 0.5 | N/A | 12 | 1 | 19,741,326 |

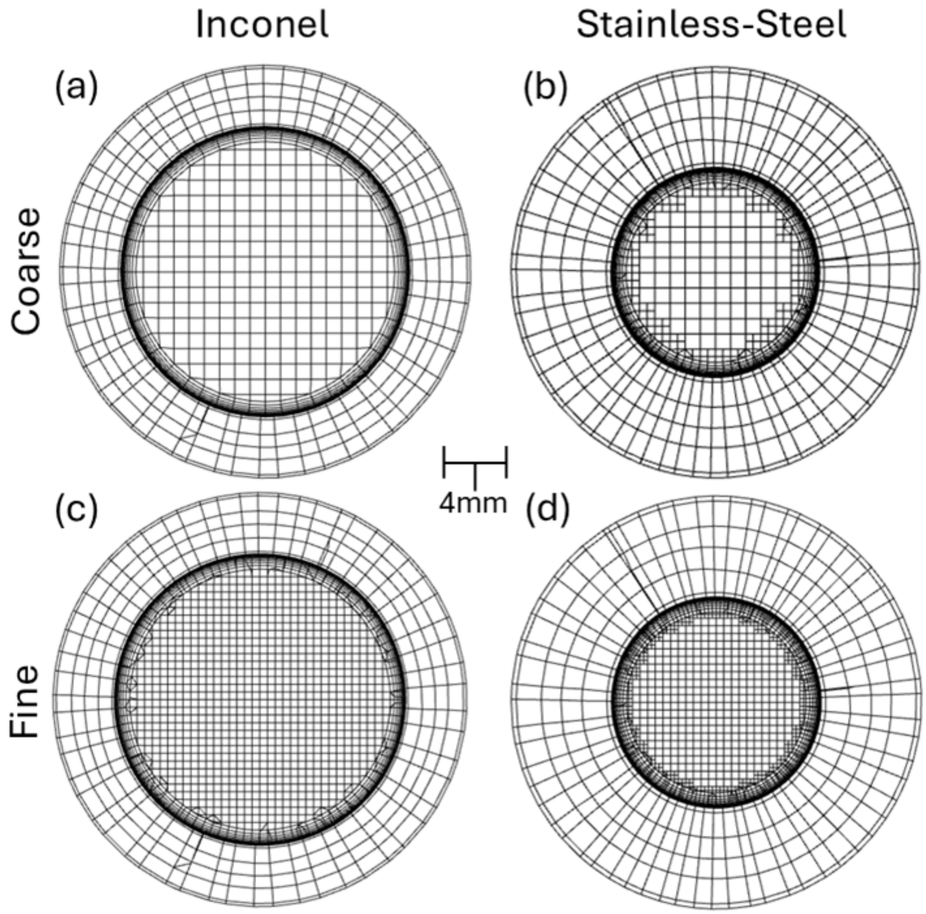


**Fig. A3:** Radial cross sections of the implemented numerical mesh grids in the Inconel and stainless-steel sections of the feed tube.

Initial simulations, using both fine and coarse meshes, utilize an added flow development length and no TC in the stainless-steel section of the feed tube. These simulations have undergone 20,000 iterations to ensure convergence of the solution and the residual. The calculated average He exit temperature and velocity, the pressure drop, and the highest wall temperature are compared to assess the effect of the mesh refinement on the results. The relative differences in the calculated results using the two numerical grids are 0.052% for the average exit temperature, 0.276% for the average exit velocity, 0.117% for the pressure drop, and 0.056% for the highest wall temperature. Given these very small differences and that both meshes were found to be well within the computational budget, the fine mesh is used in all subsequent calculations with the same number of iterations.

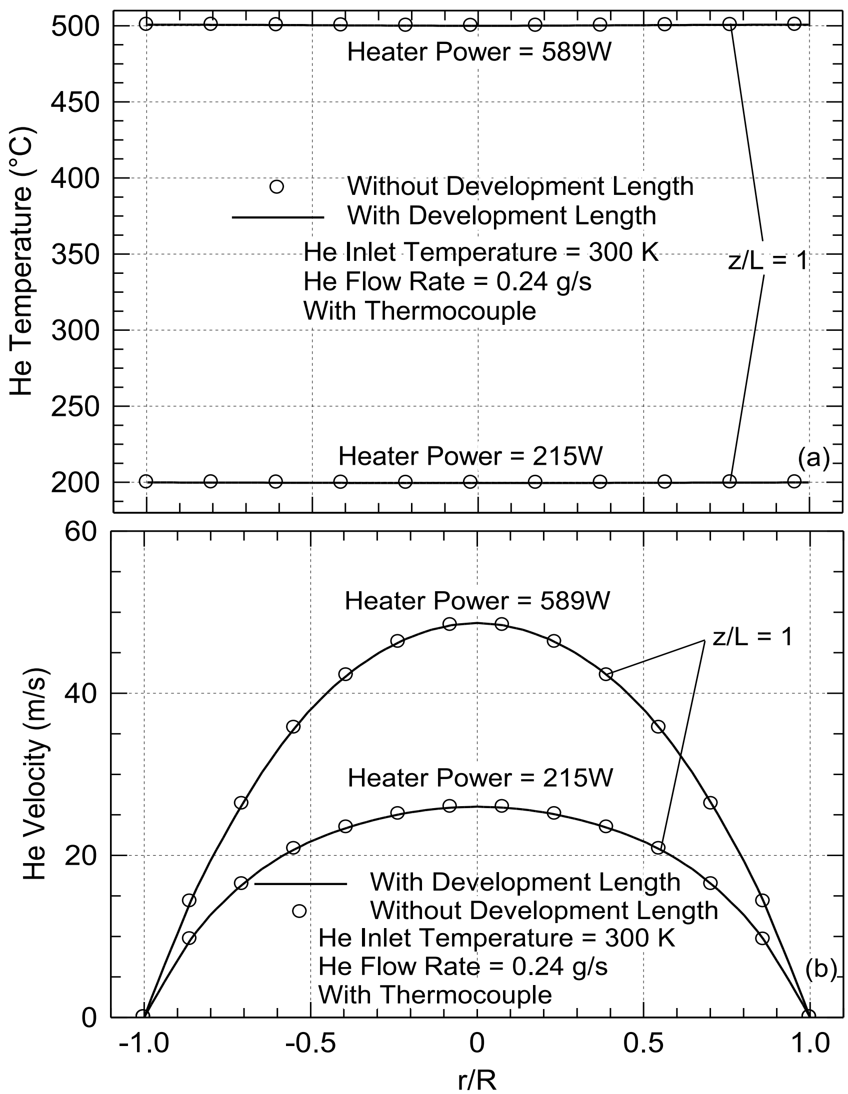


**Fig. A4:** Radial He Velocity and Temperature at Exit of the feed tube with and without Development Length.

Steady-state simulations are then carried out for 215 and 594 W of heater power, with a uniform surface heat flux, as shown in Figs. A1 and A2. The 215 W heater power was determined from a transient analysis of the required power to heat the Inconel to 500 °C in 2 hours with no He flow, and the 594 W heater power was determined from an energy balance to achieve a He injection temperature of 500 °C. Finally, thermal analyses of the feed tube configuration with a flow development length and no TC inserted through the wall of the stainless-steel section are performed at 300, 400, 500, and 600 W of heater power to determine the difference between the He exit temperature and the calculated TC tip temperature. The analysis results are presented and discussed next.

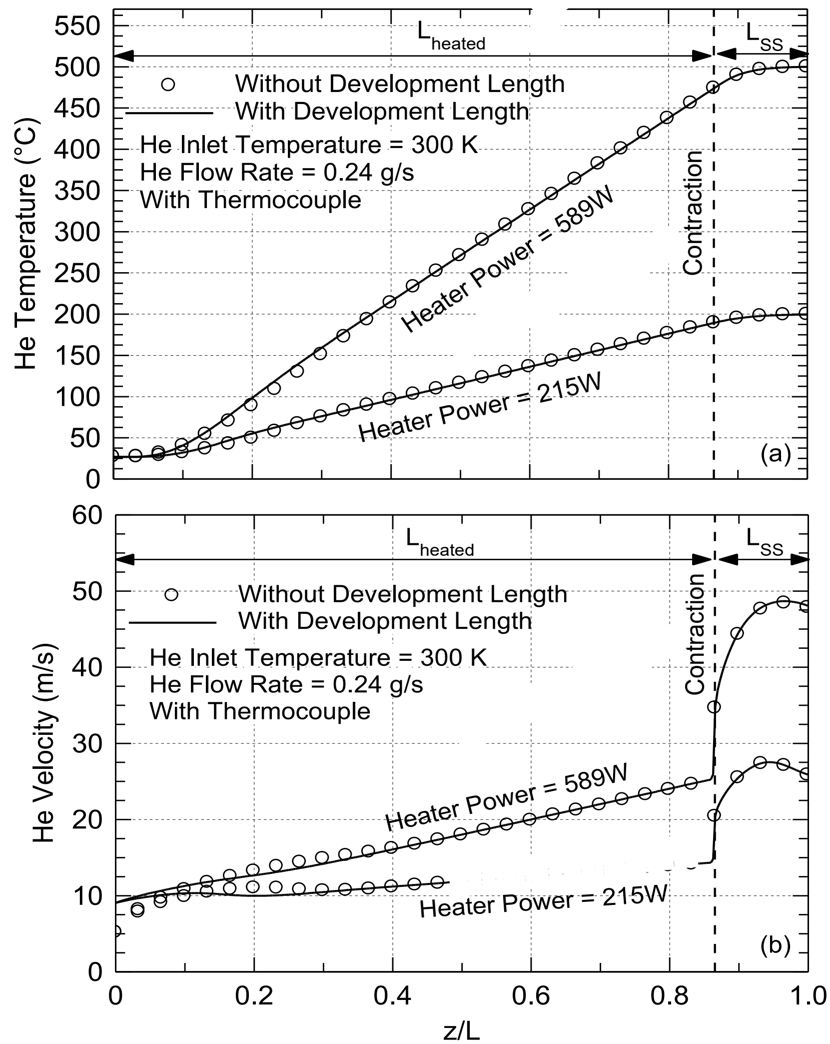


**Fig. A5:** Centerline He Velocity and Temperature along the length of the feed tube, with and without Development Length.

### *A2 Results and Discussion*

The following results (Figs. A4 - A9) are of the performed CFD analyses of the He gas flow through the feed tube, from which He is injected into cavity 1 of the experiment. The calculated radial temperature profiles of the He exiting the feed tube for cases with and without the development length are identical for both heater powers of 215 and 589 W (Fig. A4). There are no noticeable differences in the centerline temperature along the length of the feed tube (Fig. A5a). Still, minor differences in the He centerline velocity are observed in the early sections of the heated Inconel section (Fig. A5b). This entrance effect disappears at approximately z/L = 0.3, beyond which the velocity distributions are nearly identical.

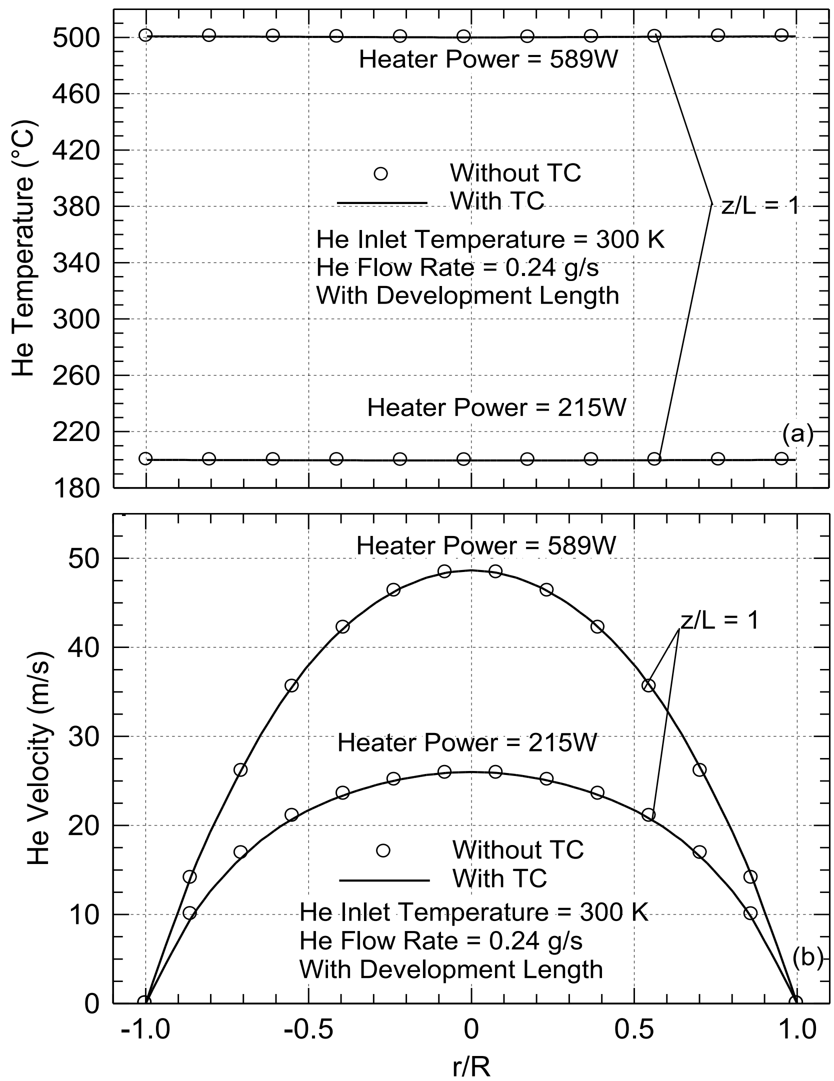


**Fig. A6:** Radial distribution of the He flow velocity and temperature at the exit of the feed tube without a flow development section and with and without TC in the stainless-steel section.

The results of the effect of the TC in the stainless-steel section of the feed tube on the flow field and the local temperature, and that of the He exiting the tube, are presented in Fig. A6. Results show that the presence of the TC negligibly affects the radial velocity and temperature profile of He gas exiting the feed tube (Fig. A6). The calculated effects on the flow field at and downstream of the TC location eventually disappear as the flow becomes fully developed before it exits the feed tube. This is likely because the stainless-steel connecting pipe length after the TC is long enough for the flow to become fully developed again. However, there are no noticeable differences in the calculated He temperature at the TC location (Figs. A7a and A8). Nonetheless, perturbations in the velocity fields at and downstream of the TC are evident (Figs. A7b and A9a), where a wake is observed.

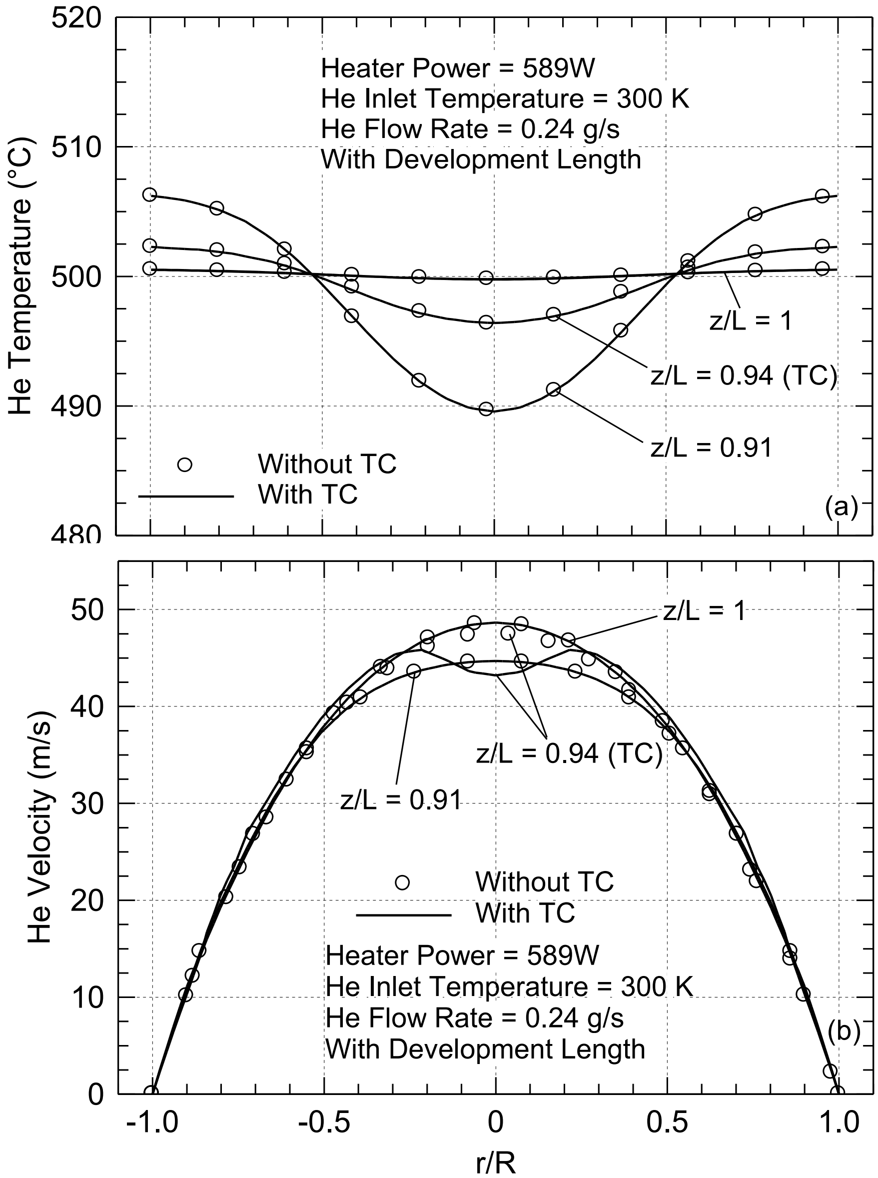


**Fig. A7:** Calculated radial He velocity and temperature profiles at multiple axial locations in the feed tube, with and without TC in the stainless-steel section.

Results also show that the radial temperature profile at the exit of the feed tube (z/L = 1) is nearly uniform (Figs. A7a). In contrast to the temperature, the exit velocity is non-uniform but has a parabolic radial profile consistent with that of fully developed laminar flow (Figs. A4b, A6b, and A7b). The results of the CFD analyses compare the calculated temperature at the TC tip with that at the feed tube exit. For the feed tube with an entrance flow development length and no TC present in the stainless-steel section, the temperature difference between the He flow exit and calculated at the TC tip is 3-5 °C, for all cases (Table A3). The high temperature difference occurs at higher heating element power, and vice versa. Actual differences, however, could be larger when accounting for the uncertainties in the TC measurement.

**Table A3:** Temperature difference of injection and TC locations at various heater powers.

| Heater Power (W) | $T_{injection} - T_{TC}$ (°C) |
|---|---|
| 215 | 3 |
| 300 | 3 |
| 400 | 4 |
| 500 | 5 |
| 600 | 5 |

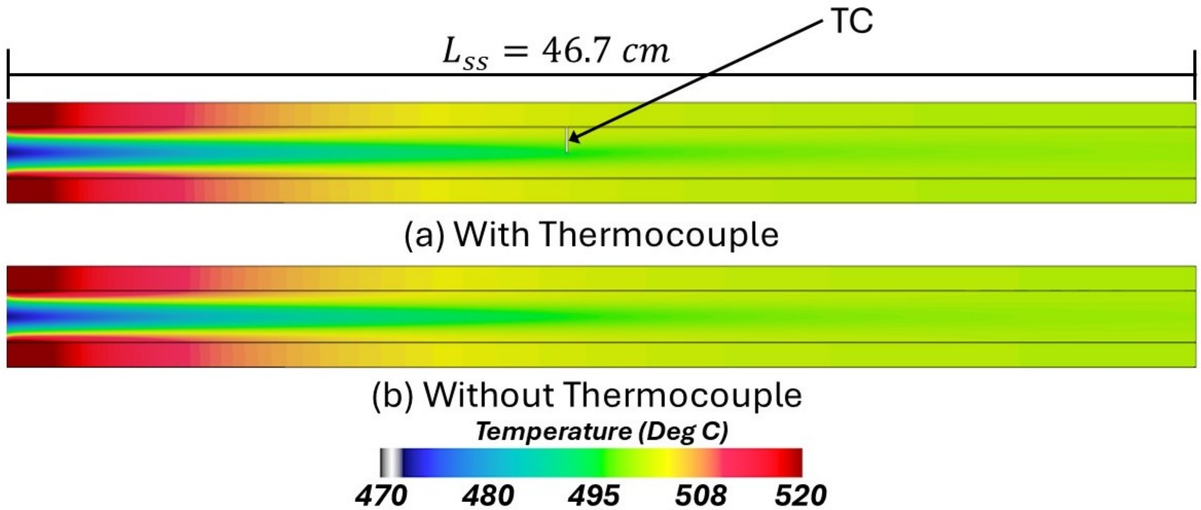


**Fig. A8:** Temperature contours in stainless-steel section with (a) and without (b) TC.

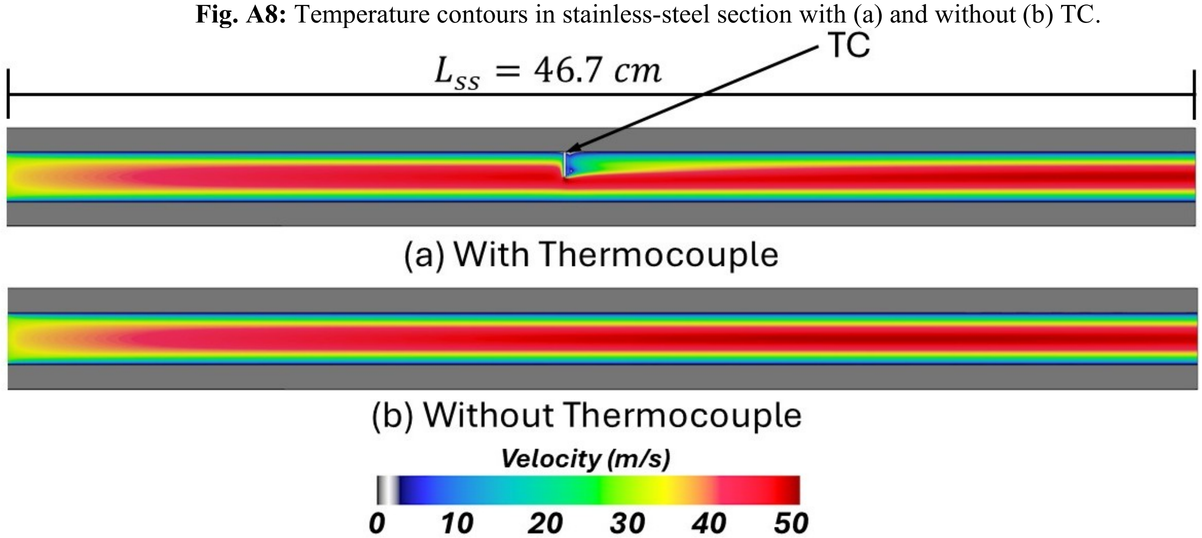


**Fig. A9:** Velocity contours in the stainless-steel section with (a) and without (b) TC.

# Appendix B – Measurements Uncertainties of Oxygen Concentration in the Experiments

The reported oxygen concentration measurements in the experiment by Abubakar et al. [2024 and 2025] are obtained using Honeywell MF020 Zirconium Dioxide ($ZrO_2$) oxygen sensors. These sensors operate by detecting the partial pressure of oxygen in a gas mixture through a dynamic process occurring across two zirconium oxide discs forming a hermetically sealed chamber. When stabilized zirconium dioxide is held at elevated temperatures, it behaves like an electrolyte, and a Nernst voltage is generated across the disc when different oxygen partial pressures are present on either side [SST Sensing, 2017]. These sensors have a stated accuracy of ±2 vol% oxygen and a response time of approximately 3 seconds [Honeywell, 2011]. The experimental conditions may have influenced the measurements recorded by these sensors, as indicated by Balderramma Prieto [2022] and Kultgen [2025] below.

Balderramma Prieto [2022] conducted similar experiments using the same type of oxygen sensor and identified prolonged exposure to low oxygen environments as a potential cause of sensor drift and eventual failure. The oxygen concentrations in those experiments were approximately 5 vol%, comparable to the oxygen concentration measured during the final minute of the hot He injection in cavity one of Abubakar et al.'s experiment analyzed in this work. Balderramma Prieto [2022] observed that drift occurred during transients lasting longer than 1 minute, and oxygen concentration data from numerous experimental runs were ultimately excluded due to sensor-related issues. Given the similarity in operating conditions, it is plausible that analogous sensor behavior may have affected the reliability of the low oxygen concentrations recorded in the Abubakar et al. experiments.

Similarly, Kultgen [2025] conducted analogous experiments using zirconia-based oxygen sensors. Upon contacting the sensor manufacturer, it was noted that the use of zirconia oxygen sensors in He-rich environments is outside their intended application. Kultgen summarized the manufacturer's response as "helium's higher thermal conductivity will cause the zirconia cell to reach higher temperatures as it is not attached to their internal heater. Since their instrument can be envisioned as an O2 ion pump, the relatively higher temperatures translate to faster pumping and lower O2 values." This effect leads to a systematic underestimation of the actual oxygen concentration in He-rich gas mixtures, which is further exacerbated at higher He concentrations. Kultgen [2025] also observed unrealistic increases in oxygen concentration measurements as cavity pressure increased, similar to observations in the Abubakar et al. [2024, 2025] experiments. This was attributed to the sensor's operating principle: the partial pressure of oxygen within the cavity increases with increasing total cavity pressure. Finally, degraded sensor performance over time was also observed, with noticeable deterioration of measurement capabilities and the complete failure of two oxygen sensors deployed in regions of high He concentration.

For zirconium oxide oxygen sensors, manufacturers and practitioners advise limiting direct immersion in fast-flowing gases. This is typically achieved either by positioning sensors close to walls, where direct gas impingement is minimal, or by employing protective baffles to stagnate local flow and ensure reliable sensor operation [SST Sensing, 2017]. If the sensors in the Abubakar et al. experiments were exposed to high gas flow velocities without such precautions, this would introduce additional measurement uncertainty beyond the device's stated accuracy. The results of the CFD simulation analyses suggest that OS6, in particular, could be affected by local flow velocity, as it is the sensor on which the hot He jet impinges directly.

Collectively, the evidence presented in this appendix highlights several compounding sources of uncertainty in the oxygen concentration measurements recorded during the experiments. The inherent device accuracy of ±2 vol%, potential sensor drift under prolonged He exposure, systematic underestimation in He-rich environments due to elevated zirconia cell temperatures, pressure-dependent partial pressure effects, degraded sensor performance over time, and the possible influence of high local flow velocities on sensors such as OS6 together suggest that the reported oxygen concentrations may not fully represent the true conditions within the cavity. These uncertainties are particularly relevant when evaluating the agreement between experimental data and CFD simulation analysis results. Notably, the CFD results during the 250-second transient period showed increasing deviation from the experimental measurements at higher oxygen concentrations, a trend consistent with the systematic underestimation bias introduced by the zirconia sensors in He-rich environments, where higher He concentrations, and therefore lower true oxygen concentrations, amplify the sensor error. Taken together, these factors indicate that caution should be exercised when drawing quantitative conclusions from the oxygen concentration data, and that the observed discrepancies between the CFD predictions and experimental measurements are at least partially attributable to sensor measurement limitations rather than deficiencies in the numerical model alone.

# References


Abubakar, A., Davis, M., Ahmed, Z., Kalaga, D., Kawaji, M., 2024. Helium-air mixing in simulated reactor cavities of high temperature gas reactors. Nuclear Engineering and Design 420, 113014. https://doi.org/10.1016/j.nucengdes.2024.113014

Abubakar, A., Sieh, B., Bindra, H., Schultz, R.R., Shahrokhi, F., McEligot, D.M., Kalaga, D., Kawaji, M., 2025. Effects of break geometry and orientation on helium-air mixing in simulated reactor cavities of high temperature gas reactors. Nuclear Engineering and Design 433, 113878. https://doi.org/10.1016/j.nucengdes.2025.113878

André, M.A., Burns, R.A., Danehy, P.M., Cadell, S.R., Woods, B.G., Bardet, P.M., 2019. Velocimetry during depressurized conduction cooldown events in the HTTF. Nuclear Engineering and Design 341, 406–414. https://doi.org/10.1016/j.nucengdes.2018.11.026

Arp, V.D., McCarty, R.D., Friend, D.G., 1998. Thermophysical Properties of Helium-4 from 0.8 to 1500 K with Pressures to 2000 MPa (Technical Note No. 1334). National Institute of Standards and Technology.

Balderrama Prieto, S.A., 2022. EXPERIMENTAL CHARACTERIZATION OF HTGR REACTOR CAVITY GAS DYNAMICS FOLLOWING A PRIMARY SYSTEM RUPTURE (Dissertation). University of Idaho.

Balderrama Prieto, S.A., Arcilesi, D., 2025. Experimental analysis of gas dynamics in the reactor cavity section of a High-Temperature Gas-Cooled Reactor during an accident scenario. Progress in Nuclear Energy 185, 105709. https://doi.org/10.1016/j.pnucene.2025.105709

Ball, S.J., Burchell, T.D., Corwin, W.R., Fisher, S.E., Forsberg, C.W., Morris, R.N., Moses, D.L., 2008. Next Generation Nuclear Plant GAP Analysis Report (GAP Analysis No. ORNL/TM-2007/228). Oak Ridge National Laboratory.

Ball, S.J., Fisher, S.E., 2008a. Next Generation Nuclear Plant Phenomena Identification and Ranking Tables (PIRTs) Volume 1: Main Report (PIRT No. ORNL/TM-2007/147). United States Nuclear Regulatory Commission.

Ball, S.J., Fisher, S.E., 2008b. Next Generation Nuclear Plant Phenomena Identification and Ranking Tables (PIRTs) Volume 2: Accident and Thermal Fluids Analysis PIRTs (PIRT No. ORNL/TM-2007/147,). United States Nuclear Regulatory Commission.

Beck, J.M., Pincock, L.F., 2011. High Temperature Gas-cooled Reactors Lessons Learned Applicable to the Next Generation Nuclear Plant (No. INL/EXT-10-19329). Idaho National Laboratory.

COMSOL, Inc., 2020. COMSOL Multiphysics®.

Courant, R., Friedrichs, K., Lewy, H., 1967. On the Partial Difference Equations of Mathematical Physics.

Crownhart, C., 2025. AI is changing the grid. Could it help more than it harms? MIT Technology Review.

DOE, Office of Nuclear Energy, 2025. Advantages and Challenges of Nuclear-Powered Data Centers. Nuclear Energy.

DOE, Office of Nuclear Energy, 2024. Nuclear 101: What Is a High-Temperature Gas Reactor? Nuclear Energy. URL https://www.energy.gov/ne/articles/nuclear-101-what-high-temperature-gas-reactor

Dubief, Y., Delcayre, F., 2000. On coherent-vortex identification in turbulence. Journal of Turbulence 1, N11. https://doi.org/10.1088/1468-5248/1/1/011

El-Gabry, L.A., Thurman, D.R., Poinsatte, P.E., 2014. Procedure for Determining Turbulence Length Scales Using Hotwire Anemometry (No. NASA/TM—2014-218403). NASA.

El-Genk, M.S., Tournier, J.-M.P., 2013. Transient gasification in an NBG-18 coolant channel of a VHTR prismatic fuel element. Progress in Nuclear Energy 64, 16–30. https://doi.org/10.1016/j.pnucene.2012.11.004

El-Genk, M.S., Tournier, J.-M.P., 2012. Validation of gasification model for NBG-18 nuclear graphite. Nuclear Engineering and Design 250, 142–155. https://doi.org/10.1016/j.nucengdes.2012.05.016

El-Genk, M.S., Tournier, J.-M.P., 2009. Small Size Turbo-Machines for HTR Plants, in: ASME 2009 Power Conference. Presented at the ASME 2009 Power Conference, ASMEDC, Albuquerque, New Mexico, USA, pp. 665–674. https://doi.org/10.1115/POWER2009-81171

El-Genk, M.S., Tournier, J.-M.P., Contescu, C.I., 2014. Chemical kinetics parameters and model validation for the gasification of PCEA nuclear graphite. Journal of Nuclear Materials 444, 112–128. https://doi.org/10.1016/j.jnucmat.2013.09.031

Fournier, Y., Bonelle, J., Moulinec, C., Shang, Z., Sunderland, A.G., Uribe, J.C., 2011. Optimizing Code_Saturne computations on Petascale systems. Computers & Fluids 45, 103–108. https://doi.org/10.1016/j.compfluid.2011.01.028

Fütterer, M.A., 2015. Operation and utilisation of the high flux reactor: annual report 2014. European Commission. Joint Research Centre. Institute for Energy and Transport.

Generation IV International Forum, 2014. Technology Roadmap Update for Generation IV Nuclear Energy Systems (No. 45073529). Nuclear Energy Agency.

Ham, T.K., Arcilesi, D.J., Kim, I.H., Sun, X., Christensen, R.N., Oh, C.H., Kim, E.S., 2016.

Computational fluid dynamics analysis of the initial stages of a VHTR air-ingress accident using a scaled-down model. Nuclear Engineering and Design 300, 517–529. https://doi.org/10.1016/j.nucengdes.2016.02.011

Harp, J.M., Demkowicz, P.A., Winston, P.L., Sterbentz, J.W., 2014. An analysis of nuclear fuel burnup in the AGR-1 TRISO fuel experiment using gamma spectrometry, mass spectrometry, and computational simulation techniques. Nuclear Engineering and Design 278, 395–405. https://doi.org/10.1016/j.nucengdes.2014.07.041

Honeywell International Inc., 2011. MF010 Series Low Temperature and MF020 Series High Temperature Oxygen Sensors Data Sheet.

Huning, A.J., Chandrasekaran, S., Garimella, S., 2021. A review of recent advances in HTGR CFD and thermal fluid analysis. Nuclear Engineering and Design 373, 111013. https://doi.org/10.1016/j.nucengdes.2020.111013

Hunt, J.C.R., A.A. Wray, P, Moin, 1988. Eddies, Streams, and Convergence Zone in Turbulent Flows. Center for Turbulence Research Proceedings of the Summer Program 1988 193–208.

IEA, 2025. Global Energy Review 2025.

International Atomic Energy Agency, 2025. Energy, Electricity and Nuclear Power Estimates for the Period up to 2050, Reference Data Series. INTERNATIONAL ATOMIC ENERGY AGENCY. https://doi.org/10.61092/iaea.gwov-o544

International Atomic Energy Agency, 2024. Advances in Small Modular Reactor Developments. International Atomic Energy Agency.

International Atomic Energy Agency, 2014. General Atomics Prismatic Modular High Temperature Gas Cooled Reactor (Technical Data on Gas Cooled Reactors (GCR)), Advanced Reactors Information System (IAEA, ARIS). International Atomic Energy Agency.

J. M. Beck, L. F. Pincock, 2011. High Temperature Gas-Cooled Reactors Lessons Learned Applicable to the Next Generation Nuclear Plant (No. INL/EXT-10-19329). Idaho National Laboratory, Idaho Falls, Idaho 83415.

Kadoya, K., Matsunaga, N., Nagashima, A., 1985. Viscosity and Thermal Conductivity of Dry Air in the Gaseous Phase. Journal of Physical and Chemical Reference Data 14, 947–970. https://doi.org/10.1063/1.555744

Kim, J.S., Hwang, J.-S., Kim, E.S., Kim, B.J., Oh, C.H., 2016. Experimental study on fundamental phenomena in HTGR small break air-ingress accident. Annals of Nuclear Energy 87, 145–156. https://doi.org/10.1016/j.anucene.2015.08.012

Kindra, V.O., Rogalev, A.N., Kovalev, D.S., Ilin, I.V., Levina, A.I., 2025. Research and development of high temperature gas-cooled reactor nuclear power plants for combined production of electricity, heat and hydrogen. International Journal of Hydrogen Energy 148, 149968. https://doi.org/10.1016/j.ijhydene.2025.06.158

Kultgen, D.W., 2025. COMPREHENSIVE INVESTIGATION OF THE BUILDING ENVIRONMENT THROUGHOUT A DEPRESSURIZED LOSS OF FORCED COOLING ACCIDENT IN A HIGH TEMPERATURE GAS REACTOR (Dissertation). Purdue University, West Lafayette, Indiana.

Lemmon, E.W., Jacobsen, R.T., Penoncello, S.G., Friend, D.G., 2000. Thermodynamic Properties of Air and Mixtures of Nitrogen, Argon, and Oxygen From 60 to 2000 K at Pressures to 2000 MPa. Journal of Physical and Chemical Reference Data 29, 331–385. https://doi.org/10.1063/1.1285884

Li, F., Chen, F., Wang, H., Dong, Y., Zhang, Z., 2020. One implementation of vented low pressure containment for HTR. Nuclear Engineering and Design 356, 110412. https://doi.org/10.1016/j.nucengdes.2019.110412

Lisowski, D., Qiuping Lv, Bogdan Alexandreanu, Yiren Chen, Rui Hu, Tanju Sofu, 2021. An Overview of Non-LWR Vessel Cooling Systems for Passive Decay Heat Removal (Technical Letter Report No. ANL/NSE-21/3). Argonne National Laboratory, Lemont, IL 60439.

Liu, B., He, S., He, J., Moulinec, C., Uribe, J., 2025. Unsteady Reynolds-Averaged Navier-Stokes Simulation of Turbulent Buoyant Jets Issued into a Model HTGR Cavity with Bottom Venting. Nuclear Technology 211, 2559–2576. https://doi.org/10.1080/00295450.2025.2492964

Marrero, T.R., Mason, E.A., 1972. Gaseous Diffusion Coefficients. Journal of Physical and Chemical Reference Data 1, 3–118. https://doi.org/10.1063/1.3253094

Mills, K.C., 2002. Recommended Values of Thermophysical Properties for Selected Commercial Alloys (Technical Report). National Physical Laboratory.

Molkov, V., Shentsov, V., 2014. Numerical and physical requirements to simulation of gas release and dispersion in an enclosure with one vent. International Journal of Hydrogen Energy 39, 13328–13345. https://doi.org/10.1016/j.ijhydene.2014.06.154

Nicoud, F., Ducros, F., 1999. Sub-grid-Scale Stress Modelling Based on the Square of the Velocity Gradient Tensor. Flow, Turbulence, and Combustion.

Numerical Applications Inc., 2014. GOTHIC.

Oh, C.H., Kim, E.S., 2011. Air-ingress analysis: Part 1. Theoretical approach. Nuclear Engineering and Design 241, 203–212.

https://doi.org/10.1016/j.nucengdes.2010.05.064

Oh, C.H., Kim, E.S., 2010. ISOTHERMAL AIR INGRESS VALIDATION EXPERIMENTS AT IDAHO NATIONAL LABORATORY: DESCRIPTION AND SUMMARY OF DATA (No. INL/EXT-10-19727, 993545). https://doi.org/10.2172/993545

Oh, C.H., Kim, E.S., Kang, H.S., No, H.C., Cho, N.Z., 2009. Experimental Validation of Stratified Flow Phenomena, Graphite Oxidation, and Mitigation Strategies of Air Ingress Accidents (No. INL/EXT-09-16465). Idaho National Laboratory.

Ortiz Vega, D.O., Hall, K.R., Holste, J.C., Harvey, A.H., Lemmon, E.W., 2023. An equation of state for the thermodynamic properties of helium (No. NIST IR 8474). National Institute of Standards and Technology (U.S.), Gaithersburg, MD. https://doi.org/10.6028/NIST.IR.8474

Pope, S.B., 2004. Ten questions concerning the large-eddy simulation of turbulent flows. New J. Phys. 6, 35–35. https://doi.org/10.1088/1367-2630/6/1/035

Qin, S., Song, M., Vietz, S., Pham, C., Plummer, M., Strydom, G., 2022. High-Temperature Gas-Cooled Reactor Research Survey and Overview: Preliminary Data Platform Construction for the Nuclear Energy University Program (No. INL/RPT-22-68771-Rev000, 1887092). https://doi.org/10.2172/1887092

Reitsma, F., 2019. Introduction to the CRP on modular HTGR Safety Design, in: EVT1703158. Presented at the Joint IAEA–GIF Technical Meeting on the Safety of High Temperature Gas Cooled Reactors.

Revankar, S.T., Kultgen, D.W., 2022. Scaling and Engineering Design of Facility for Simulation of HTGR Reactor Building Response for a Break in Primary Coolant Break, in: Volume 7A: Thermal-Hydraulics and Safety Analysis. Presented at the 2022 29th International Conference on Nuclear Engineering, American Society of Mechanical Engineers, Virtual, Online, p. V07AT07A004. https://doi.org/10.1115/ICONE29-88852

Rodriguez, S., 2019. Applied Computational Fluid Dynamics and Turbulence Modeling, 1st ed. Springer.

Sabharwall, P., Weaver, K., Anand, N.K., Ellis, C., Sun, X., Choi, H., Chen, D., Christensen, R., Fronk, B.M., Gess, J., Hassan, Y., Jovanovic, I., Manera, A., Petrov, V., Vaghetto, R., Balderrama-Prieto, S., Burak, A.J., Burger, M., Cardenas-Melgar, A., Orea, D., Chavez, R., Choi, B., Garrett, L., Gaudin, G.L., Sutton, N., Ssennyimba, K.W., Young, J., 2022. Preconceptual Design of Multifunctional Gas-Cooled Cartridge Loop for the Versatile Test Reactor: Instrumentation and Measurement—Part II. Nuclear Science and Engineering 196, 16. https://doi.org/10.1080/00295639.2022.2070384

Settles, G.S., Liberzon, A., 2022. Schlieren and BOS velocimetry of a round turbulent helium jet in air. Optics and Lasers in Engineering 156, 107104. https://doi.org/10.1016/j.optlaseng.2022.107104

Shehabi, A., Smith, S.J., Hubbard, A., Newkirk, A., Lei, N., Siddik, M.A.B., Holecek, B., Koomey, J., Masanet, E., Sartor, D., 2024. 2024 United States Data Center Energy Usage Report (No. LBNL-2001637).

Shiozawa, S., Fujikawa, S., Iyoku, T., Kunitomi, K., Tachibana, Y., 2004. Overview of HTTR design features. Nuclear Engineering and Design 233, 11–21. https://doi.org/10.1016/j.nucengdes.2004.07.016

Siemens PLM, 2023. Simcenter Star CCM+.

SST Sensing LTD., 2017. O2 Sensors - Zriconium Dioxide (ZrO2) Oxygen Sensor Installation, Operation, and Compatibility Guide (No. AN-0050).

Standard Specification for Nickel-Chromium-Aluminum Alloys (UNS N06699), Nickel-Chromium-Iron Alloys (UNS N06600, N06601, N06603, N06690, N06693, N06025, N06045, and N06696), Nickel-Chromium-Cobalt-Molybdenum Alloy (UNS N06617), Nickel-Iron-Chromium-T, 2023.

Stauff, N.E., Lee, C.H., Wells, A., Filippone, C., 2021. DESIGN OPTIMIZATION OF THE HOLOS-QUAD MICRO-REACTOR CONCEPT. EPJ Web Conf. 247, 01005. https://doi.org/10.1051/epjconf/202124701005

Wells, B., Phillips, N., Geelhood, K., 2021. TRISO Fuel: Properties and Failure Modes (No. PNNL-31427). Pacific Northwest National Laboratory.

Wilson, T.L., S. J. Ball, R. T. Wood, M. S. Cetiner, W. P. Poore, 2012. Advanced Control and Protection System Design Methods for Modular HTGRs (No. ORNL/TM-2012/170). Oak Ridge National Laboratory, Oak Ridge, TN.

Yang, S.R., Kappes, E., Nguyen, T., Vaghetto, R., Hassan, Y., 2018. Experimental study on 1/28 scaled NGNP HTGR reactor building test facility response to depressurization event. Annals of Nuclear Energy 114, 154–164. https://doi.org/10.1016/j.anucene.2017.12.023

Yildiz, M.A., Yang, S.R., Vaghetto, R., Hassan, Y.A., 2018. Numerical analysis of 1/28 scaled NGNP HTGR reactor building test facility response to depressurization event using GOTHIC. Annals of Nuclear Energy 119, 46–65. https://doi.org/10.1016/j.anucene.2018.04.030

Zhou, X.W., Tang, C.H., 2011. Current status and future development of coated fuel particles for high temperature gas-cooled reactors. Progress in Nuclear Energy 53, 182–188.

https://doi.org/10.1016/j.pnucene.2010.10.003